AD-A280 491

AFIT/DS/ENG/94J-05

A diffraction-based model of

anisoplanatism effects in adaptive optic systems

DISSERTATION
Steven Edward Troxel
Captain, USAF

AFIT/DS/ENG/94J-05

94-19403
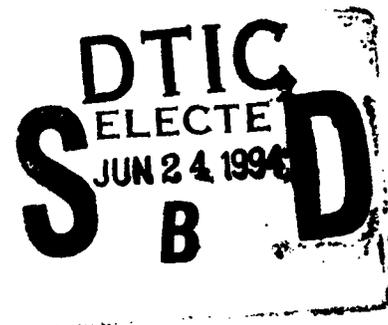
DTIC
ELECTE
JUN 24 1994
S
B
D

94 6 24 012

The views expressed in this dissertation are those of the author and do not reflect the official

policy or position of the Department of Defense or the U. S. Government.

AFIT/DS/ENG/94J-05

A diffraction–based model of

anisoplanatism effects in adaptive optic systems

DISSERTATION

Presented to the Faculty of the Graduate School of Engineering

of the Air Force Institute of Technology

Air University

In Partial Fulfillment of the

Requirements for the Degree of

Doctor of Philosophy

Steven Edward Troxel, B.S.E.E.,M.S.E.E.

Captain, USAF

June, 1994

A diffraction–based model of

anisoplanatism effects in adaptive optic systems

Steven Edward Troxel, B.S.E.E.,M.S.E.E.

Captain, USAF

Approved:
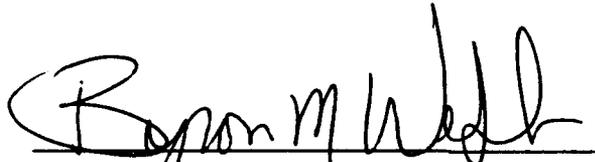
_____ 6 June 94
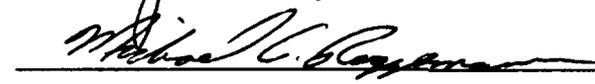
_____ 9 May 94
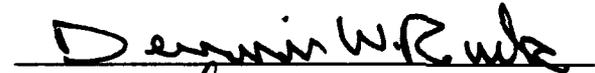
_____ 9 MAY 94
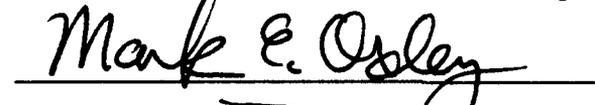
_____ 9 May 94

_____ 9 May 94
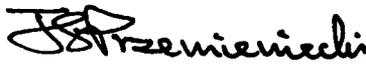
_____ 6 Jun 94

J. S. PRZEMIENIECKI
Institute Senior Dean and
 Scientific Advisor

Acknowledgements

I believe that the days of productive, *isolated* research are forever gone, or at least reserved for the true genius. Therefore, lacking in genius, I would like to thank the many people who contributed to this successful research effort. First and foremost, my advisor Dr. Byron Welsh for his continual guidance and insight. Dr. Welsh's ability to point toward areas of productive research resulted in a relatively streamlined research effort. Additionally, his rapid but ruthless editing abilities proved to be truly invaluable in generating research papers and this final document. I thank Dr. Mike Roggemann for, very early in this project, saving me many months of unproductive time by identifying a conceptual error and helping to redirect my efforts. I thank committee members Dr. Dennis Ruck, Dr. Mark Oxley, and Deans Representative Dr. Steve Rogers for their review of this document and for giving me the freedom to conduct research in the manner I felt was best. I thank Dr. Brent Ellerbroek of the Phillips Lab, for several timely technical discussions and Dr. Dustin Johnston, also of the Phillips Lab, for his encouragement and sympathy for the problems with my editor.

My fellow PhD students provided a very positive and supportive atmosphere. In particular I thank Ken Fielding for plowing the field of paperwork that allowed us to purchase our SUN workstations and for introducing me to the ROCKPILE when I was in need of extra computational power. I also thank my cubical mate Jim Brown for listening to my whining, for patiently answering my many math questions, and for loaning me his CDs.

I am forever indebted to my wife Sherry, and kids Shawn, Stacey, and Melissa. You never lost faith in my ability, and your pride in my accomplishments kept me pushing forward. You became my motivation. I thank the many members of Beavercreek Christian Church who offered much encouragement and allowed my family and I many opportunities to grow. Finally, this work is dedicated to the memory of Dr. Marcia Hamre who 20 years ago instilled in me the desire to achieve.

Steven Edward Troxel

iii

Table of Contents

List of Figures

List of Tables

AFIT/DS/ENG/94J-05

Abstract

This dissertation presents a new model for computing the angle dependent performance measures of an adaptive-optics system. By incorporating diffraction caused by the index-of-refraction variations of the atmosphere, the phase and amplitude fluctuations of the propagating wave are computed. New theory is presented, that uses the diffraction-based propagation model to yield optical transfer function (OTF) expressions that are more accurate as compared to current theory that neglects diffraction. An evaluation method for calculating the OTF is presented that utilizes a layered atmospheric model and normalized OTF expressions. The diffraction model is also used to present the first OTF signal-to-noise ratio (SNR) expressions that are a function of separation angle between the beacon and the object in an adaptive-optics system. An evaluation method for the SNR is presented that utilizes normalized correlation functions which are valid over a wide range of atmospheric conditions and correction geometries. An analysis of the angle dependency of the point spread function (PSF) is presented using the derived OTF expression. The diffraction model is then used to develop a new adaptive-optics wavefront correction algorithm that results in an extended correctable field-of-view (FOV) as compared to current correction algorithms.

A diffraction–based model of

anisoplanatism effects in adaptive optic systems

I. Introduction

1.1 Overview

The heating and cooling of the earth along with the mixing effects of the wind causes the atmosphere to be non-homogeneous and turbulent. The non-homogeneous aspect means that the atmosphere at one point in space is different from the atmosphere at another point in space. In particular, temperature fluctuations in the atmosphere cause the index–of–refraction of the atmosphere to be random in space and time. The study of how turbulence affects a propagating wavefront is well advanced with one of the most complete references being written in 1961 by Tatarski (46). As the wavefront from an object, such as a star, travels through the atmosphere, different parts of the wavefront will travel through different indices of refraction. This will cause different parts of the wavefront to experience different optical path lengths (20). The non–uniform optical path lengths result in bending of the wavefront. This bending causes different portions of the wavefront to travel in slightly different directions resulting in optical field perturbations. These optical field perturbations cause a significant portion of the blur experienced when imaging through the atmosphere and is the limiting factor in the resolution of an image observed from a large aperture ground based optical imaging system. However, through recent advances in adaptive–optics, it is now theoretically possible to view an exo–atmospheric object at resolutions near the diffraction limit of the imaging system (18).

Wavefront correction through the use of adaptive optics has been widely studied as a means to overcome turbulence effects (1, 2, 17, 18, 19, 34). Babcock first suggested 'the possibility of compensating astronomical seeing' in 1953 (1), and the relatively recent

1

advances of Welsh and Gardner in the areas of performance analysis and the use of laser guide stars (54, 55), may have hastened the declassification of military involvement in adaptive-optics in May 1991. Since that time, research activity has increased and reports concerning adaptive-optic applications have made their way to the open literature (8, 31, 45). Recent work at AFIT in the areas of adaptive-optics and image reconstruction include the work of Johnston in the area of multiconjugate adaptive optics (22) and the work of Pennington in comparing the performance of the shearing interferometer and the Hartman wavefront sensor for extended sources and large subaperture spacing (38). Also, Stoudt investigated a technique for improving the image quality through a post processing algorithm that selected the higher quality frames for the image reconstruction (44). VonNiederhausern developed an analysis program for obtaining system transfer functions as a function of number and size of sensor subapertures, sensor noise, and atmospheric turbulence (51). These system transfer functions were then used in the image reconstruction technique identified as 'Self-Referenced Speckle Holography' (53). In addition, Koeffler researched a technique for measuring the strength of the turbulence and wind velocity as a function of altitude (26).

The theory of adaptive optics states that by measuring the wavefront phase of a reference beacon such as a star, a laser guide star (13, 54, 55, 56), or a glint off of the object to be imaged, and then subtracting this phase from the object wavefront, an improvement in image quality will result. Wavefront measurements are made with a wavefront sensor (WFS) such as a Shack-Hartman sensor (18). These measurements are then converted into deformable mirror control commands (52) which are used to drive the actuators of a deformable mirror resulting in the desired wavefront correction. Theory indicates that perfect correction can be attained with a perfect wavefront correction system when the object wavefront propagates along the same path as the beacon. This perfect correction is referred to as diffraction limited correction.

Over the past several years, experiments have been performed using actual adaptive-optic systems (12, 36, 57). The results have been encouraging but have never quite matched the theoretical predictions of diffraction limited correction. One of the reasons that the ideal diffraction limited correction has been unattainable is that a wavefront correction system can

2

never be perfect. There will always be errors in the sampling and in the reconstruction of the wavefront. Much work is being done to minimize these errors, but, as this analysis will show, for a large aperture optical system in a turbulent atmosphere, the use of adaptive-optics will *never* allow the diffraction limit to be achieved. An understanding of the problems involved is obtained by examining a typical correction geometry.

In the most general case, the object and beacon locations are separated by the object angle, ϑ, as shown in Figure 1. However, the performance of the adaptive-optics system is known to degrade as ϑ increases and useful performance is limited to a small range of angles about the beacon (11, 12). The degradation in performance results from the turbulence effects along one optical path being only partially correlated with the turbulence in the other path. This partial correlation effect is referred to as anisoplanatism (10) and the maximum angular separation where good correlation is maintained is called the isoplanatic angle (θ_o). In addition, the effect of amplitude variations in the received wavefront degrades the performance of an adaptive-optics system which inherently only corrects for phase effects. Experimental results indicate that amplitude as well as phase variations are a real concern (5).

Proper accounting of phase and amplitude variations in a received wavefront requires an analysis based on diffraction. Much of the early work of anisoplanatism justifies dropping diffraction effects part way through the analysis (10). This analysis approach, commonly referred to as geometric optics, is widely used (23, 32, 33, 43, 49), and assumes that the only effect the atmosphere has on a propagating wave is in the form of wavefront phase aberrations due to integrated optical path differences. McKechnie, for example, breaks the atmosphere into phase screens which simply add a phase to a propagating wave (32). In good seeing conditions where the atmospheric profile contains little high altitude, or far-field turbulence, the use of a geometric optics calculation is convenient and yields accurate results. However, as conditions deteriorate in the form of a greater amount of high altitude turbulence, a performance analysis that neglects diffraction becomes less accurate.

The analysis presented here considers an adaptive–optics system which is able to perfectly measure the wavefront phase from a reference beacon, and in turn perfectly apply this
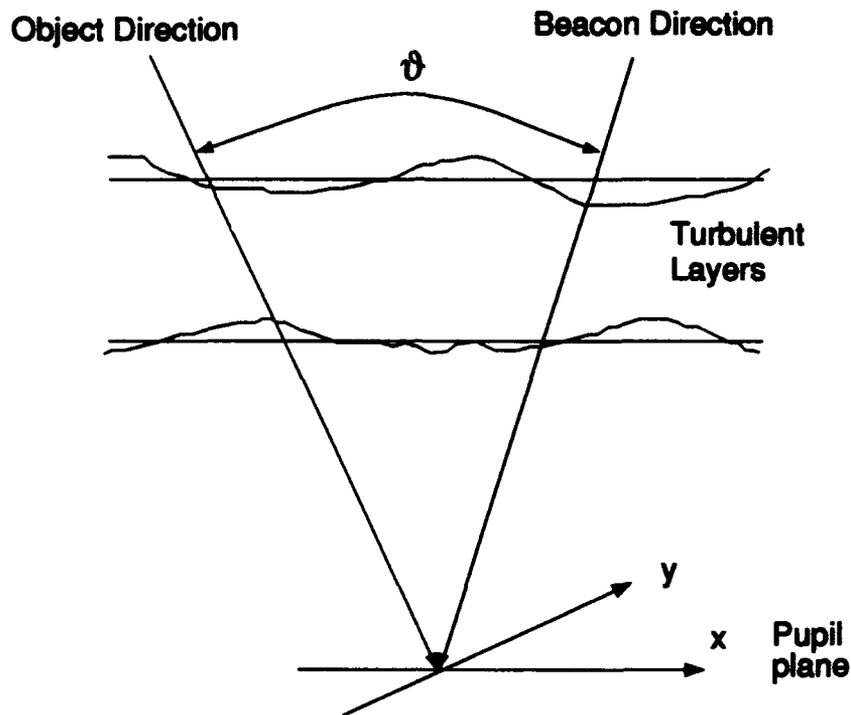
Figure 1. Object and beacon geometry

correction to the object wavefront. The constraint of an ideal adaptive–optics system, allows the analysis to focus on atmospheric effects, which for any large diameter optics will define the upper bound of performance. A diffraction calculation based on the work of Lee and Harp (30), and Tatarski (46) is used to account for both phase and amplitude perturbation effects of a wavefront in the pupil plane. The diffraction technique consists of expanding the atmosphere into thin slabs and then resolving the refractivity field within each slab into Fourier components of varying wave number. Each Fourier component is represented as a sinusoidally varying grating which diffracts the incident wave. The effect on a wavefront from each Fourier component in each slab can then be calculated and summed in the aperture to yield the resulting wavefront. The adaptive–optics system applies a phase correction, and performance measures are calculated based on the residual wavefront phase and amplitude perturbations in the pupil. Weak turbulence is assumed, which implies that the diffracted wave is relatively weak. Therefore, the effects of the diffracted wave being diffracted again

4

by subsequent slabs is ignored. Since the adaptive–optics system only corrects for phase perturbations, this diffraction analysis allows a more accurate calculation of the system performance than the current theory that neglects diffraction. The improvement in accuracy is due to the diffraction analysis accounting for both phase and amplitude effects. This analysis becomes essential for obtaining accurate performance results for adaptive–optic systems operating in an atmosphere containing high altitude turbulence.

Since an adaptive-optics system uses information measured along one path of the atmosphere to correct a wavefront passing through a different path, the analyzed performance measures will be dependent on the angular separation, or 'object angle' between the paths. One performance measure of an adaptive-optics system is the average optical transfer function (OTF). The OTF represents an excellent measure since other measures such as resolution, the point spread function (PSF) and the Strehl ratio can be derived from the OTF. The OTF is a measure of the attenuation of each object spatial frequency. Knowledge of the PSF is useful since in a shift invariant imaging system, the image intensity is determined by convolving the PSF with the object intensity. However, since an adaptive–optics imaging system yields an angle dependent PSF, the system is not shift invariant. The image intensity in a system that is not shift invariant involves a superposition integral of the shift dependent PSF (in our case – angular dependent PSF) and the object intensity distribution. The Strehl ratio is a useful measure in adaptive–optics since it defines how much the peak of the PSF has been reduced compared to a diffraction limited peak. An equally important measure is the OTF signal-to-noise ratio (SNR). Knowledge of the SNR is particularly important when image reconstruction is used in conjunction with adaptive-optics imaging (43). In image reconstruction, the system OTF can be used in conjunction with the measured image intensity to obtain an estimate of the actual object intensity. The SNR, which is a measure of the variability or randomness of the OTF relative to the mean value of the OTF, provides a measure of the quality with which the spectral components of the OTF can be used to reconstruct the object spectrum.

This research effort is the first to explicitly define a phase and amplitude OTF of an adaptive–optics system (48) and the first to yield diffraction based OTF SNR results

5

that are a function of the angle between the reference beacon and the object (47). Fried developed expressions for the angle dependent OTF but dismissed diffraction effects (9), and Roggemann (42, 43) produced OTF SNR results but did not consider the angle dependency.

Additionally, previous analyses utilize the Kolmogorov power spectrum for the atmospheric index of refraction variations. The use of the Kolmogorov power spectrum explicitly contains the assumption that the 'outer scale', or the largest eddy size of the turbulence, is infinite, creating a pole in the power spectrum at the index variation wavenumber, $\kappa = 0$ (14). There is no general agreement regarding the size of the outer scale, L_o. Conventional measurements put L_o at a value greater than most telescope diameters (5 - 10 meters), while McKechnie and others believe that the value of L_o is much smaller (20 - 40 cm) (6, 33). The analysis presented here is completely general with respect to the refractive index power spectrum, and allows for calculations of the effect of finite inner and outer scales. In Chapter II, an analysis of the effect of the inner and outer scales on the average OTF is presented. This research effort produced the first analysis of this type on the inner and outer scale effects (48).

Finally, a diffraction based analysis yields additional information regarding the propagating wavefronts. This information is used to develop a new adaptive–optics wavefront correction algorithm that increases the correctable field–of–view (FOV) of an adaptive–optics imaging system.

1.2   Problem statement

Establish a new model for the theory and numerical evaluation of the performance measures of an adaptive–optics system that is valid over a wide range of atmospheric turbulence parameters and is a function of separation angle between the reference beacon and the object source. The new model is to account for diffraction effects and provide for an effective evaluation of the average optical transfer function, the signal–to–noise ratio, and the point spread function.

1.3   Contributions

1. Development of a new diffraction–based model of atmospheric propagation for use in calculating the angle dependent performance measures of an adaptive-optics system.

The model incorporates diffraction to track both the amplitude and phase effects. An evaluation method is presented that results in rapid evaluation of the average OTF under changing atmospheric conditions (48). The OTF analysis is then extended by computing the angle dependent PSF through the inverse Fourier Transform of the OTF.

2. Development of a method for calculating the angle dependent OTF variance and SNR of an adaptive-optics system. This method uses the model discussed in Item 1 above to include both amplitude and phase effects. An evaluation method is presented that results in the rapid evaluation of the SNR under changing atmospheric conditions as well as correction geometries (47).

3. Development of a new adaptive-optics wavefront correction algorithm that extends the correctable FOV of the adaptive-optic system. The new model developed in Item 1 above yields additional information regarding the propagating wavefronts. This additional information is used to develop the new correction algorithm.

1.4   Outline of Dissertation

The remainder of this dissertation is organized as follows. Chapter II presents the derivation of the object angle dependent average OTF. This derivation consists of developing the wave perturbation equations in Section 2.2 and separately deriving the expression for the amplitude and phase OTFs in Sections 2.3 and 2.4 respectively. Chapter II also presents simplifications necessary to rapidly evaluate the OTF's under changing atmospheric conditions (48). Chapter III presents an analysis of the object angle dependent variance and SNR of the OTF, along with the required simplifications and method of evaluation (47). Chapter IV presents an analysis of the the PSF and the Strehl ratio utilizing the OTF developed in Chapter II. Chapter V considers a new wavefront correction algorithm that has the effect of extending the correctable FOV of the adaptive-optics system. This correction algorithm is a natural utilization of the wave perturbation equations developed in Section 2.2. Finally, a summary and conclusions of this research effort are presented in Chapter VI.

7

II. The angle dependent optical transfer function (OTF)

2.1 Introduction

The purpose of this chapter is to develop a model that allows for the derivation and evaluation of an angle dependent average optical transfer function (OTF) for an ideal adaptive-optics system (48). The model is to be valid over a wide range of atmospheric conditions and is to incorporate diffraction to properly track phase and amplitude effects of the corrected wavefront in the pupil plane of the adaptive-optics system. An understanding of the modeling of atmospheric turbulence as well as the use of phase screens is assumed. A model of atmospheric turbulence is presented in Appendix A and the concept of phase screens is discussed in Appendix B. The analysis begins by considering a linear imaging system.

In a linear imaging system, the object intensity may be considered to be composed of a sum of the object spatial frequencies. The response of a linear system to each spatial frequency component can be calculated separately. An image is formed by summing each spatial frequency at the output of the system. The OTF is a measure of the attenuation of each object spatial frequency as it passes through the system. The linear system of interest in this research is the atmosphere along with the adaptive-optics imaging system.

The atmosphere imposes optical distortions on a propagating wave due to the index-of-refraction variations. These variations are random, thereby producing an optical wave that must be considered a random process. The OTF that models the imaging system will also be a random process where the quantity of interest is the average value of the OTF. We distinguish between the phase and amplitude variations of the corrected field in the pupil plane of the adaptive-optics system by defining H_p as the average OTF due to the residual phase of the corrected wavefront in the pupil, and H_a as the average OTF due to the amplitude variations of the corrected wavefront in the pupil. Based on the work of Tatarski (46), Fried has shown that phase and amplitude variations of a wavefront, resulting from propagating through atmospheric turbulence, may be considered as independent wide sense stationary Gaussian random variables (9). Therefore, H_a and H_p can be calculated separately and multiplied

8

together to form the overall OTF due to the atmosphere. The OTF of the optics will not be addressed in this chapter, but the atmospheric OTF can always be multiplied by the optics OTF to yield an overall system OTF.

We begin by calculating the wavefronts from a beacon and an object that have propagated through the atmosphere at an angle ϑ as shown in Figure 1 on page 4. This calculation includes diffraction which tracks the phase and amplitude variations in the propagating wave. The adaptive–optics system subtracts the phase of the beacon field from the phase of the object field. The calculations of H_a and H_p are then based on the correlation of the amplitude and phase variations of the residual field in the pupil plane. The OTF curves calculated here will be expressed in terms of the shift variable $\vec{\rho}$ located in the aperture of the system. Once the optics of the system are chosen, the shift variable can be related to spatial frequency $\vec{\nu}$ by $\vec{\nu} = \frac{\vec{\rho}}{\lambda f}$, where f is the focal length of the optics and λ is the optical wavelength.

The remainder of this chapter is organized as follows. In Section 2.2, expressions are presented for the amplitude and phase perturbations of a wave that has propagated through atmospheric turbulence. Much of the actual derivation of these equations is deferred to Appendix C. The amplitude and phase perturbation equations are then used to derive the expressions for H_a and H_p in Sections 2.3 and 2.4, respectively. The derived OTF expressions are kept general with respect to the refractive index power spectrum. These generalized expressions allow for the analysis of the effect on the OTF due to the scale sizes of the turbulence as presented in Section 2.5. In Section 2.6, a new method of modeling the atmospheric turbulence through the use of discrete layers at preselected altitudes is presented. The method of preselected altitudes is essential in obtaining an OTF that can be scaled to different atmospheric conditions. Section 2.7 introduces the normalized OTF that is shown to be scalable over a large range of atmospheric conditions. Numerical results using the normalized OTF are then presented in Section 2.8. In Section 2.9, a direct comparison is made between the diffraction method of OTF calculation, as presented in this chapter, and the geometric optics method of OTF calculation. Finally, Section 2.10 summarizes the chapter.

9

2.2   Phase and amplitude perturbation equations

This section develops the necessary equations to describe the amplitude and phase variations of a wave that has propagated through the atmosphere at some angle ϑ with respect to the reference direction (see Figure 1 on page 4). We begin by deriving the wavefront perturbations resulting from a single Fourier component of the refractivity field in a single thin slab of the atmosphere located at an altitude η. We will then integrate over all Fourier components and all altitudes to obtain the total wavefront perturbations. A single Fourier component of spatial frequency, $\vec{\kappa}$, represents a sinusoidal refractive index variation. This single frequency component slab located at an altitude η, imposes a phase variation on the incident wavefront given by $A(\eta, \vec{\kappa}) \cos(\vec{\kappa} \cdot \vec{x} + \phi_o(\eta, \vec{\kappa}))$, where $A(\eta, \vec{\kappa})$ and $\phi_o(\eta, \vec{\kappa})$ are related to the amplitude and phase of the refractivity field Fourier component as shown in Appendix B, and $\vec{x}$ is a position vector in the plane of the slab. Propagating the perturbed wavefront to the pupil plane creates a complex wavefront which is fully described by its amplitude and phase components.

The process of determining the amplitude and phase variations in a propagating wave is accomplished using the approach of Lee and Harp (30) with the complete derivation given in Appendix C. The amplitude variation is given by

$$P_a(\eta, \vec{\kappa}, \vec{x}, \vartheta) \;=\; A(\eta, \vec{\kappa}) \sin(\eta\alpha) \cos(\eta\beta - (\vec{\kappa} \cdot \vec{x} + \phi_o(\eta, \vec{\kappa}))), \qquad (1)$$

and the phase variation is given by

$$P_p(\eta, \vec{\kappa}, \vec{x}, \vartheta) \;=\; -A(\eta, \vec{\kappa}) \cos(\eta\alpha) \cos(\eta\beta - (\vec{\kappa} \cdot \vec{x} + \phi_o(\eta, \vec{\kappa}))), \qquad (2)$$

where, $\alpha = \frac{|\vec{\kappa}|^2}{2k}$, $\beta = \vec{\kappa} \cdot \vec{\vartheta}$, and k is the wavenumber of the propagating wave. The angle dependence of the amplitude and phase perturbations is given as ϑ in the left hand side of Eqs. (1) and (2). This is a valid representation since, as shown in Appendix C, the orientation of $\vec{\vartheta}$ defines the x axis of the system (i.e., $\vec{\vartheta} = \vartheta\hat{x}$). The amplitude and phase perturbations of Eqs. (1) and (2), contain two differences from those given by Lee and Harp. First, an

approximation is used in place of Lee and Harp's expression for the wavenumber of the scattered wave, $(\sqrt{k^2 - \kappa^2} - k)$. Using the binomial expansion and the assumption that $\kappa \ll k$, the wavenumber of the scattered wave is given by

$$\sqrt{k^2 - \kappa^2} - k = k \left(\sqrt{1 - \frac{\kappa^2}{k^2}} - 1 \right) \approx \frac{\kappa^2}{2k}, \qquad (3)$$

where, $\kappa = |\vec{\kappa}|$. Second, Lee and Harp only considered on-axis propagation. With on-axis propagation, all orientations of $\vec{\kappa}$ will scatter the incident wave at angles with the same magnitude. The analysis presented here considers off-axis propagation where the orientation of $\vec{\kappa}$ with respect to the direction of incident propagation now determines the direction of the scattered wave. An off-axis propagation analysis produces the $\eta\beta$ term of Eqs. (1) and (2), where $\eta\beta = \eta\vec{\kappa} \cdot \vec{\vartheta}$. The angle dependence of Eqs. (1) and (2) yields the angle dependence of the performance measures discussed in this dissertation.

The idealized adaptive-optics system subtracts the measured phase of the beacon from the phase of the object. The residual phase of the adaptive-optics system for this single slab, designated $\Delta P_p(\eta, \vec{\kappa}, \vec{x}, \vartheta)$, is the difference between $P_p(\eta, \vec{\kappa}, \vec{x}, \vartheta)$ and $P_p(\eta, \vec{\kappa}, \vec{x}, 0)$:

$$\begin{aligned} \Delta P_p(\eta, \vec{\kappa}, \vec{x}, \vartheta) &= -A(\eta, \vec{\kappa}) \cos(\eta\alpha) \cos(\eta\beta - (\vec{\kappa} \cdot \vec{x} + \phi_o(\eta, \vec{\kappa}))) \\ &\quad + A(\eta, \vec{\kappa}) \cos(\eta\alpha) \cos(\vec{\kappa} \cdot \vec{x} + \phi_o(\eta, \vec{\kappa})). \end{aligned} \qquad (4)$$

The total residual phase is found by integrating over all altitudes η and all frequencies $\vec{\kappa}$.

$$\begin{aligned} \Delta P_p(\vec{x}, \vartheta) &= -\iint d\eta d\vec{\kappa} \Big(A(\eta, \vec{\kappa}) \cos(\eta\alpha) \cos(\eta\beta - (\vec{\kappa} \cdot \vec{x} + \phi_o(\eta, \vec{\kappa}))) \\ &\quad - A(\eta, \vec{\kappa}) \cos(\eta\alpha) \cos(\vec{\kappa} \cdot \vec{x} + \phi_o(\eta, \vec{\kappa})) \Big). \end{aligned} \qquad (5)$$

This analysis is simplified by use of complex phasor notation where the amplitude and residual phase variations can be written as

$$P_a(\vec{x}, \vartheta) = -\mathcal{R} \left\{ \iint d\eta d\vec{\kappa} \tilde{A}(\eta, \vec{\kappa}) e^{-j(\vec{\kappa} \cdot \vec{x})} \sin(\eta\alpha) e^{j\eta\beta} \right\}, \qquad (6)$$

11

and,

$$\Delta P_p(\vec{x}, \vartheta) = \mathcal{R}\left\{\iint d\eta d\vec{\kappa} \tilde{A}(\eta, \vec{\kappa}) e^{-j(\vec{\kappa}\cdot\vec{x})} \cos(\eta\alpha)(1 - e^{j\eta\beta})\right\}, \qquad (7)$$

where, $\tilde{A}(\eta, \vec{\kappa}) = A(\eta, \vec{\kappa}) e^{-j\phi_0(\eta,\vec{\kappa})}$ and $\mathcal{R}$ is an operator that takes the real portion of a complex quantity. The $\mathcal{R}$ operator is now dropped and work continues with the complex phasor representations $\underline{P_a}(\vec{x}, \vartheta)$ and $\underline{\Delta P_p}(\vec{x}, \vartheta)$ given by

$$\underline{P_a}(\vec{x}, \vartheta) = \iint d\eta d\vec{\kappa} \tilde{A}(\eta, \vec{\kappa}) e^{-j(\vec{\kappa}\cdot\vec{x})} \sin(\eta\alpha) e^{j\eta\beta}, \qquad (8)$$

and,

$$\underline{\Delta P_p}(\vec{x}, \vartheta) = \iint d\eta d\vec{\kappa} \tilde{A}(\eta, \vec{\kappa}) e^{-j(\vec{\kappa}\cdot\vec{x})} \cos(\eta\alpha)(1 - e^{j\eta\beta}). \qquad (9)$$

2.3 Amplitude OTF (H_a)

The derivation of H_a treats amplitude effects rather than log-amplitude effects as given in other research (9, 14). The log-amplitude can be a useful quantity and is used by many researchers in the study of atmospheric propagation (4, 9, 7, 28). By assuming Gaussian statistics and small amplitude variations, the log-amplitude leads to the wave structure function as discussed in (14). However, the assumption of small amplitude variations becomes less valid as high altitude turbulence strength increases. Since the analysis of the amplitude OTF will not rely on the wave structure function, the final result of this section, Eq. (18), will be used as a more general amplitude OTF expression which is valid under stronger turbulence conditions than a log–amplitude result.

The derivation of H_a begins by representing the amplitude variations of the wavefront in the pupil plane as a wide-sense stationary amplitude transmittance function given by

$$t_s(\vec{x}, \vartheta) = t_o + P_a(\vec{x}, \vartheta), \qquad (10)$$

where in general, t_o is some real and nonnegative bias lying between zero and unity. Here, we assume $t_o = 1$. The average OTF of this transmittance function is then given by (14)

$$H_a(\vec{\rho}) = \frac{1 + \Gamma_a(\vec{\rho})}{1 + \Gamma_a(\vec{0})}, \tag{11}$$

where $\vec{\rho}$ is a shift vector in the pupil plane and $\Gamma_a(\vec{\rho}) = \langle P_a(\vec{x}, \vartheta) P_a(\vec{x} + \vec{\rho}, \vartheta) \rangle$. The amplitude correlation function is related to the complex phasor representation of the amplitude perturbations given in Eq. (8) by

$$\Gamma_a(\vec{\rho}) = \frac{1}{2} \mathcal{R}\{\underline{\Gamma_a}(\vec{\rho})\} = \frac{1}{2} \mathcal{R}\langle \underline{P_a}(\vec{x}, \vartheta) \cdot \underline{P_a}^*(\vec{x} - \vec{\rho}, \vartheta)\rangle. \tag{12}$$

The notation $\langle \rangle$ represents the ensemble average. Here we use the property that the correlation of the complex representation is twice the value of the real valued correlation (14). Substituting Eq. (8) into Eq. (12) gives

$$\begin{aligned}
\underline{\Gamma_a}(\vec{\rho}) &= \iiiint d\eta_1 d\vec{\kappa}_1 d\eta_2 d\vec{\kappa}_2 \langle \tilde{A}(\eta_1, \vec{\kappa}_1) \tilde{A}^*(\eta_2, \vec{\kappa}_2)\rangle e^{-j(\vec{\kappa}_1 \cdot \vec{x} - \vec{\kappa}_2 \cdot (\vec{x} - \vec{\rho}))} \\
&\times \quad \sin(\eta_1 \alpha) \sin(\eta_2 \alpha) e^{j(\beta \eta_1 - \beta \eta_2)}.
\end{aligned} \tag{13}$$

The relations given in Appendix B and Appendix D are now used for propagation through long distances of atmospheric turbulence to yield

$$\langle \tilde{A}(\eta_1, \vec{\kappa}_1) \tilde{A}^*(\eta_2, \vec{\kappa}_2)\rangle = 8\pi k^2 \delta(\vec{\kappa}_1 - \vec{\kappa}_2) \delta(\eta_1 - \eta_2) \Phi(\vec{\kappa}_1, \eta_1), \tag{14}$$

where, $\Phi(\vec{\kappa}, \eta)$ is the three dimensional refractive index power spectrum with $\kappa^2 = \kappa_x^2 + \kappa_y^2$, and δ is the Dirac delta function. The $\delta(\eta_2 - \eta_1)$ part of Eq. (14) is a derived relation and should not be considered as a statement of independence of turbulent layers. Substituting Eq. (14) into Eq. (13) gives

$$\underline{\Gamma_a}(\vec{\rho}) = 8\pi k^2 \iint d\eta d\vec{\kappa} \Phi(\vec{\kappa}, \eta) \sin^2(\eta \alpha) e^{-j(\vec{\kappa} \cdot \vec{\rho})}. \tag{15}$$

13

Note that Eq. (15) is not a function of either β or ϑ. Taking half the real portion of Eq. (15), the final form of the amplitude correlation function is given by

$$\Gamma_a(\vec{\rho}) = 4\pi k^2 \iint d\eta d\vec{\kappa} \Phi(\vec{\kappa}, \eta) \sin^2(\eta\alpha) \cos(\vec{\kappa} \cdot \vec{\rho}). \tag{16}$$

Substituting Eq. (16) into Eq. (11) yields an expression for the average amplitude OTF,

$$H_a(\vec{\rho}) = \frac{1 + 4\pi k^2 \iint d\eta d\vec{\kappa} \Phi(\vec{\kappa}, \eta) \sin^2(\eta\alpha) \cos(\vec{\kappa} \cdot \vec{\rho})}{1 + 4\pi k^2 \iint d\eta d\vec{\kappa} \Phi(\vec{\kappa}, \eta) \sin^2(\eta\alpha)}, \tag{17}$$

and, substituting in the expression for α, where $\alpha = \frac{|\vec{\kappa}|^2}{2k}$, we are left with

$$H_a(\vec{\rho}) = \frac{1 + 4\pi k^2 \iint d\eta d\vec{\kappa} \Phi(\vec{\kappa}, \eta) \sin^2\left(\eta\frac{|\vec{\kappa}|^2}{2k}\right) \cos(\vec{\kappa} \cdot \vec{\rho})}{1 + 4\pi k^2 \iint d\eta d\vec{\kappa} \Phi(\vec{\kappa}, \eta) \sin^2\left(\eta\frac{|\vec{\kappa}|^2}{2k}\right)}. \tag{18}$$

Equation (18) represents the final result of this section. An example of an amplitude OTF is shown in Figure 2. This figure is simply an evaluation of Eq. (18) where an optical wavelength of 0.5 microns and a Hufnagel-Valley turbulence profile with a 54 mph upper altitude wind (21) has been assumed. This turbulence profile is labeled HV-54 in Figure 5. In this calculation, the Von Karman power spectrum is used, as discussed in Appendix A, with the inner scale, L_m, set at 1 millimeter and the outer scale, L_o, set at 5 meters. The use of turbulence profiles is discussed in more detail in Section 2.6 and an analysis of the inner and outer scale effects is presented in Section 2.5. Here, it is important only to note the initial sharp roll off and then the constant value attained by the transfer function. This is consistent with the amplitude transmittance functions given by Goodman (14) and will be characteristic of all amplitude OTFs.

2.4   Residual phase OTF (H_p)

The analysis of the average phase OTF, (H_p), begins much the same as the last section. Here the result for the total residual phase given by Eq (5), and the corresponding complex phasor representation given by Eq. (8), is used to define a phase only transmittance func-
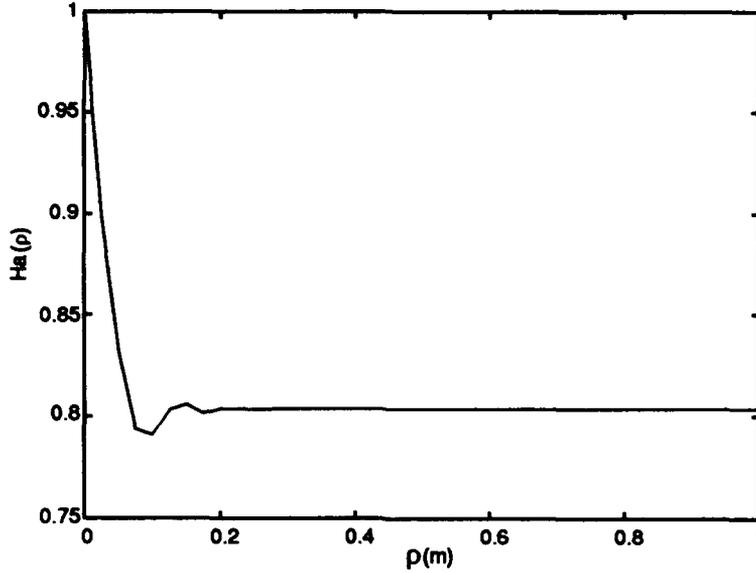
Figure 2. Amplitude OTF calculated for a wavelength of 0.5 microns, a Hufnagel-Valley turbulence profile with a 54 mph upper altitude wind (21), and a Von Karman power spectrum with $L_m = 1$mm and $L_o = 5$m.

tion (14). The residual phase is considered as a single phase screen with a transmittance of $t_p(\vec{x}, \vartheta) = \exp(j\Delta P_p(\vec{x}, \vartheta))$. The OTF of the phase screen is then calculated using (14)

$$
\begin{aligned}
H_p(\vec{\rho}, \vartheta) &= \frac{\langle t_p(\vec{x}, \vartheta) t_p^*(\vec{x} - \vec{\rho}, \vartheta) \rangle}{\langle t_p(\vec{x}, \vartheta) t_p^*(\vec{x}, \vartheta) \rangle} \\
&= \frac{\langle \exp(j\Delta P_p(\vec{x}, \vartheta)) \exp(-j\Delta P_p(\vec{x} - \vec{\rho}, \vartheta)) \rangle}{\langle \exp(j\Delta P_p(\vec{x}, \vartheta)) \exp(-j\Delta P_p(\vec{x}, \vartheta)) \rangle} \\
&= \frac{\langle \exp(j(\Delta P_p(\vec{x}, \vartheta) - \Delta P_p(\vec{x} - \vec{\rho}, \vartheta))) \rangle}{1}.
\end{aligned}
\tag{19}
$$

Assuming that the residual phase obeys Gaussian statistics gives,

$$
H_p(\vec{\rho}, \vartheta) = \exp\left\{ -\frac{1}{2} \langle (\Delta P_p(\vec{x}, \vartheta) - \Delta P_p(\vec{x} - \vec{\rho}, \vartheta))^2 \rangle \right\}.
\tag{20}
$$

15

Expanding the square within the expected value, and using the assumption that the residual phase is wide-sense stationary, the following expression for the residual phase OTF is obtained:

$$H_p(\vec{\rho}, \vartheta) = \exp\left\{\Gamma_p(\vec{\rho}, \vartheta) - \Gamma_p(\vec{0}, \vartheta)\right\}. \tag{21}$$

As with the amplitude correlation function, the complex phasor representation of the phase correlation function is defined as

$$\underline{\Gamma}_p(\vec{\rho}, \vartheta) = \langle \underline{\Delta P_p}(\vec{x}, \vartheta)\underline{\Delta P_p}^*(\vec{x} - \vec{\rho}, \vartheta)\rangle. \tag{22}$$

Substituting Eq. (9) into Eq. (22) gives

$$\underline{\Gamma}_p(\vec{\rho}, \vartheta) = \iiiint d\eta_1 d\vec{\kappa}_1 d\eta_2 d\vec{\kappa}_2 \langle \tilde{A}(\eta_1, \vec{\kappa}_1)\tilde{A}^*(\eta_2, \vec{\kappa}_2)\rangle e^{-j(\vec{\kappa}_1 \cdot \vec{x} - \vec{\kappa}_2 \cdot (\vec{x} - \vec{\rho}))}$$
$$\times \cos(\eta_1\alpha)(1 - e^{j\beta\eta_1})\cos(\eta_2\alpha)(1 - e^{-j\beta\eta_2}). \tag{23}$$

Using the same independence relation given by Eq. (14), yields

$$\underline{\Gamma}_p(\vec{\rho}, \vartheta) = 8\pi k^2 \iint d\eta d\vec{\kappa} \Phi(\vec{\kappa}, \eta) e^{-j(\vec{\kappa} \cdot \vec{\rho})} \cos^2(\eta\alpha)(1 - e^{j\beta\eta})(1 - e^{-j\beta\eta})$$
$$= 8\pi k^2 \iint d\eta d\vec{\kappa} \Phi(\vec{\kappa}, \eta) \cos^2(\eta\alpha)|1 - e^{j\beta\eta}|^2 e^{-j\vec{\kappa} \cdot \vec{\rho}}. \tag{24}$$

For the final form of the correlation function, half the real part of $\underline{\Gamma}_p(\vec{\rho}, \vartheta)$ is considered,

$$\Gamma_p(\vec{\rho}, \vartheta) = 4\pi k^2 \iint d\eta d\vec{\kappa} \Phi(\vec{\kappa}, \eta) \cos(\vec{\kappa} \cdot \vec{\rho}) \cos^2(\eta\alpha)(2 - 2\cos(\eta\beta)), \tag{25}$$

and, substituting in the expressions for α and β, where $\alpha = \frac{|\vec{\kappa}|^2}{2k}$, $\beta = \vec{\kappa} \cdot \vec{\vartheta}$, results in

$$\Gamma_p(\vec{\rho}, \vartheta) = 8\pi k^2 \iint \Phi(\vec{\kappa}, \eta) \cos^2\left(\frac{\eta|\vec{\kappa}|^2}{2k}\right) \cos(\vec{\kappa} \cdot \vec{\rho})[1 - \cos(\eta\vec{\kappa} \cdot \vec{\vartheta})]d\eta d\vec{\kappa}. \tag{26}$$

16

Substituting Eq. (26) into Eq. (21), yields the final expression for H_p:

$$H_p(\vec{\rho}, \vartheta) = \exp\left\{-8\pi k^2 \iint \Phi(\vec{\kappa}, \eta) \cos^2(\frac{\eta|\vec{\kappa}|^2}{2k})[1 - \cos(\vec{\kappa} \cdot \vec{\rho})][1 - \cos(\eta\vec{\kappa} \cdot \vec{\vartheta})]d\eta d\vec{\kappa}\right\}.$$

(27)

This is the OTF due to the residual phase of an ideal adaptive–optics system where the beacon and the object are separated by an angle ϑ. Note that this OTF is not circularly symmetric about the zero frequency. An example of a phase OTF is shown in Figure 3. Although the OTF equations allow for complete two dimensional calculations, the results of Figure 3 are calculated for $\vec{\rho}$ along the axis parallel to $\vec{\vartheta}$ which defines the x axis of the system. This figure is an evaluation of Eq. (27) with an optical wavelength of 0.5 microns and a Hufnagel–Valley turbulence profile with a 54 mph wind (21) as discussed in Section 2.6. The object angle, ϑ, equals 2.4 μrad, which is equal to the isoplanatic angle as defined by Fried (10). Once again, the Von Karman power spectrum with the inner scale, L_m, set at 1 millimeter and the outer scale, L_o, set at 5 meters is used. The effect of inner and outer scale on H_p is discussed in section 2.5. Here, note the characteristic shape of a phase OTF. The initial sharp roll off is followed by a much more gradually decreasing value of the OTF.

2.5   Effect of inner and outer turbulence scale sizes on the OTF

The purpose of this section is to quantify the significance of the turbulence scale sizes on the OTF. As previously stated, this analysis refrains from taking a stand on the value of the turbulence scale sizes of the atmosphere, but rather presents a method of calculating the effect. Up to this point, a specific form for the turbulence power spectrum $\Phi(\vec{\kappa})$ has not been assumed. The power spectrum can be written as a constant times a normalized power spectrum, $\Phi_o(\vec{\kappa})$. Details of the constant are discussed in Section 2.6. Most current research utilizes the Kolmogorov power spectrum where $\Phi_o(\vec{\kappa}) = |\vec{\kappa}|^{-11/3}$. The Kolmogorov power spectrum yields analytic results to many problems. Also, this form is known to match well with actual measured data over the region of the inertial subrange which is the range between the inner and outer scale values of $|\vec{\kappa}|$. What sometimes becomes lost with use of the Kolmogorov spectrum is the implication that the inner scale equals zero and the outer scale is infinity. A
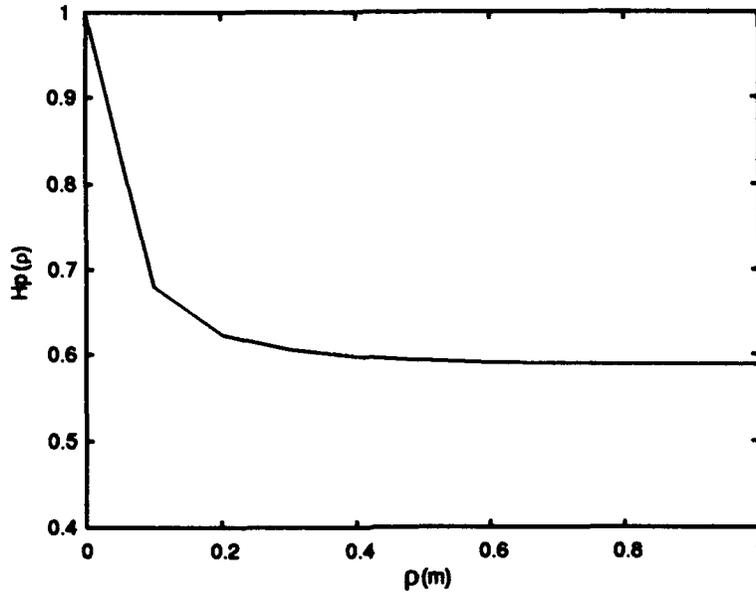
Figure 3. A phase OTF calculated for a wavelength of 0.5 microns, a separation angle of 2.4 μrad, a Hufnagel-Valley turbulence profile with a 54 mph high altitude wind (21), and a Von Karman refractive index power spectrum with $L_m = 1$mm and $L_o = 5$m.

non-zero inner scale and a finite outer scale is incorporated into the calculations by using a modification to the Kolmogorov spectrum known as the Von Karman power spectrum given by

$$\Phi_o(\vec{\kappa}) = \frac{e^{\left(-\frac{|\vec{\kappa}|^2 L_m^2}{4\pi^2}\right)}}{\left(|\vec{\kappa}|^2 + \frac{4\pi^2}{L_o^2}\right)^{11/6}},\qquad(28)$$

where L_m and L_o represent the inner and outer turbulence scale sizes respectively. To determine the effect of the parameter L_o, the OTF value is evaluated for various values of L_o at a single spatial frequency. As noted before, this spatial frequency is related to the shift parameter $\vec{\rho}$ by $\vec{\rho} = \vec{v}\lambda f$. Figure 4 shows the effect of the outer scale size on the phase and amplitude OTFs for a typical Hufnagel-Valley atmosphere (21) evaluated at $|\vec{\rho}| = 1$ m and oriented parallel to $\vec{\vartheta}$. From Figure 4, it is seen that the effect on the phase OTF caused by differences in outer scale dimension are significant enough to warrant concern about the proper selection of L_o. In a similar manner, the effect of the inner scale on the OTF was studied. The

18

inner scale was found to cause insignificant changes in the OTF over all conceivable scale sizes. The remainder of this work utilizes scale sizes of $L_o = 5$ m and $L_m = 1$ mm.
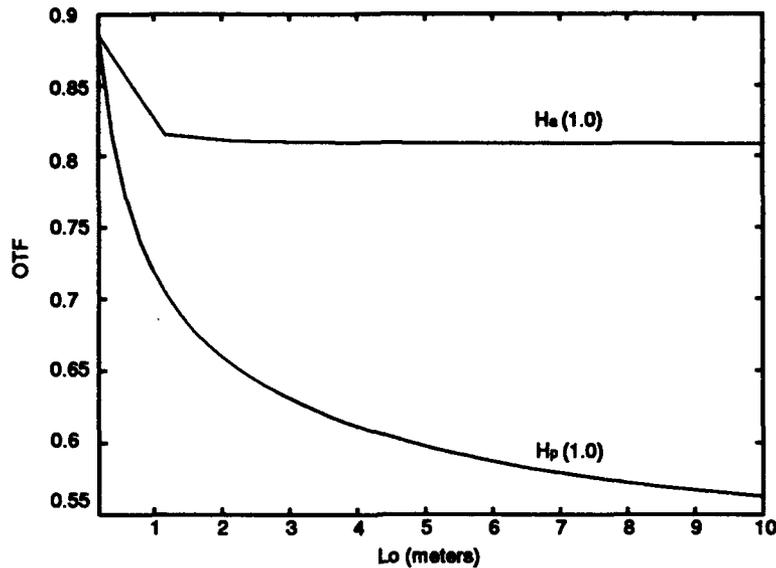
Figure 4. $H_a(1.0)$ and $H_p(1.0)$ versus L_o. This figure gives a measure of outer scale significance on the calculated OTF values. The OTFs are evaluated for $\rho = 1$ meter, $\vartheta = 2\mu$rad, and a Hufnagel–Valley atmosphere (21) with a 54 mph upper atmosphere wind.

2.6 Discrete atmospheric layers at preselected altitudes

Although Eqs. (18) and (27) are useful, they are time consuming to compute and do not lend a great deal of insight to the parameter dependences. The purpose of this section is to begin simplifying the OTF expressions by creating a layered atmosphere approximation to the continuous atmosphere. The result of this process will serve two purposes. First, by simplifying the OTF with respect to the atmospheric turbulence profile, an OTF is obtained that can be scaled with changing atmospheric parameters rather than completely recalculated. Second, notice that the integration within the OTFs of Eqs. (18) and (27) are over the altitude parameter η, and the two dimensional frequency vector $\vec{\kappa}$. By creating a layered atmospheric model, the integration over η can be replaced with a summation over the layers. Layering

19

the atmosphere can reduce the computation time by over 90% and still yield results that are within 1% of that obtained using a continuous atmosphere.

The subject of layering the atmosphere begins by considering the turbulence power spectrum, $\Phi(\vec{\kappa}, \eta)$. The power spectrum contains information regarding the frequency distribution of the index of refraction variations and the distribution of turbulence strength as a function of altitude. These two functional dependencies are commonly broken up as a turbulence strength profile represented by $C_n^2(\eta)$ and a normalized power spectral density $\Phi_o(\vec{\kappa})$ as (46)

$$\Phi(\vec{\kappa}, \eta) = 0.033 C_n^2(\eta) \Phi_o(\vec{\kappa}). \tag{29}$$

Several $C_n^2(\eta)$ turbulence profiles are shown in Figure 5 where $C_n^2(\eta)$ is given in units of meters$^{-2/3}$. The goal is to determine a discrete model representation of $C_n^2(\eta)$, where properly weighted turbulent layers are placed at specified altitudes.

Creating discrete turbulence layers is a standard function approximation problem where the function to be approximated is the $C_n^2(\eta)$ turbulence profile. The only issue is deciding when a good approximation has been obtained. For the diffraction calculations presented in this research, higher order moments of the layered model of the atmospheric turbulence must match the higher order moments of the continuous turbulence profile. For example, the first moment, called the center of mass, could be matched by either placing a single layer at exactly the center of mass of the continuous $C_n^2(\eta)$ profile, or by properly weighted layers somewhere on either side of the known center of mass. Higher order moments can be similarly matched. Two general techniques exist for accomplishing this type of approximation. The first, which utilizes Gaussian Quadrature (39), specifies both the location and the strength of the layers and for n layers will match $2n$ moments (the integrated value, or zeroth moment, plus the first $2n - 1$ moments). For the case where a $C_n^2(\eta)$ turbulence profile is known, and a layered equivalent atmosphere is desired, this is the best method available. This method was used to model many turbulence profiles, and it was found that by using only two discrete layers, OTFs were obtained that were within 1% of the OTFs calculated using a continuous $C_n^2(\eta)$ profile.

20
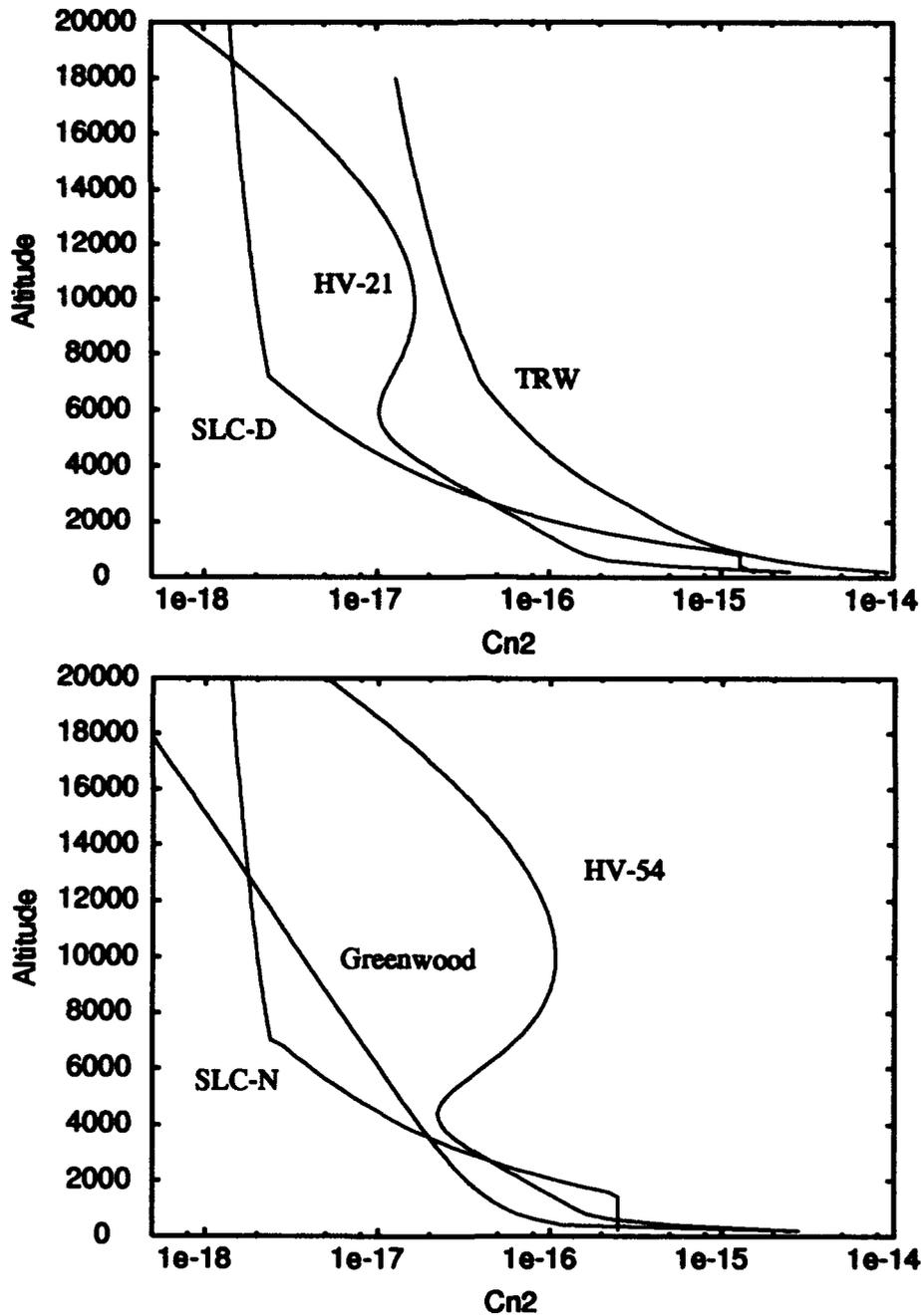
Figure 5. $C_n^2(\eta)$ Profiles: Model SLC-N represents a fit to the ARPA Maui Optical Station
(AMOS) night data (15, 35), and SLC-D represents a fit to the AMOS night data
with the addition of an altered boundary layer to simulate daytime conditions (15,
35). Model Greenwood is Greenwood's 'good seeing' model (15), and TRW is
a TRW high turbulence model for the Capistrano Test Site (CTS) environment.
HV-21 and HV-54 represent the Hufnagel–Valley model calculated with a 21 and
54 mph upper atmospheric wind, respectively (21).

21

One problem with using the Gaussian Quadrature method is that for a new C_n^2 turbulence profile, the algorithm must be reaccomplished to determine new layer strengths *and* altitudes. In order to obtain the full $2n$ matched moments, Gaussian Quadrature requires the extra degree of freedom of determining the altitude of the layers. This process is accurate but it does not allow the transfer function to be scaled for different atmospheric conditions. To accomplish the goal of a scalable transfer function, the altitudes of the turbulent layers must be fixed and then weights separately determined that will properly approximate the desired continuous $C_n^2(\eta)$ turbulence profile. This is accomplished by picking the altitudes and then solving the matrix equation

$$
\begin{bmatrix}
1 & 1 & \cdots & 1 \\
\eta_1 & \eta_2 & \cdots & \eta_n \\
\eta_1^2 & \eta_2^2 & \cdots & \eta_n^2 \\
\vdots & \vdots & \ddots & \vdots \\
\eta_1^{n-1} & \eta_2^{n-1} & \cdots & \eta_n^{n-1}
\end{bmatrix}
\begin{bmatrix}
W_1 \\
W_2 \\
\vdots \\
W_n
\end{bmatrix}
=
\begin{bmatrix}
1 \\
m_1 \\
m_2 \\
\vdots \\
m_{n-1}
\end{bmatrix},
\tag{30}
$$

where η_i represents the altitude of the ith layer, W_i is the weight (or percent of the integrated C_n^2 turbulence profile) for the ith layer, and m_i is the normalized i^{th} moment of the turbulence profile. This method allows us to specify the altitudes of the layers, but n layers only match the first n moments (the integrated value, or zeroth moment, plus the first $n-1$ moments). There are also constraints placed on the altitudes so as to ensure positive weights, but a discussion of these constraints are beyond the scope of this research. Here, it is sufficient to state that the choice of altitudes is flexible but not completely arbitrary. Using this method, it was found that the proper placing and weighting of four turbulent layers (altitudes of 200 m, 2 km, 10 km, and 18 km) could model most standard turbulence models and also yield OTFs that were within 1% of the OTFs calculated using a continuous atmosphere. The calculated weights for several different models are shown in Table 1 with the corresponding profiles being given in Figure 5.

Table 1. Weights for a 4-layered atmospheric model. Layer 1 is placed at 200 meters, layer 2 at 2 km, layer 3 at 10 km, and layer 4 at 18 km. W_i represents the weight of layer i as a percentage of the integrated turbulence, $\widehat{C}_n^2$. Model SLC-N represents a fit to the AMOS night data (15, 35), and SLC-D represents a fit to the AMOS night data with the addition of an altered boundary layer to simulate daytime conditions (15, 35). Model Greenwood is Greenwood's 'good seeing' model (15), and TRW is a TRW high turbulence model for the CTS environment. HV-21 and HV-54 represent the Hufnagel-Valley model calculated with a 21 and 54 mph upper atmospheric wind, respectively (21).

| Atmosphere | Layer 1 | | Layer 2 | | Layer 3 | | Layer 4 | | $\widehat{C}_n^2 10^{-12}$ | r_o |
Model	W_i	r_{oi} (cm)	W_i	r_{oi} (cm)	W_i	r_{oi} (cm)	W_i	r_{oi} (cm)	$m^{-2/3}$	cm
SLC-N	.4965	15.68	.4623	16.36	.0299	84.61	.0113	151.7	0.6879	10.3
SLC-D	.7397	6.063	.2513	11.59	.0048	124.6	.0042	135.0	2.220	5.06
Greenwood	.8615	8.420	.0980	31.03	.0394	53.60	.0011	458.8	1.078	7.7
TRW	.9254	1.718	.0466	11.33	.0262	16.01	.0017	82.60	13.57	1.8
HV-21	.8902	5.361	.0443	32.44	.0591	27.29	.0064	103.6	2.233	5.0
HV-54	.6877	5.258	.0204	43.40	.2554	9.526	.0365	30.61	2.953	4.2

The discrete layers allow the integral over η in Eq. (27) to be replaced with a summation over the layers. This leaves a phase OTF expression of

$$
\begin{aligned}
H_p(\vec{\rho}, \vec{\vartheta}) &= \exp\Big\{ -8\pi 0.033 k^2 \sum_{i=1}^{m} C_n^2(\eta_i) \int \Phi_o(\vec{\kappa}) \cos^2(\frac{\eta_i \kappa^2}{2k}) \\
&\quad \times \ [1 - \cos(\vec{\kappa} \cdot \vec{\rho})][1 - \cos(\eta_i \vec{\kappa} \cdot \vec{\vartheta})] d\vec{\kappa} \Big\} \\
&= \prod_{i=1}^{m} \exp\Big\{ -8\pi 0.033 k^2 C_n^2(\eta_i) \int \Phi_o(\vec{\kappa}) \cos^2(\frac{\eta_i \kappa^2}{2k}) \\
&\quad \times \ [1 - \cos(\vec{\kappa} \cdot \vec{\rho})][1 - \cos(\eta_i \vec{\kappa} \cdot \vec{\vartheta})] d\vec{\kappa} \Big\},
\end{aligned} \tag{31}
$$

where $C_n^2(\eta_i)$ represents the turbulence strength of the ith layer located at altitude η_i, and m is the number of turbulent layer. $C_n^2(\eta_i)$ can be replaced by a percentage of the integrated turbulence $W_i \widehat{C}_n^2$:

$$
C_n^2(\eta_i) = W_i \int C_n^2(\eta) d\eta = W_i \widehat{C}_n^2, \tag{32}
$$

where the integration is over the path from the source to the aperture plane. In the case of a source outside the atmosphere and an aperture on the ground, the integration is over the entire

23

vertical C_n^2 profile. This allows the phase OTF to be expressed as

$$H_p(\vec{\rho}, \vartheta) = \prod_{i=1}^{m} \exp\left\{ -8\pi 0.033 k^2 W_i \hat{C}_n^2 \int \Phi_o(\vec{\kappa}) \cos^2\left(\frac{\eta_i \kappa^2}{2k}\right) \right.$$

$$\left. \times \quad [1 - \cos(\vec{\kappa} \cdot \vec{\rho})][1 - \cos(\eta_i \vec{\kappa} \cdot \vec{\vartheta})] d\vec{\kappa} \right\}. \tag{33}$$

Following a similar analysis, the amplitude OTF, H_a, can be written as

$$H_a(\vec{\rho}) = \frac{1 + 4\pi 0.033 k^2 \hat{C}_n^2 \sum_{i=1}^{m} W_i \int \Phi_o(\vec{\kappa}) \sin^2(\eta_i \alpha) \cos(\vec{\kappa} \cdot \vec{\rho}) d\vec{\kappa}}{1 + 4\pi 0.033 k^2 \hat{C}_n^2 \sum_{i=1}^{m} W_i \int \Phi_o(\vec{\kappa}) \sin^2(\eta_i \alpha) d\vec{\kappa}}. \tag{34}$$

2.7 Simplified OTF calculations

Equations (33) and (34) represent the complete phase and amplitude OTF's for a layered atmosphere. However, they still require recalculation if the integrated turbulence or the distribution of turbulence changes. In this section, Eqs. (33) and (34) are simplified by incorporating Fried's coherence parameter (9), r_o, and introducing the concept of a scalable transfer function. This will allow OTFs to be quickly computed under changing atmospheric conditions.

Fried's coherence parameter is commonly used to describe the 'seeing' conditions of the atmosphere. It is known that the OTF of the atmosphere is roughly equivalent to the OTF resulting from an aperture with diameter r_o, where r_o is calculated from the relation

$$r_o = 0.185 \left(\frac{\lambda^2}{\hat{C}_n^2}\right)^{3/5}. \tag{35}$$

By incorporating Eq. (35) into Eq. (33), the 'seeing' condition is directly incorporated into the OTF:

$$
\begin{aligned}
H_p(\vec{\rho}, \vartheta) &= \prod_{i=1}^{m} \exp\left\{ -32\pi^3 0.033(0.185)^{5/3} \frac{W_i}{r_o^{5/3}} \int \Phi_o(\vec{\kappa}) \cos^2\left(\frac{\eta_i \kappa^2}{2k}\right) \right. \\
&\qquad\qquad \left. \times [1 - \cos(\vec{\kappa} \cdot \vec{\rho})][1 - \cos(\eta_i \vec{\kappa} \cdot \vec{\vartheta})]d\vec{\kappa} \right\} \\
&= \prod_{i=1}^{m} \left[\exp\left\{ -1.967 \int \Phi_o(\vec{\kappa}) \cos^2\left(\frac{\eta_i \kappa^2}{2k}\right) \right. \right. \\
&\qquad\qquad \left. \left. \times [1 - \cos(\vec{\kappa} \cdot \vec{\rho})][1 - \cos(\eta_i \vec{\kappa} \cdot \vec{\vartheta})]d\vec{\kappa} \right\} \right]^{\frac{W_i}{r_o^{5/3}}} \\
&= \prod_{i=1}^{m} \tilde{H}_{pi}(\vec{\rho}, \vartheta)^{\frac{1}{r_{oi}^{5/3}}},
\end{aligned}
\tag{36}
$$

where,

$$
\tilde{H}_{pi}(\vec{\rho}, \vartheta) = \exp\left\{ -1.967 \int \Phi_o(\vec{\kappa}) \cos^2\left(\frac{\eta_i \kappa^2}{2k}\right)[1 - \cos(\vec{\kappa} \cdot \vec{\rho})][1 - \cos(\eta_i \vec{\kappa} \cdot \vec{\vartheta})]d\vec{\kappa} \right\},
\tag{37}
$$

and, the parameter r_{oi} is defined as Fried's coherence parameter for layer i, where $r_{oi}^{-5/3} = W_i r_o^{-5/3}$. In Eq. (37), the term $\tilde{H}_{pi}$ can be thought of as the phase OTF for layer i calculated for an r_{oi} of 1 meter. Therefore, by calculating $\tilde{H}_{pi}$ a single time, we have a general phase OTF that can now be scaled to the actual turbulence profile through Eq. (36). The strength of the ith turbulence layer can be adjusted by varying r_{oi}. The overall value of r_o for all of the layers is related to the individual r_{oi}'s by (16)

$$
r_o^{-5/3} = \sum_{i=1}^{m} r_{oi}^{-5/3}.
\tag{38}
$$

The complete phase OTF is then found by scaling and multiplying the OTFs, $\tilde{H}_{pi}$, for each layer. Results obtained with this method are presented in Section 2.8.

No analogy to the simplifications obtained for the phase OTF exist for the amplitude OTF. This is due to the form of the amplitude OTF in Eq. (34). However, a similar analysis

yields

$$H_a(\vec{\rho}) = \frac{1 + \sum_{i=1}^{m} \frac{1}{r_{oi}^{5/3}} \tilde{\Gamma}_{ai}(\vec{\rho})}{1 + \sum_{i=1}^{m} \frac{1}{r_{oi}^{5/3}} \tilde{\Gamma}_{ai}(0)}, \tag{39}$$

with, $\tilde{\Gamma}_{ai}(\vec{\rho})$ representing a normalized amplitude correlation function for layer i and given by

$$\begin{aligned}
\tilde{\Gamma}_{ai}(\vec{\rho}) &= 16\pi^3 0.033(0.185)^{5/3} \int \Phi_o(\vec{\kappa}) \sin^2(\eta_i \alpha) \cos(\vec{\kappa} \cdot \vec{\rho}) d\vec{\kappa} \\
&= 0.983 \int \Phi_o(\vec{\kappa}) \sin^2(\eta_i \alpha) \cos(\vec{\kappa} \cdot \vec{\rho}) d\vec{\kappa}.
\end{aligned} \tag{40}$$

Amplitude OTF results are also presented in Section 2.8.

2.8 Numerical results

The purpose of this section is to provide representative results and to demonstrate the utility of the OTF equations derived in Section 2.7. In Sections 2.3 and 2.4, the amplitude and phase OTFs were derived for a continuous atmospheric C_n^2 profile. These OTF equations were derived using diffraction to account for both phase and amplitude variations in the corrected wavefront. The OTF equations accurately model the performance of the adaptive–optics system. However, the three dimensional integration is very time consuming. In Section 2.6, it was shown that by modeling the continuous atmosphere with discrete layers, one dimension of the OTF integration could be removed. Finally, Section 2.7, demonstrated how to create a set of normalized phase OTFs, $\tilde{H}_{pi}$, and normalized amplitude correlation functions, $\tilde{\Gamma}_{ai}$, that can be used to compute the overall OTF of the system through the use of the scaling parameters r_{oi}. The benefit of using $\tilde{H}_{pi}$ and $\tilde{\Gamma}_{ai}$ is that once these functions are calculated, the OTFs resulting from a wide range of atmospheric conditions can be calculated through the very simple scaling operations of Eq. (36) and Eq. (39).

This section demonstrates the ease of computing the OTFs by first generating a family of the curves for $\tilde{H}_{pi}$ and $\tilde{\Gamma}_{ai}$. A family of $\tilde{H}_{pi}$ curves is shown in Figure 6. These curves are created for an optical wavelength of 0.5 microns and an object angle, ϑ, of 2.4 μrad

26

for a 4 layered atmosphere with the inner scale set at $L_m = 1$ millimeter and the outer scale set at $L_o = 5$ meters. The object angle of 2.4 μrad is chosen to be equal to the isoplanatic angle as defined by Fried (10) for a Hufnagel–Valley atmosphere with a 54 mph upper atmosphere wind (21). This angle is chosen to allow the direct comparison with a geometric optics calculation discussed in Section 2.9. The curves in Figure 6 are computed such that when used in conjunction with Eq. (36) to obtain the complete phase OTF, r_{oi} in Eq. (36) is evaluated in units of centimeters. Once the $\tilde{H}_{pi}$ curves are created, the phase OTF for a wide range of atmospheric conditions can be computed by raising $\tilde{H}_{pi}$ to the $r_{oi}^{-5/3}$ power, and then multiplying the four OTFs together. This becomes a fast and convenient method for determining how a change in atmospheric conditions effects the phase OTF.
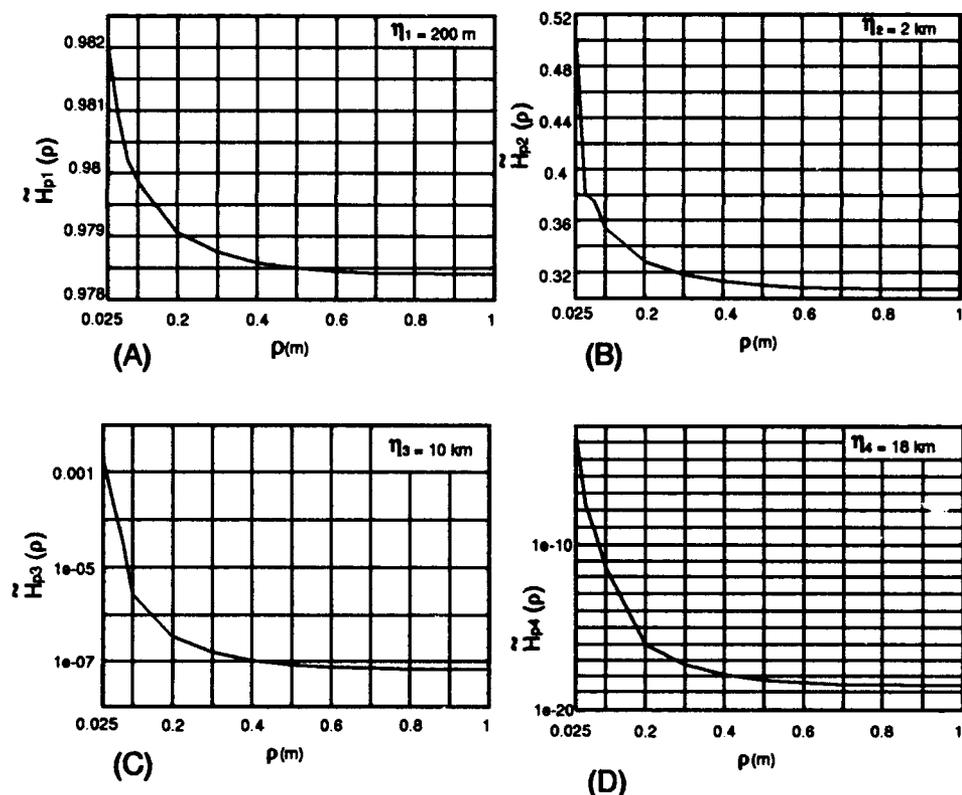
Figure 6. $\tilde{H}_{pi}(\rho)$ for turbulent layer located at A) 200 m, B) 2 km, C) 10 km, and D) 18 km. These OTFs are calculated for $\lambda = 0.5\mu$m, $\vartheta = 2.4\mu$rad, and $r_{oi} = 1$ cm.

27

For example, we want to calculate the phase OTF for a Hufnagel–Valley atmosphere with a 54 mph upper atmosphere wind and a ϑ of 2.4 μrad. We simply use the $\tilde{H}_{pi}$ curves plotted in Figure 6 and the values of r_{oi} given for HV-54 in Table 1 and evaluate the equation

$$
\begin{aligned}
H_p(\rho) &= \prod_{i=1}^{4} \tilde{H}_{pi}(\rho)^{\frac{1}{r_{oi}^{5/3}}} \\
&= (\tilde{H}_{p1}(\rho))^{5.258^{-5/3}} \cdot (\tilde{H}_{p2}(\rho))^{43.40^{-5/3}} \cdot (\tilde{H}_{p3}(\rho))^{9.526^{-5/3}} \cdot (\tilde{H}_{p4}(\rho))^{30.61^{-5/3}}.
\end{aligned}
$$

$$(41)$$

This calculation produces a curve that matches the OTF curve found in Figure 3 which required many computational hours to calculate using a continuous atmospheric C_n^2 turbulence profile.

In a similar manner, a family of curves can be created for calculating the amplitude OTF utilizing Eq. (39). Unfortunately, the amplitude OTF can't be scaled with the same ease as the phase OTF. However, by creating a family of curves for $\tilde{\Gamma}_{ai}(\rho)$, a simple method of calculating the overall amplitude OTF is obtained. Also, the process is somewhat simplified since the amplitude OTF is independent of ϑ. By evaluating Eq. (39) at a wavelength of 0.5 microns, the family of curves given in Figure 7 is obtained. Note that $\tilde{\Gamma}_{ai}(\rho)$ has a positive value at $\rho = 0$, and then quickly decays to zero. Knowledge of the general shape of $\tilde{\Gamma}_{ai}(\rho)$ and the amplitude OTF can be used to considerably simplify the numerical integration. It is known that $H_a(0) = 1.0$ and then falls off to a relatively constant value as shown in Figure 2 on page 15. Greater amounts of turbulence will not significantly change the cutoff point, but rather will change the constant value to which $H_a(\rho)$ decays. A comparison of Figures 7 and 2 shows that when the constant value of H_a is attained, $\tilde{\Gamma}_{ai}(\rho) \approx 0$. Therefore, a good approximation of the constant value is found using

$$
H_a(\rho) = \frac{1}{1 + \sum_{i=1}^{m} \frac{1}{r_{oi}^{5/3}} \tilde{\Gamma}_{ai}(0)}.
$$

$$(42)$$

The constant value attained by the amplitude OTF, designated $H_a(c)$, for a Hufnagel–Valley atmosphere with a 54 mph upper atmosphere wind is determined using the plotted
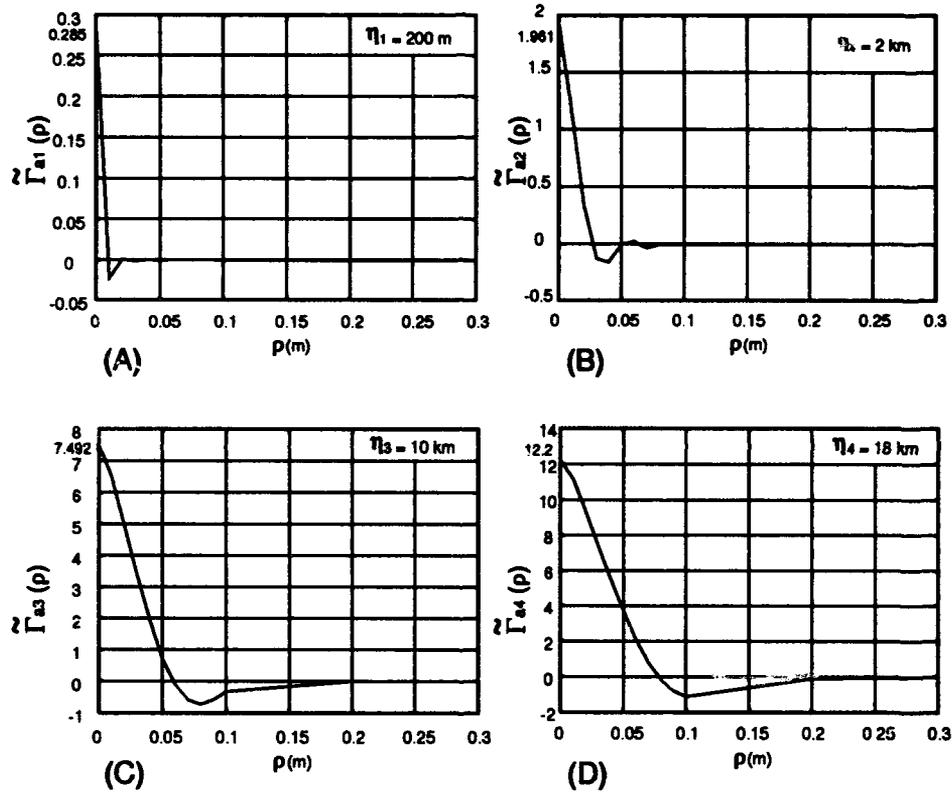
Figure 7. The normalized correlation function, $\tilde{\Gamma}_{ai}(\rho)$, for turbulent layer located at A) 200 m, B) 2 km, C) 10 km, and D) 18 km. These functions are calculated for $\lambda = 0.5\mu$m.

values for $\tilde{\Gamma}_{ai}(0)$ and the values of r_{oi} given for HV-54 in Table 1 and evaluating Eq. (42):

$$H_a(c) = \frac{1}{1 + \sum_{i=1}^{m} \frac{1}{r_{oi}^{5/3}} \tilde{\Gamma}_{ai}(0)} = 0.8082. \tag{43}$$

Again, this value compares very well with the constant value attained by $H_a(\rho)$ in Figure 2.

By using a small amount of memory to store the data points contained in $\tilde{H}_{pi}(\rho)$ and the values of $\tilde{\Gamma}_{ai}(0)$, complete OTFs can be calculated using a programmable calculator or plotted using a lap-top computer. The utility of this method is in rapid computations under changing atmospheric conditions.

2.9   Comparison between the diffraction and geometric optics OTF

In this section, two useful comparisons are made between the diffraction method and the geometric optics method of calculating the OTF of an adaptive–optics system. First, a direct comparison is made of the OTFs for a given atmosphere. In this comparison, the additional phase and amplitude information obtained through the diffraction method is highlighted. Second, the high frequency limit of the OTFs as a function of object angle, ϑ, is examined. It is common to define the isoplanatic angle as the angle, ϑ, where the OTF high frequency limit has fallen to $1/e$ of the $\vartheta = 0$ value (10). In this comparison it is shown that the diffraction method of calculation predicts a more optimistic isoplanatic angle.

In his discussion of atmospheric turbulence, Goodman (14) defines the 'near field' region where geometric optics is valid as the region where $\eta \ll \frac{\pi k}{|\vec{\kappa}|^2}$. This is the equivalent of stating that $\cos^2(\frac{\eta |\vec{\kappa}|^2}{2k}) \approx 1$ in the phase OTF expression of Eq. (27) and that $\sin^2(\frac{\eta |\vec{\kappa}|^2}{2k}) \approx 0$ in the amplitude OTF expression of Eq. (18). With the $\cos^2$ term of Eq. (27) set equal to one, and assuming a strict Kolmogorov power spectrum where $\Phi(\kappa, \eta) \propto \kappa^{-\frac{11}{3}}$, the integrations over $\vec{\kappa}$ can be solved analytically. As shown in Appendix E, the substitution of $\cos^2(\frac{\eta |\vec{\kappa}|^2}{2k}) = 1$ in the phase OTF expression of Eq. (27) yields the same OTF solution given by Fried using the geometric optics analysis (10). Also note that setting $\sin^2(\frac{\eta |\vec{\kappa}|^2}{2k}) = 0$ in Eq. (18) results in $H_a(\rho) = 1$ which is consistent with a geometric optics calculation.

30

One of the advantages to using a diffraction method to calculate the system OTF is that it allows for the separation of phase and amplitude effects. This is important because the adaptive–optics system is only correcting for phase effects. Figure 8 shows a direct comparison between the diffraction method of computing the OTF and the geometric optics method. In this figure, the 4 layered turbulence model, as discussed in the previous section, has been used with an optical wavelength of $\lambda = 0.5$ microns, a Hufnagel–Valley turbulence profile with a 54 mph upper altitude wind (21), an object angle of $\vartheta = 2.4\mu$rad, and a Von Karman refractive index power spectrum with $L_m = 1$mm and $L_o = 5$m. The geometric optics OTF was calculated using the same turbulence model and the same Von Karmon power spectrum but with the approximation of $\cos^2\left(\frac{\eta|\vec{\kappa}|^2}{2k}\right) = 1$. The diffraction method gives a better understanding of the atmospheric correction problem and helps quantify the level of improvement possible in the OTF. For example, from Figure 8 it is seen that, for this atmosphere, no matter how good the phase correction is, there will always be about a 20% attenuation due to the amplitude effects.
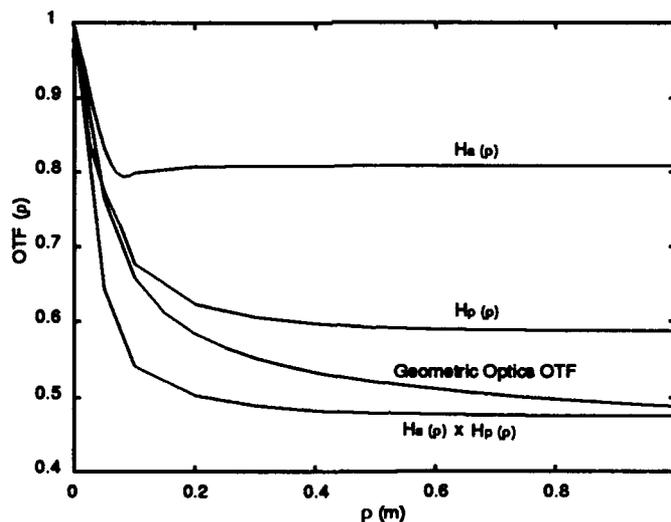
Figure 8. Comparison between diffraction theory and geometric optics theory. The diffraction OTFs are calculated with a 4 layered atmosphere at 200m, 2km, 10km, and 18km, $\lambda = 0.5\mu$m, a Hufnagel–Valley turbulence profile with a 54 mph upper altitude wind (21), $\vartheta = 2.4\mu$rad, and a Von Karman refractive index power spectrum with $L_m = 1$mm and $L_o = 5$m. The geometric optics OTF is calculated with the same atmospheric conditions but using the geometric optics approximation.

31

In adaptive–optics, the size of the isoplanatic angle or isoplanatic patch of the atmosphere is of interest. This is commonly thought of as an area of the atmosphere that has high correlation in the index of refraction. Therefore, a ray of light propagating at any angle through this portion of the atmosphere will receive approximately the same wavefront distortions. However, no two paths through the atmosphere will induce identical distortions. The isoplanatic angle is therefor the angle over which the difference in the distortions are 'not too large'. Fried established a method of quantifying this measure by defining the isoplanatic angle as the angle, ϑ, where the OTF high frequency limit has fallen to e^{-1} of the $\vartheta = 0$ value (10). This definition can be interpreted two different ways. First, since for the idealized system modeled here, geometric optics always calculates an OTF value of 1.0 at $\vartheta = 0$, the isoplanatic angle can be considered to be the angle at which the high frequency limit of the overall OTF has fallen to a value of e^{-1}. Second, recall that the adaptive–optics system is concerned only with the phase correctability. In this case, only the phase portion of the OTF is considered, and the isoplanatic angle is defined as the angle at which the high frequency limit of H_p has fallen to a value of e^{-1}. Figure 9 shows a comparison between the OTF high frequency limit using diffraction theory and the OTF high frequency limit using geometric optic theory for the same atmospheric conditions discussed above. We see that where geometric optics predicts an isoplanatic angle of 2.4μrad for this atmosphere, the diffraction theory indicates a greater value regardless of how the isoplanatic angle is defined. When the isoplanatic angle definition is taken to be the angle at which the high frequency limit of the overall OTF has fallen to a value of e^{-1}, the isoplanatic angle equals 3.1μrad. When the definition is taken to be the angle at which the high frequency limit of H_p has fallen to a value of e^{-1}, the isoplanatic angle equals 3.65μrad. It is easy to show that any atmosphere will yield a greater isoplanatic angle when a diffraction calculation is performed than when a geometric optics analysis is used.
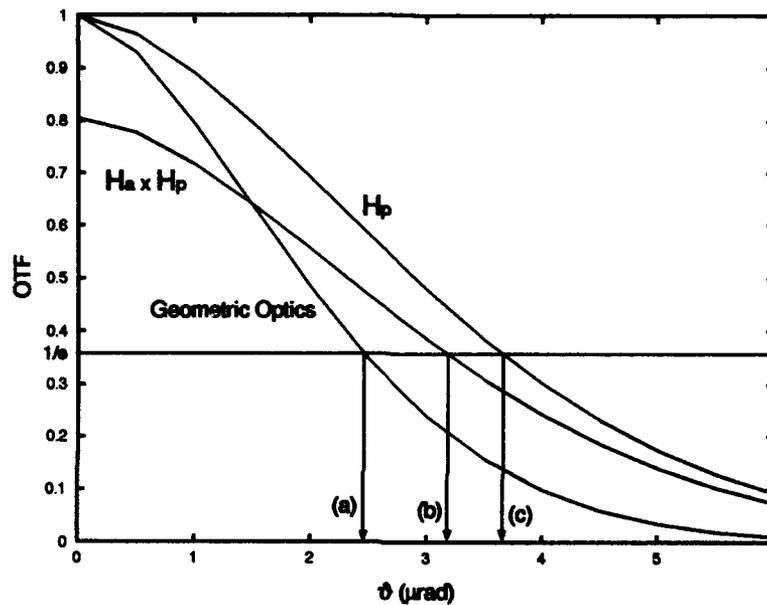
Figure 9.   Comparison of the OTF high frequency limit ($\rho = \infty$) between diffraction theory and geometric optic theory as a function of separation angle, ϑ. The diffraction OTFs are calculated with a 4 layered atmosphere at 200m, 2km, 10km, and 18km, $\lambda = 0.5\mu$m, a Hufnagel–Valley turbulence profile with a 54 mph upper altitude wind (21), and a Von Karman refractive index power spectrum with L_m = 1mm and L_o = 5m. The geometric optics OTF is calculated with the same atmospheric conditions but using the geometric optics approximation. (a) represents the isoplanatic angle calculated for geometric optics. (b) and (c) represent the isoplanatic angle computed with two different definitions for the diffraction method .

2.10 Summary and Conclusions

In this chapter a model is developed that allows for the derivation and evaluation of an angle dependent average OTF for an ideal adaptive-optics system. An expression is derived for a wavefront propagating through a turbulent atmosphere at an arbitrary angle, ϑ. The derived expression includes diffraction effects to properly account for phase and amplitude perturbations in the propagating wave. Expressions are then derived for the phase and amplitude correlation functions, $\Gamma_a(\vec{\rho})$ and $\Gamma_p(\vec{\rho}, \vartheta)$, and the average amplitude and phase OTFs, $\langle H_a(\vec{\rho}) \rangle$ and $\langle H_p(\vec{\rho}, \vartheta) \rangle$. These expressions are used in the evaluation of the SNR in Chapter III, the analysis of the PSF in Chapter IV, and the development of a new wavefront correction algorithm in Chapter V. All of the above expressions are generalized with respect to the refractive index power spectrum, $\Phi(\eta, \vec{\kappa})$. This generalization allows an analysis of performance effects as a function of the turbulent scale sizes. A useful method of computing $\langle H_a(\vec{\rho}) \rangle$ and $\langle H_p(\vec{\rho}, \vartheta) \rangle$ is also presented in this chapter. A layered atmosphere is created that results in an expression that can be scaled to arbitrary turbulent conditions. An actual OTF is then determined through a scaling term of $r_{oi}^{-5/3}$, where r_{oi} represents Fried's coherence parameter related to the ith layer (9, 16). This scaling method of evaluation allows rapid evaluation of the effect of changing atmospheric conditions. The advantage of using a diffraction theory is demonstrated in a comparison with geometric optics. It is shown that the diffraction method separates phase and amplitude effects and allows for determining the effect of various $C_n^2(\eta)$ profiles. When the $C_n^2(\eta)$ profile contains far-field turbulence, amplitude effects become significant and this method becomes essential for accurate calculations.

III. The angle dependent OTF signal-to-noise ratio (SNR)

3.1 Introduction

In this chapter, the work of Chapter II is extended by calculating the object angle dependent variance of the OTF. The variance is then used in conjunction with the average OTF to obtain a signal-to-noise ratio (SNR) performance measure (47). The SNR performance measure is particularly important when image reconstruction is used in conjunction with adaptive-optics imaging (43). In image reconstruction, knowledge of the system OTF can be used along with the measured image intensity to obtain an estimate of the actual object intensity.

To fully understand the motivation for computing the SNR, consider the linear, locally space-invariant, system model for incoherent adaptive-optics imaging. Let $i(\vec{x}, \vartheta)$ represent the measured image intensity, where $\vec{x}$ designates a point in the image and ϑ is the angle between the reference source and the object. The image $i(\vec{x}, \vartheta)$ can be related to the object being imaged, $o(\vec{x})$, by

$$i(\vec{x}, \vartheta) = o(\vec{x}) * h(\vec{x}, \vartheta), \tag{44}$$

where $h(\vec{x}, \vartheta)$ is the instantaneous, object angle dependent, point spread function (PSF) of the system and the notation * designates 2-dimensional convolution. Note that the object is considered to be the same object at any angle and is therefore not a function of ϑ. The problem of imaging an extended field-of-view with regard to the angle dependent PSF is examined in Chapter IV.

The relationship between the image and the object can be equivalently stated in the frequency domain as

$$I(\vec{\nu}, \vartheta) = O(\vec{\nu})H(\vec{\nu}, \vartheta), \tag{45}$$

where $\vec{\nu}$ is the spatial frequency variable and the capital letters I, O, and H are the Fourier transforms of i, o, and h, respectively. $H(\vec{\nu}, \vartheta)$ is the instantaneous OTF of the imaging system. In a deterministic system (i.e., a system in which the OTF is perfectly known),

35

the object spectrum $O(\vec{\nu})$, can be recovered out to the cutoff frequency of the system by multiplying the measured spectrum $I(\vec{\nu}, \vartheta)$ by the inverse of $H(\vec{\nu}, \vartheta)$:

$$O(\vec{\nu}) = I(\vec{\nu}, \vartheta)H^{-1}(\vec{\nu}, \vartheta). \tag{46}$$

However, imaging through the atmosphere produces an instantaneous OTF that is random. This randomness will be manifested as noise in the image measurement and will always tend to degrade the quality of the reconstructed image. The SNR, which is a measure of the variability or randomness of the OTF relative to it's mean value, provides a measure of the quality with which the spectral components of $H(\vec{\nu}, \vartheta)$ can be used to reconstruct the object spectrum in Eq. (46).

In Chapter II, it was shown how to compute the average OTF. However, the average OTF gives no indication as to how a single realization of the OTF can vary from the mean value. The SNR is used to quantify the fluctuations in the OTF and is defined as

$$\text{SNR}\{H(\vec{\nu}, \vartheta)\} = \frac{|\langle H(\vec{\nu}, \vartheta)\rangle|}{\sqrt{\text{Var}\{H(\vec{\nu}, \vartheta)\}}}, \tag{47}$$

where $\text{Var}\{H(\vec{\nu}, \vartheta)\}$ is the variance of $H(\vec{\nu}, \vartheta)$.

This chapter presents the first analysis to yield OTF SNR results that are a function of the angle between the reference beacon and the object. The analysis considers an ideal adaptive–optics system which is able to perfectly measure a wavefront phase from a reference beacon, and in turn perfectly apply this correction to the object wavefront. The diffraction based analysis of the average OTF and the corresponding correlation functions presented in Chapter II are fully utilized in this analysis.

The remainder of this chapter is organized as follows. Section 3.2 presents an analysis of the object angle dependent variance and SNR of the OTF. In Section 3.3, simplifications of the numerical computation process are presented. These simplifications allow solutions to

otherwise computationally prohibitive problems. Section 3.4 contains numerical results for a typical atmosphere. Finally, conclusions are presented in Section 3.5.

3.2 Derivation of variance and SNR expressions

In this section, an expression is derived for the variance of the OTF of an adaptive–optics system. The variance is designated $\mathrm{Var}\{H(\vec{\rho}, \vartheta)\}$, where $H(\vec{\rho}, \vartheta)$ represents the instantaneous system OTF. Once an expression for the variance is obtained, the SNR is calculated using Eq. (47).

Rather than computing $\mathrm{Var}\{H(\vec{\rho}, \vartheta)\}$ directly, the second moment of the OTF is established, and the variance is computed using

$$
\begin{aligned}
\mathrm{Var}\{H(\vec{\rho}, \vartheta)\} &= \langle |H(\vec{\rho}, \vartheta)|^2 \rangle - \langle H(\vec{\rho}, \vartheta) \rangle^2 \\
&= \langle |H(\vec{\rho}, \vartheta)|^2 \rangle - H_o^2(\vec{\rho}) \langle H_a(\vec{\rho}) \rangle^2 \langle H_p(\vec{\rho}, \vartheta) \rangle^2, \quad (48)
\end{aligned}
$$

where, $H_o(\vec{\rho})$ is the OTF of the optics, and $\langle H_a(\vec{\rho}) \rangle$ and $\langle H_p(\vec{\rho}, \vartheta) \rangle$ are the average amplitude and phase OTFs, respectively. The average phase and amplitude OTFs have been computed in Chapter II. However, the second moment of the OTF, $\langle |H(\vec{\rho}, \vartheta)|^2 \rangle$, still needs to be calculated. A combined phase and amplitude transmission screen, $t(\vec{x}, \vartheta)$, is used to represent the residual phase and amplitude perturbations of the corrected wavefront in the pupil of the adaptive–optics system. The transmission screen is given by

$$
t(\vec{x}, \vartheta) = t_a(\vec{x}) t_p(\vec{x}, \vartheta) = (1 + a(\vec{x})) \exp\{j\phi(\vec{x}, \vartheta)\}, \quad (49)
$$

where $a(\vec{x})$ represents the amplitude perturbations and $\phi(\vec{x}, \vartheta)$ represents the angle dependent residual phase in the pupil of the adaptive–optic system. The second moment of the OTF can

now be written as (14)

$$\langle |H(\vec{\rho},\vartheta)|^2 \rangle = \left\langle \frac{\left| \int d\vec{x} P(\vec{x}) P(\vec{x}-\vec{\rho}) t(\vec{x},\vartheta) t^*(\vec{x}-\vec{\rho},\vartheta) \right|^2}{\left| \int d\vec{x} |P(\vec{x}) t(\vec{x},\vartheta)|^2 \right|^2} \right\rangle$$

$$= \left\langle \frac{\int d\vec{x} P(\vec{x}) P(\vec{x}-\vec{\rho}) t(\vec{x},\vartheta) t^*(\vec{x}-\vec{\rho},\vartheta) \int d\vec{x}' P(\vec{x}') P(\vec{x}'-\vec{\rho}) t^*(\vec{x}',\vartheta) t(\vec{x}'-\vec{\rho},\vartheta)}{\int d\vec{x} P(\vec{x})^2 |t(\vec{x},\vartheta)|^2 \int d\vec{x}' P(\vec{x}')^2 |t(\vec{x}',\vartheta)|^2} \right\rangle,$$

(50)

where $P(\vec{x})$ is the real valued pupil function with a value of 1 when $\vec{x}$ is inside the aperture and 0 for $\vec{x}$ outside the aperture. The variable $a(\vec{x})$ in Eq. (49), is the zero mean, Gaussian, random variable representation of the amplitude perturbations of the field in the pupil. The variable $\phi(\vec{x},\vartheta)$ in Eq. (49), is the zero mean, Gaussian, random variable representation of the phase difference between the wavefronts of the reference beacon and the object. Note that the phase difference is dependent on the object angle, ϑ.

Next, the expected value of the fraction in Eq. (50), is assumed to be approximately equal to the expected value of the numerator divided by the expected value of the denominator (14). The integrations over the pupil function in Eq. (50) are represented in simplified form by

$$\iint_{P(\vec{x}-\vec{\rho})} d\vec{x} d\vec{x}' = \iint d\vec{x} d\vec{x}' P(\vec{x}) P(\vec{x}-\vec{\rho}) P(\vec{x}') P(\vec{x}'-\vec{\rho}).$$

(51)

Substituting Eq. (49) into Eq. (50) and using the assumption of independence between $a(\vec{x})$ and $\phi(\vec{x},\vartheta)$ gives

$$\langle |H(\vec{\rho},\vartheta)|^2 \rangle =$$
$$\frac{\iint_{P(\vec{x}-\vec{\rho})} d\vec{x} d\vec{x}' \langle (1+a(\vec{x}))(1+a(\vec{x}-\vec{\rho}))(1+a(\vec{x}'))(1+a(\vec{x}'-\vec{\rho})) \rangle}{}$$
$$\times \quad \langle e^{j\phi(\vec{x},\vartheta)} e^{-j\phi(\vec{x}-\vec{\rho},\vartheta)} e^{-j\phi(\vec{x}',\vartheta)} e^{j\phi(\vec{x}'-\vec{\rho},\vartheta)} \rangle$$
$$\overline{\iint_{P(\vec{x})} d\vec{x} d\vec{x}' \langle (1+a(\vec{x}))^2 (1+a(\vec{x}'))^2 \rangle}.$$

(52)

We now compute the three expected values in Eq. (52). Note that the third order moment of jointly Gaussian, zero mean random variables, U_i, is equal to zero and that the fourth order

moment is given by (40)

$$\langle U_1 U_2 U_3 U_4 \rangle = \langle U_1 U_2 \rangle \langle U_3 U_4 \rangle + \langle U_1 U_3 \rangle \langle U_2 U_4 \rangle + \langle U_1 U_4 \rangle \langle U_2 U_3 \rangle. \tag{53}$$

It can then be shown using Eq. (53) that the fourth order amplitude expectation in the numerator of Eq. (52) is given by

$$\langle (1 + a(\vec{x}))(1 + a(\vec{x} - \vec{\rho}))(1 + a(\vec{x}'))(1 + a(\vec{x}' - \vec{\rho})) \rangle =$$
$$(1 + \Gamma_a(\vec{\rho}))^2 + (1 + \Gamma_a(\Delta \vec{x}))^2 + (1 + \Gamma_a(\Delta \vec{x} + \vec{\rho}))(1 + \Gamma_a(\Delta \vec{x} - \vec{\rho})) - 2, \tag{54}$$

where $\Delta \vec{x} = \vec{x} - \vec{x}'$ and the correlation function, $\Gamma_a(\vec{\rho})$, is defined as

$$\Gamma_a(\vec{x} - \vec{x}') = \langle a(\vec{x}) a(\vec{x}') \rangle. \tag{55}$$

In a similar manner, the fourth order amplitude expectation in the denominator of Eq. (52) is computed to be

$$\langle (1 + a(\vec{x}))^2 (1 + a(\vec{x}'))^2 \rangle = (1 + \Gamma_a(0))^2 + 4\Gamma_a(\Delta \vec{x}) + 2\Gamma_a^2(\Delta \vec{x}). \tag{56}$$

Next, the fourth order moment is computed for of the exponential term in the numerator of Eq. (52). Since $\phi(\vec{x}, \vartheta)$ is a zero mean, Gaussian random variable, the fourth order moment can be written as

$$\langle e^{j\phi(\vec{x},\vartheta)} e^{-j\phi(\vec{x}-\vec{\rho},\vartheta)} e^{-j\phi(\vec{x}',\vartheta)} e^{j\phi(\vec{x}'-\vec{\rho},\vartheta)} \rangle =$$
$$\exp\left\{ -\frac{1}{2} \left\langle [(\phi(\vec{x}, \vartheta) - \phi(\vec{x} - \vec{\rho}, \vartheta)) - (\phi(\vec{x}', \vartheta) - \phi(\vec{x}' - \vec{\rho}, \vartheta))]^2 \right\rangle \right\}$$
$$= \exp\left\{ -\frac{1}{2} \left[\left\langle (\phi(\vec{x}, \vartheta) - \phi(\vec{x} - \vec{\rho}, \vartheta))^2 + (\phi(\vec{x}', \vartheta) - \phi(\vec{x}' - \vec{\rho}, \vartheta))^2 \right. \right. \right.$$
$$\left. \left. \left. - 2(\phi(\vec{x}, \vartheta) - \phi(\vec{x} - \vec{\rho}, \vartheta))(\phi(\vec{x}', \vartheta) - \phi(\vec{x}' - \vec{\rho}, \vartheta)) \right\rangle \right] \right\}. \tag{57}$$

Expanding the first two squared term in the exponent of Eq. (57) yields

$$\langle (\phi(\vec{x}, \vartheta) - \phi(\vec{x} - \vec{\rho}, \vartheta))^2 \rangle = 2\Gamma_p(0, \vartheta) - 2\Gamma_p(\vec{\rho}, \vartheta), \tag{58}$$

where the phase correlation, $\Gamma_p(\vec{\rho}, \vartheta)$, is defined as

$$\Gamma_p(\vec{x} - \vec{x}', \vartheta) = \langle \phi(\vec{x}, \vartheta) \phi(\vec{x}', \vartheta) \rangle. \tag{59}$$

The last term in the exponent of Eq. (57) can be expanded and written in terms of phase correlations in a straight forward manner. Equation (57) is now only a function of second order phase correlation functions and is given by

$$\langle e^{j\phi(\vec{x},\vartheta)} e^{-j\phi(\vec{x}-\vec{\rho},\vartheta)} e^{-j\phi(\vec{x}',\vartheta)} e^{j\phi(\vec{x}'-\vec{\rho},\vartheta)} \rangle = \exp\Big\{ 2\Gamma_p(\vec{\rho}, \vartheta) - 2\Gamma_p(0, \vartheta) + 2\Gamma_p(\Delta\vec{x}, \vartheta)$$
$$- \Gamma_p(\Delta\vec{x} + \vec{\rho}, \vartheta) - \Gamma_p(\Delta\vec{x} - \vec{\rho}, \vartheta) \Big\}, \tag{60}$$

where, $\Delta\vec{x}$ is the separation between correlation points (i.e., $\Delta\vec{x} = \vec{x} - \vec{x}'$). Equations (54), (56), and (60) are now combined to yield an expression for $\langle |H(\vec{\rho}, \vartheta)|^2 \rangle$. For convenience, the result is broken into numerator (Num) and denominator (Den) expressions:

$$\text{Num}\langle |H(\vec{\rho}, \vartheta)|^2 \rangle = (1 + \Gamma_a(\vec{\rho}))^2 \exp\{ 2\Gamma_p(\vec{\rho}, \vartheta) - 2\Gamma_p(0, \vartheta) \}$$
$$\times \iint_{P(\vec{x}-\vec{\rho})} d\vec{x} d\vec{x}' \Big(1 + \frac{(1 + \Gamma_a(\Delta\vec{x}))^2 + (1 + \Gamma_a(\Delta\vec{x} + \vec{\rho}))(1 + \Gamma_a(\Delta\vec{x} - \vec{\rho})) - 2}{(1 + \Gamma_a(\vec{\rho}))^2} \Big)$$
$$\times \exp\{ 2\Gamma_p(\Delta\vec{x}, \vartheta) - \Gamma_p(\Delta\vec{x} + \vec{\rho}, \vartheta) - \Gamma_p(\Delta\vec{x} - \vec{\rho}, \vartheta) \}, \tag{61}$$

and,

$$\text{Den}\langle |H(\vec{\rho}, \vartheta)|^2 \rangle = (1 + \Gamma_a(0))^2 \iint_{P(\vec{x})} d\vec{x} d\vec{x}' \left(1 + \frac{4\Gamma_a(\Delta\vec{x}) + 2\Gamma_a^2(\Delta\vec{x})}{(1 + \Gamma_a(0))^2} \right), \tag{62}$$

where the terms not dependent on $\vec{x}$ or $\vec{x}'$ have been factored outside the integration. Notice that when Eqs. (61) and (62) are combined as numerator and denominator, there are terms outside the integrals that correspond to $\langle H_a(\vec{\rho}) \rangle^2$ and $\langle H_p(\vec{\rho}, \vartheta) \rangle^2$ as shown in Eqs. (11)

40

and (21). Also note that the integration in Eq. (62) can be evaluated independent of $\vec{\rho}$ and ϑ. This independence is useful for the numerical analysis in Section 3.4.

Equations (61) and (62), are now combined and substituted into Eq. (48), to yield a final expression for the OTF variance as

$$\text{Var}\{H(\vec{\rho}, \vartheta)\} = \langle H_a(\vec{\rho}) \rangle^2 \langle H_p(\vec{\rho}, \vartheta) \rangle^2 \left(\Upsilon(\vec{\rho}, \vartheta) - H_o^2(\vec{\rho}) \right), \tag{63}$$

where $\Upsilon(\vec{\rho}, \vartheta)$ is defined by

$$\Upsilon(\vec{\rho}, \vartheta) =$$
$$\frac{\iint_{P(\vec{x}-\vec{\rho})} d\vec{x} d\vec{x}' \left\{ \left(1 + \frac{(1+\Gamma_a(\Delta\vec{x}))^2 + (1+\Gamma_a(\Delta\vec{x}+\vec{\rho}))(1+\Gamma_a(\Delta\vec{x}-\vec{\rho}))-2}{(1+\Gamma_a(\vec{\rho}))^2} \right) \times \exp\{2\Gamma_p(\Delta\vec{x}, \vartheta) - \Gamma_p(\Delta\vec{x}+\vec{\rho}, \vartheta) - \Gamma_p(\Delta\vec{x}-\vec{\rho}, \vartheta)\} \right\}}{\iint_{P(\vec{x})} d\vec{x} d\vec{x}' \left(1 + \frac{4\Gamma_a(\Delta\vec{x}) + 2\Gamma_a^2(\Delta\vec{x})}{(1+\Gamma_a(0))^2}\right)}$$

$$\tag{64}$$

It is now a simple matter to substitute Eq. (63) into Eq. (47) to obtain the desired object angle dependent SNR:

$$\text{SNR}\{H(\vec{\rho}, \vartheta)\} = \frac{H_o(\vec{\rho})}{\sqrt{\Upsilon(\vec{\rho}, \vartheta) - H_o^2(\vec{\rho})}}. \tag{65}$$

Note that the SNR is a function of the phase and amplitude correlation functions, Γ_p and Γ_a. The amplitude correlation, Γ_a, was derived in Chapter II with the result:

$$\Gamma_a(\vec{\rho}) = 4\pi k^2 \iint d\eta d\vec{\kappa} \Phi(\vec{\kappa}, \eta) \sin^2\left(\frac{\eta|\vec{\kappa}|^2}{2k}\right) \cos(\vec{\kappa} \cdot \vec{\rho}). \tag{66}$$

A typical amplitude correlation function is shown in Figure 10. The correlation function in Figure 10 is calculated for $\lambda = 0.5$ microns using a Hufnagel-Valley turbulence profile with a 54 mph upper atmospheric wind (21), and a Von Karman index of refraction power spectrum with inner scale set at 1 millimeter and the outer scale set at 5 meters.
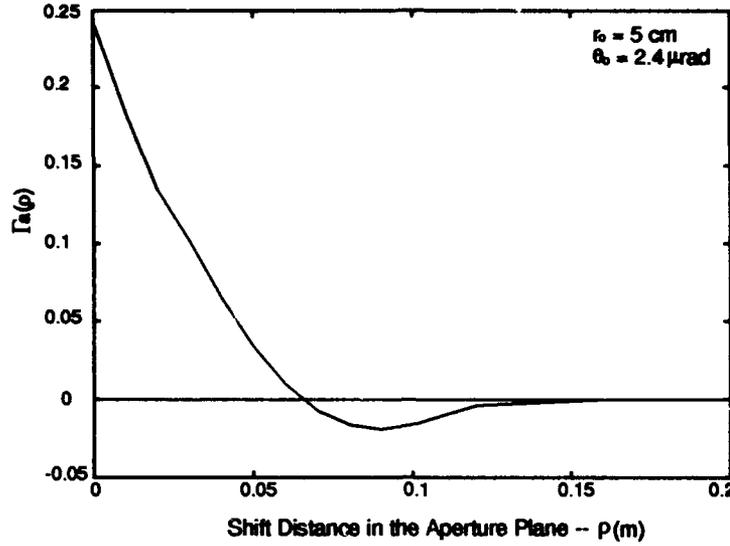
Figure 10.   Amplitude correlation function, $\Gamma_a(\rho)$, plotted versus ρ. This plot was calculated for $\lambda = 0.5$ microns using a Hufnagel–Valley turbulence profile with a 54 mph upper atmospheric wind. This turbulence profile has a Fried coherence cell size of $r_o = 5$ cm and an isoplanatic angle of $\theta_o = 2.4$ μrad.

The phase correlation, Γ_p, was also derived in Chapter II with the result:

$$\Gamma_p(\vec{\rho}, \vartheta) = 8\pi k^2 \int\!\!\int \Phi(\vec{\kappa}, \eta) \cos^2\left(\frac{\eta|\vec{\kappa}|^2}{2k}\right) \cos(\vec{\kappa} \cdot \vec{\rho})[1 - \cos(\eta\vec{\kappa} \cdot \vec{\vartheta})]d\eta d\vec{\kappa}. \qquad (67)$$

A typical phase correlation function is shown in Figure 11. The correlation function in Figure 11 is calculated for $\lambda = 0.5$ microns using a Hufnagel–Valley turbulence profile with a 54 mph upper atmospheric wind (21). The object angle ϑ is set equal to the isoplanatic angle, θ_o, as defined by Fried (10).

3.3   Simplifications for evaluation of the SNR

In this section, simplifications are presented that are required to numerically evaluate the SNR expression given in Eq. (65), and specifically the evaluation of $\Upsilon(\vec{\rho}, \vartheta)$ in Eq. (64). In the numerator of $\Upsilon(\vec{\rho}, \vartheta)$, the integration over $\vec{x}$ and $\vec{x}'$ is a four dimensional integration over an overlapping region of shifted pupil functions. Since the evaluation of the correlation functions, $\Gamma_a(\vec{\rho})$ and $\Gamma_p(\vec{\rho}, \vartheta)$, involve three dimensional integrations, as shown in Eqs. (66)

42
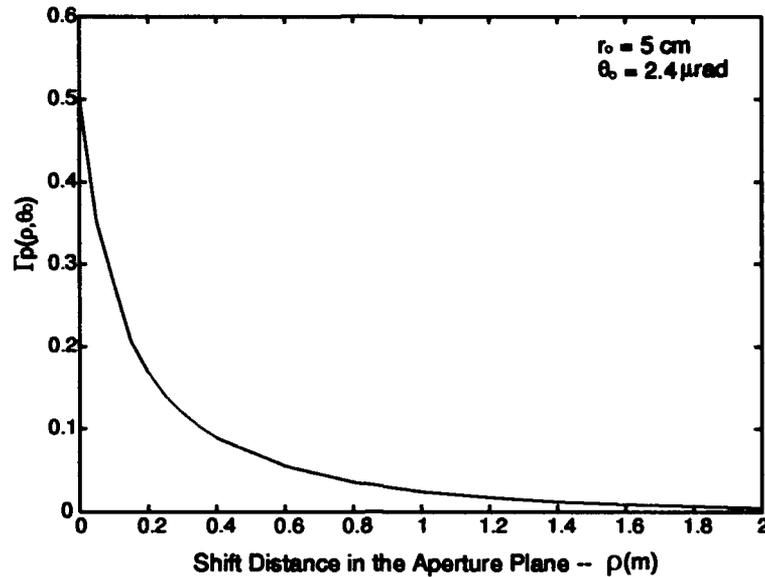
Figure 11.   Phase correlation function, $\Gamma_p(\rho, \vartheta)$, plotted versus ρ. This plot was calculated
for $\lambda = 0.5$ microns and $\vartheta = \theta_o$ using a Hufnagel-Valley turbulence profile with
a 54 mph upper atmospheric wind. This turbulence profile has a Fried coherence
cell size of $r_o = 5$ cm and an isoplanatic angle of $\theta_o = 2.4$ μrad.

and (67), the complete evaluation of $\Upsilon(\vec{\rho}, \vartheta)$ requires a seven dimensional integration. Even

with present day computational power, seven dimension numerical integration is extremely

intensive for all but very simply functions. In addition, the integrands of Eqs. (66) and (67)

are oscillatory and require relatively fine subdivisions to obtain convergence. It therefore

becomes computationally prohibitive to numerically integrate the function in its derived form.

The simplification process will be presented in two steps. First, a normalized version of

the correlation function will be derived. This will allow for scaling under changing atmospheric

conditions. Next an approximating function will be determined for the normalized correlation

functions. This process will allow for scaling under changing atmospheric conditions as well

as changing geometrical conditions (i.e., changing values of the object angle, ϑ).

3.3.1   The normalized correlation function for layered turbulence.   The first simplifi-

cation involves using a layered atmosphere as discussed in Section 2.6. By properly modeling

the atmospheric turbulence with relatively few discrete layers, the integration over the altitude

43

variable, η, in Eqs. (66) and (67) can be replaced with a summation over the number of layers. This is a significant simplification, but the evaluation of Eq. (64) still requires six dimensions of integration.

The next simplification is achieved by realizing that the correlation functions, Γ_a and Γ_p in Eq. (64), are simply functions of the shift vectors $\vec{\rho}$, $\Delta\vec{x}$, $\Delta\vec{x} + \vec{\rho}$, and $\Delta\vec{x} - \vec{\rho}$. Since the correlation functions are themselves integrations, they tend to be relatively smooth as a function of their argument. The smoothness of the correlation functions is shown in the plots of $\Gamma_a(\vec{\rho})$ and $\Gamma_p(\vec{\rho}, \vartheta)$ in Figures 10 and 11. Due to the smooth nature of the correlation functions, they can be represented over their complete argument range by a relatively sparse grid of precomputed values. The precomputed grid greatly reduces computation times and the smooth nature of the correlation functions allows simple bilinear interpolation between grid points to yield accurate approximations. The phase correlation function is found to be symmetric about the x and y components of the shift variable, $\vec{\rho}$, and the amplitude correlation function is circularly symmetric. These two symmetries reduce the number of grid points needed to completely characterize $\Gamma_a(\vec{\rho})$ and $\Gamma_p(\vec{\rho}, \vartheta)$. The evaluation of $\Upsilon(\vec{\rho})$ then involves four dimensional integration over an integrand that is precomputed on a grid of points. The integration in the numerator of Eq. (64) must be recomputed for each $\vec{\rho}$, but the denominator is independent of $\vec{\rho}$ and is only computed once.

Although this method of precomputing the correlation functions was necessary to obtain SNR results, creating the grid of points is still computationally intensive. Also, a disadvantage of precomputing the correlation functions is that the results are only valid for a single scenario, defined by the object angle, ϑ, and the particular atmospheric $C_n^2(\eta)$ profile. The quantity $C_n^2(\eta)$ is the altitude dependent structure constant of the refractive index fluctuations and is a measure of the strength and distribution of the turbulence. It would be useful to have a method of quickly computing the SNR that is not limited to a single scenario but is robust in both the choice of object angle, ϑ, and atmospheric $C_n^2(\eta)$ profile.

The first step in developing a robust analysis method is to model the atmosphere with a set of preselected turbulent layers. Section 2.6 demonstrated that four discrete layers placed at

44

200m, 2km, 10km, and 18km, is adequate for modeling a wide range of atmospheric profiles. Using a 4 layered atmospheric turbulence model, a normalized index of refraction power spectrum given by, $\Phi_o(\vec{\kappa}) = \frac{\Phi(\vec{\kappa})}{0.033C_n^2}$, and an analysis method similar to the development of Eqs. (36) and (39) in Chapter II, the correlation functions given in Eqs. (66) and (67) can be rewritten as

$$
\begin{aligned}
\Gamma_p(\vec{\rho}, \vartheta) &= 1.967 \sum_{i=1}^{4} \frac{1}{r_{oi}^{5/3}} \int \Phi_o(\vec{\kappa}) \cos^2\left(\frac{\eta_i|\vec{\kappa}|^2}{2k}\right) \cos(\vec{\kappa} \cdot \vec{\rho})[1 - \cos(\eta_i \vec{\kappa} \cdot \vec{\vartheta})]d\vec{\kappa} \\
&= \sum_{i=1}^{4} \frac{1}{r_{oi}^{5/3}} \tilde{\Gamma}_{pi}(\vec{\rho}, \vartheta),
\end{aligned} \tag{68}
$$

and,

$$
\begin{aligned}
\Gamma_a(\vec{\rho}) &= 0.9835 \sum_{i=1}^{4} \frac{1}{r_{oi}^{5/3}} \int \Phi_o(\vec{\kappa}) \sin^2\left(\frac{\eta_i|\vec{\kappa}|^2}{2k}\right) \cos(\vec{\kappa} \cdot \vec{\rho})d\vec{\kappa} \\
&= \sum_{i=1}^{4} \frac{1}{r_{oi}^{5/3}} \tilde{\Gamma}_{ai}(\vec{\rho}),
\end{aligned} \tag{69}
$$

where the parameter r_{oi} is defined as Fried's coherence parameter (9) for layer i located at altitude η_i and is a measure of the turbulence strength at that altitude. Values of r_{oi} for the 4 layer atmospheric model of several common atmospheric profiles are found in Table 1 on page 23.

3.3.2 Approximating the normalized correlation function. In Eqs. (68) and (69), the terms $\tilde{\Gamma}_{pi}$ and $\tilde{\Gamma}_{ai}$ represent the normalized correlations for layer i which are then scaled for the particular turbulence distribution through r_{oi}. This scaling allows a new SNR to be quickly recomputed when atmospheric conditions change (i.e., a changing turbulence distribution). However, the desired robustness with respect to the object angle has not yet been attained. Due to the ϑ dependence of the phase correlation function, $\tilde{\Gamma}_{pi}(\vec{\rho}, \vartheta)$ must be recomputed for every new object angle, ϑ. The robustness in object angle is accomplished by first computing $\tilde{\Gamma}_{pi}(\vec{\rho}, \vartheta)$ over a grid of points for several values of ϑ. The grid points are then used to obtain a single analytic function that approximates $\tilde{\Gamma}_{pi}(\vec{\rho}, \vartheta)$ over the range of ϑ's. Note that this

approximation for $\tilde{\Gamma}_{pi}(\vec{\rho}, \vartheta)$ will be a three dimensional function in ϑ, ρ, and θ_ρ, where ρ and θ_ρ represent the magnitude and angle of the shift, $\vec{\rho}$. The amplitude correlation function is independent of ϑ and circularly symmetric, consequently it is a much easier process to obtain a one dimensional fit in ρ that approximates the amplitude correlation data. For $\tilde{\Gamma}_{pi}(\vec{\rho}, \vartheta)$, the form of the approximating function found to yield accurate results is a rational polynomial given by

$$\tilde{\Gamma}_{pi}(\rho, \theta_\rho, \vartheta) \approx \frac{f_{1i}(\vartheta) + f_{2i}(\theta_\rho, \vartheta)\rho + f_{3i}(\theta_\rho, \vartheta)\rho^2}{1 + f_{4i}(\theta_\rho, \vartheta)\rho + f_{5i}(\theta_\rho, \vartheta)\rho^2 + f_{6i}(\theta_\rho, \vartheta)\rho^3}, \qquad (70)$$

where,

$$
\begin{aligned}
f_{1i}(\vartheta) &= a_{1i} + a_{2i}\vartheta + a_{3i}\vartheta^2 + a_{4i}\vartheta^3 + a_{5i}\vartheta^4, \\
f_{2i}(\theta_\rho, \vartheta) &= a_{6i} + a_{7i}\vartheta + (a_{8i} + a_{9i}\vartheta)\theta_\rho, \\
f_{3i}(\theta_\rho, \vartheta) &= a_{10i} + a_{11i}\vartheta + (a_{12i} + a_{13i}\vartheta)\theta_\rho, \\
f_{4i}(\theta_\rho, \vartheta) &= a_{14i} + a_{15i}\vartheta + (a_{16i} + a_{17i}\vartheta)\theta_\rho, \\
f_{5i}(\theta_\rho, \vartheta) &= a_{18i} + a_{19i}\vartheta + (a_{20i} + a_{21i}\vartheta)\theta_\rho, \\
f_{6i}(\theta_\rho, \vartheta) &= a_{22i} + a_{23i}\vartheta + (a_{24i} + a_{25i}\vartheta)\theta_\rho, \qquad (71)
\end{aligned}
$$

and, a_{ni} are the coefficients that must be found to best approximate $\Gamma_{pi}(\rho, \theta_\rho, \vartheta)$. The values of the coefficients are found using a non-linear least squares fitting routine that is slightly modified from the standard algorithm given in (39) for the inclusion of multiple dimensions. The coefficient values for each of the four layers are presented in Table 2 for a refractive index power spectrum that has been normalized to an r_o of 1 cm. It is determined that for accurate SNR results, it is best to limit the range of ϑ's in the approximating function. The coefficients in Table 2 are accurate for a range of object angles between 2 and 14 μrads and ρ out to 2 meters. Accurate SNR results can be obtained over a much larger range of ϑ by creating a piecewise set of approximating functions out to the desired ϑ.

46

Table 2. Coefficients for the phase correlation approximating function, $\tilde{\Gamma}_{pi}(\rho, \theta_\rho, \vartheta)$ for a 4 layered atmosphere. Layer 1 is placed at 200 meters, layer 2 at 2 km, layer 3 at 10 km, and layer 4 at 18 km. The units of ρ, θ_ρ, and ϑ, are meters, radians, and micro-radians, respectively. Using these units, r_{oi}, in Eq. (68) is given in units of centimeters.

Coefficient	Layer 1	Layer 2	Layer 3	Layer 4
a_1	0.67219E-02	0.40004E-01	0.45689E+01	-0.24508E+01
a_2	-0.49126E-02	-0.71964E-01	-0.32579E+01	0.23486E+01
a_3	0.42528E-02	0.20869E+00	0.34852E+01	0.72594E+01
a_4	-0.69582E-04	-0.45049E-02	-0.14006E+00	-0.36121E+00
a_5	-0.14925E-05	-0.30750E-04	0.74663E-03	0.45284E-02
a_6	0.85394E-03	0.10410E+02	-0.96750E+01	0.20650E+03
a_7	0.24471E-01	-0.57929E+01	-0.33821E+01	-0.15031E+03
a_8	-0.43777E+00	-0.12087E+02	-0.19866E+03	-0.23592E+03
a_9	0.30305E+00	0.79010E+01	0.15233E+03	0.16623E+03
a_{10}	0.57525E+00	-0.21106E+01	0.32366E+03	-0.16138E+02
a_{11}	-0.43740E+00	-0.11245E+00	-0.20472E+03	0.16954E+02
a_{12}	-0.27234E+00	0.27593E+01	-0.18859E+03	0.54170E+02
a_{13}	0.20937E+00	-0.13095E+01	0.11012E+03	-0.39813E+02
a_{14}	0.18175E+03	0.54659E+02	0.14392E+02	0.63275E+01
a_{15}	-0.41943E+01	-0.21243E+01	-0.10887E+01	-0.68352E+00
a_{16}	-0.30247E+02	-0.12206E+02	0.77047E+01	0.15286E+01
a_{17}	-0.36634E+00	0.43943E+00	-0.45722E-01	0.14112E+00
a_{18}	0.63805E+02	-0.81229E+01	0.13558E+03	0.35214E+02
a_{19}	-0.87324E+01	0.31468E+01	-0.4915ₒE+01	-0.93767E+00
a_{20}	0.35184E+03	0.48318E+02	-0.11003E+02	-0.76625E+01
a_{21}	-0.13716E+02	-0.32610E+01	-0.26197E+00	0.12417E+00
a_{22}	0.14140E+04	0.14184E+03	0.15687E+03	0.25237E+01
a_{23}	-0.66265E+02	-0.10011E+02	-0.76935E+01	-0.38129E+00
a_{24}	-0.48690E+03	-0.35202E+02	-0.14124E+02	0.40961E+01
a_{25}	0.23843E+02	0.33274E+01	0.10753E+01	-0.11481E+00

Table 3.   Coefficients for the amplitude correlation approximating function, $\tilde{\Gamma}_{ai}(\rho)$ for a 4 layered atmosphere. Layer 1 is placed at 200 meters, layer 2 at 2 km, layer 3 at 10 km, and layer 4 at 18 km. With the shift parameter, ρ, in units of meters, r_{oi}, is given in units of centimeters. Coefficients are valid for all shift values and all object angles.

Coefficient	Layer 1	Layer 2	Layer 3	Layer 4
b_1	0.15000E-01	0.5000E-01	0.1000E+00	0.1800E+00
b_2	0.28791E+00	0.19884E+01	0.75052E+01	0.12246E+02
b_3	-0.97345E+02	-0.30112E+02	-0.15856E+02	-0.72605E+01
b_4	-0.53476E+02	-0.11641E+03	-0.19928E+03	-0.23363E+03
b_5	0.10012E+05	0.11210E+04	0.32861E+03	0.13730E+00
b_6	0.22359E+04	0.15350E+04	0.12089E+04	0.97764E+03
b_7	0.12556E+03	-0.37670E+04	-0.16727E+04	0.10287E+04

For the amplitude correlation function, Γ_{ai}, the same rational polynomial form worked well for the approximating function. The form used is given by

$$\tilde{\Gamma}_{ai}(\rho) \approx \Big(u(\rho) - u(\rho - b_{1i})\Big)\frac{b_{2i} + b_{3i}\rho + b_{4i}\rho^2}{1 + b_{5i}\rho + b_{6i}\rho^2 + b_{7i}\rho^3}, \qquad (72)$$

where $u(\rho)$ is the unit step function with a value of one when the argument is greater than zero. The purpose of the combination of step functions is to limit the required range of the fitting function. It is determined that the value of the amplitude correlation function beyond $\rho = b_{1i}$ is approximately zero. The values of the seven coefficients for each of the four layers are given in Table 3 for a refractive index power spectrum normalized to an r_{oi} of 1 cm. The coefficients in Table 3 are accurate for all values of the shift parameter, ρ.

The end result is approximating functions given by $\tilde{\Gamma}_{pi}(\rho, \theta_\rho, \vartheta)$ and $\tilde{\Gamma}_{ai}(\rho)$ in Eqs. (70) and (72) that completely represent the phase and amplitude correlation functions of each of the four layers. These functions are valid over a wide range of object angle, ϑ, independent of the atmospheric $C_n^2(\eta)$ profile and yield extremely accurate SNR results. The approximating functions developed here for the purpose of evaluating the SNR of an adaptive–optics system can also be used to yield accurate calculations of $\langle H_p(\vec{\rho}, \vartheta)\rangle$ and $\langle H_a(\vec{\rho})\rangle$. Chapter II demonstrated how to combine and scale OTFs for individual layers for rapid evaluation of

the overall average OTF under changing atmospheric conditions. The use of $\tilde{\Gamma}_{pi}(\rho, \theta_\rho, \vartheta)$ and $\tilde{\Gamma}_{ai}(\rho)$, along with r_{oi}, allow $\langle H_p(\vec{\rho}, \vartheta) \rangle$ and $\langle H_a(\vec{\rho}) \rangle$ to be calculated through Eqs. (11) and (21). These OTFs can be rapidly evaluated under changing atmospheric conditions as well as the choice of object angle, ϑ.

3.4 Numerical results

In this section numerical results are presented for the OTF variance and SNR as defined in Section 3.2 by Eqs. (63) and (65) respectively. The theory developed in Sections 3.2 and 3.3 allow for calculations of the variance and SNR over a wide range of atmospheric conditions. However, in this section, results are calculated using a Hufnagel–Valley turbulence profile with a 54 mph upper atmospheric wind, $r_o = 5$ cm, and $\theta_o = 2.4$ μrad (21). The expressions in Eqs. (63) and (65) allow calculations for any orientation of $\vec{\rho}$, however, for the results presented here, the orientation of $\vec{\rho}$ is fixed to be along the x-axis of the pupil (i.e. $\theta_\rho = 0$). Recall that $\vec{\vartheta}$ is also assumed to be directed along the x-axis. Subsequent results will also consider $\vec{\rho}$ directed along the y-axis of the pupil (i.e. $\theta_\rho = \frac{\pi}{2}$).

Figures 12 and 13 plot the variance of the system OTF as a function of $\frac{\rho}{D}$, where D is the diameter of the imaging system aperture. The variance plotted in Figure 12 is for $D = 1$ meter and in Figure 13 for $D = 2$ meters. Each figure plots the variance for object angles, ϑ, of 1, 2, and 3 times the isoplanatic angle, θ_o. Note the general decrease in variance with increasing ϑ. By examining Eqs. (63) and (64), it is clear that the decrease is mainly due to the reduction in the phase OTF, $\langle H_p(\vec{\rho}, \vartheta) \rangle$. Also notice that the variance decreases with increasing aperture diameter. As the aperture diameter increases, the OTF is formed by the correlation of points that are separated by proportionately larger distances. The value of the OTF can be thought of as calculated through a type of averaging over all correlation values. As the separation between correlation points increases, the correlation value will decrease and tend toward zero with very little variance between individual realizations. Therefore, as the aperture diameter increases, the result of the 'averaging' over all the correlation contributions

will be a decrease in the overall variance. Again, by examining Eqs. (63) and (64), it can be shown that the variance approaches zero as the aperture diameter approaches infinity.

The corresponding SNR calculations are plotted in Figures 14 and 15. Once again, the SNRs are plotted as a function of $\frac{\rho}{D}$ for aperture diameters $D = 1$ and 2 meters and for object angles, $\vartheta = 1, 2$, and $3\theta_o$. In addition, Figure 14 shows a comparison between calculating the SNR using the method of precomputing the correlation function for each particular ϑ, and the method utilizing the approximating functions as discussed in Section 3.3. The two methods produce nearly identical SNR results.

One use of the SNR is found by defining the effective cutoff frequency of an adaptive-optics imaging system. The effective cutoff frequency, ρ_c, can be defined as the highest spatial frequency for which SNR(ρ) is greater than or equal to one:

$$\rho_c = \rho \quad such \quad that \quad \text{SNR}(\rho) = 1.0 \ . \tag{73}$$

The effective cutoff frequency can be thought of as the highest spatial frequency where the OTF is known with a minimum acceptable degree of certainty. To illustrate ρ_c for the results presented in Figures 14 and 15, a horizontal line is drawn at the level where SNR$\{H\} = 1$. Vertical lines indicate ρ_c for the particular values of ϑ. Notice that at $\vartheta = \theta_o$, ρ_c is near the diffraction limit for the particular aperture. This is consistent with Fried's definition of the isoplanatic angle where the wavefront phase of the object is expected to be well correlated with the wavefront phase of the beacon and therefore relatively correctable (10).

Note that the SNR significantly decreases as ϑ increases. This decrease is due to the dominant effect of the average OTF in the SNR calculation for a given aperture diameter. Recall that the SNR is the ratio of the average OTF to the square root of the variance. The average OTF decreases with increasing ϑ much faster than the decrease in the variance. These two figures also show that for the cases of ϑ equal to 1 and 2 θ_o, an aperture diameter of 2 meters yields a significantly increased SNR over an aperture diameter of 1 meter. For the $\vartheta = 2\theta_o$ case, the $SNR = 1$ frequency cutoff increases from 34 % to 55 % of the diffraction

50

limit as D increases from 1 to 2 meters. At $\vartheta = 2\theta_o$, the variance decreases faster than $\langle H_p(\vec{\rho}, \vartheta) \rangle$ in going from $D = 1$ to 2 meters. However, note that at $\vartheta = 3\theta_o$, the $SNR = 1$ cutoff frequency decreases in going from $D = 1$ to 2 meters. At $\vartheta = 3\theta_o$, $\langle H_p(\vec{\rho}, \vartheta) \rangle$ is dominating the SNR calculation. This type of evaluation is important in system design issues.

Figure 16 is a plot of $\frac{\rho_c}{D}$ as a function of ϑ/θ_o. This plot includes the $SNR = 1$ cutoff frequencies of Figures 14 and 15, and extends the cutoff frequency results out to $\vartheta = 6\theta_o$. Note that beyond $\vartheta = 3\theta_o$, the $SNR = 1$ cutoff frequency levels off at a value below 10 % of the diffraction limit.

Figure 17 shows the relation between the SNR as calculated for values of $\vec{\rho}$ along the x-axis and the SNR with $\vec{\rho}$ along the y-axis. The SNRs are plotted as a function of $\frac{\rho}{D}$ for an aperture diameter of 2 meters and for object angles, ϑ, of 1, 2, and $3\theta_o$. In each case the SNR has increased in moving from the shift axis parallel to $\vec{\vartheta}$, to the shift axis perpendicular to $\vec{\vartheta}$. The increased SNR along the perpendicular axis is expected since the phase correlation as well as the average phase OTF is larger along the perpendicular axis.
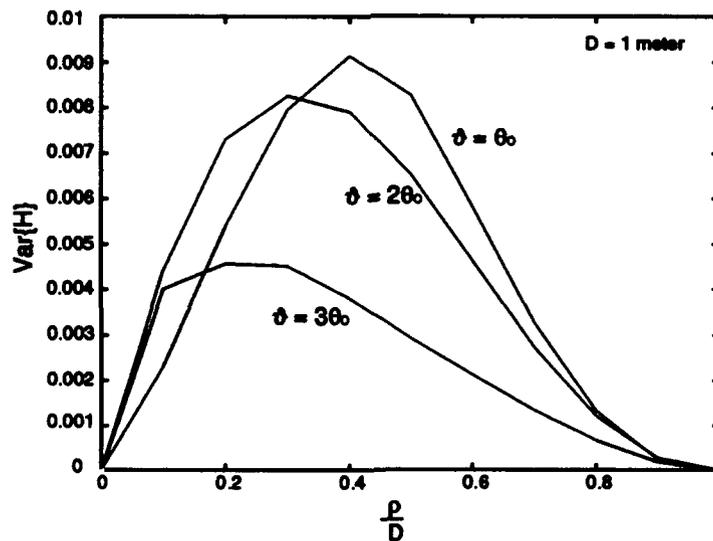
Figure 12. Variance of $H(\vec{\rho}, \vartheta)$ versus $\frac{\rho}{D}$ for $\lambda = 0.5$ microns using a Hufnagel–Valley turbulence profile with a 54 mph upper atmospheric wind, $r_o = 5$ cm, and D = 1 meter. Individual plots are for $\vartheta = 1, 2,$ and $3\theta_o$.
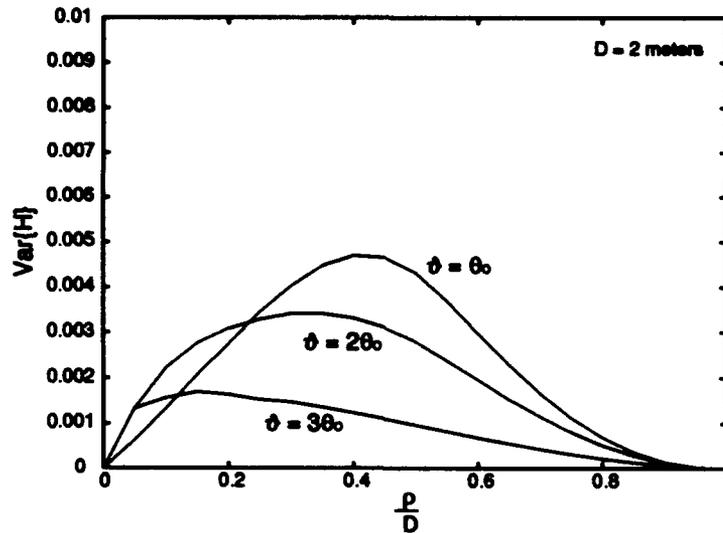
Figure 13. Variance of $H(\vec{\rho}, \vartheta)$ versus $\frac{\rho}{D}$ for $\lambda = 0.5$ microns using a Hufnagel–Valley turbulence profile with a 54 mph upper atmospheric wind, $r_o = 5$ cm, and $D = 2$ meters. Individual plots are for $\vartheta = 1, 2$, and $3\theta_o$.
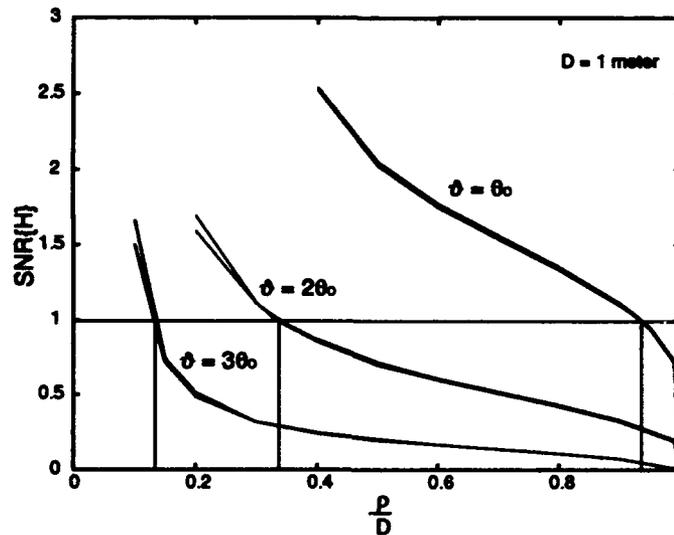
Figure 14. OTF SNR versus $\frac{\rho}{D}$ for $\lambda = 0.5$ microns using a Hufnagel–Valley turbulence profile with a 54 mph upper atmospheric wind, $r_o = 5$ cm, and $D = 1$ meter. Individual plots are for $\vartheta = 1, 2$, and $3\theta_o$. Note that double lines at each value of ϑ indicate relative accuracy of calculation method as stated in Section 3.4.

52
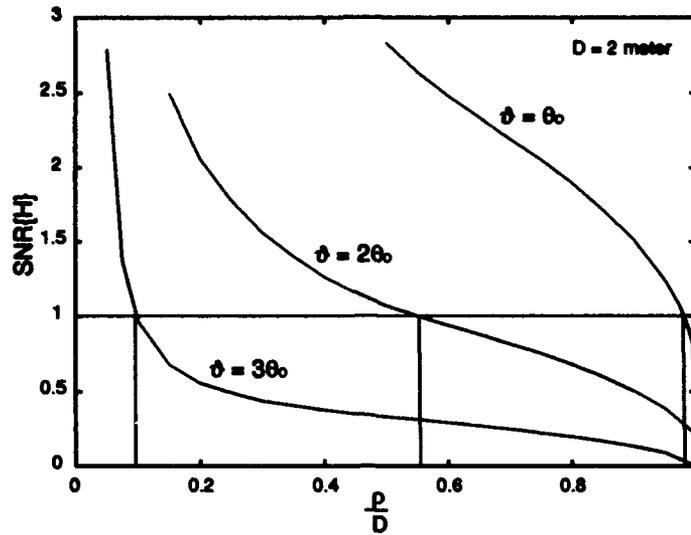
Figure 15.   OTF SNR versus $\frac{\rho}{D}$ for $\lambda = 0.5$ microns using a Hufnagel-Valley turbulence profile with a 54 mph upper atmospheric wind, $r_o = 5$ cm, and D = 2 meters. Individual plots are for $\vartheta = 1, 2,$ and $3\theta_o$.
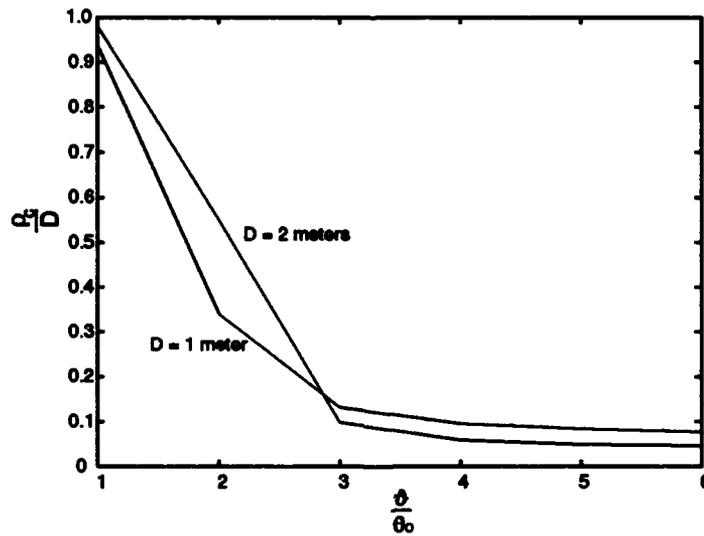
Figure 16.   Normalized cutoff frequency, $\frac{\rho_c}{D}$, vs. $\frac{\vartheta}{\theta_o}$. Data is calculated for $\lambda = 0.5$ microns using a Hufnagel-Valley turbulence profile with a 54 mph upper atmospheric wind and $r_o = 5$ cm.

53
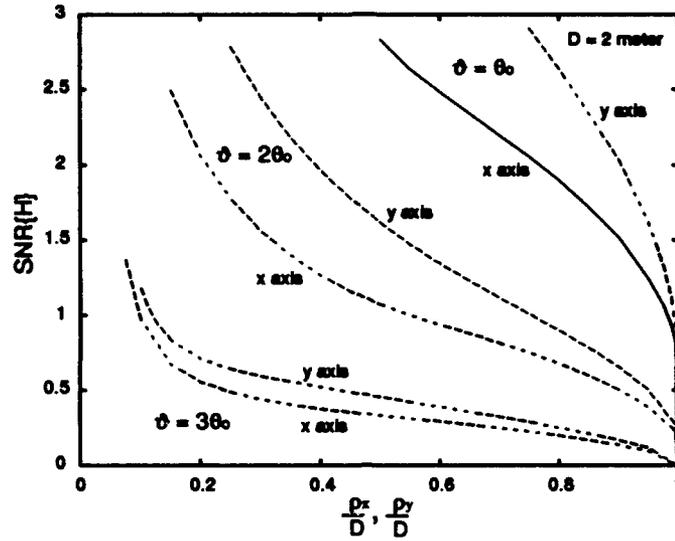
Figure 17. OTF SNR versus $\frac{\rho}{D}$ for $\lambda = 0.5$ microns using a Hufnagel–Valley turbulence profile with a 54 mph upper atmospheric wind, $r_o = 5$ cm, and D = 2 meters. Individual plots are for $\vartheta = 1$, 2, and $3\theta_o$. This figure compares the SNR calculated with $\vec{\rho}$ along the x-axis to the SNR calculated with $\vec{\rho}$ along the y-axis.

3.5   Summary and Conclusions

An analysis of the object angle dependent OTF signal-to-noise ratio, $\text{SNR}(\vec{\rho}, \vartheta)$, of an adaptive–optics system is presented in this chapter. This analysis allows for diffraction in the propagating wavefronts which accounts for both residual phase and amplitude effects. It is found that the SNR can be written in terms of second order correlations of the residual phase and amplitude in the system pupil given by $\Gamma_p(\vec{\rho}, \vartheta)$ and $\Gamma_a(\rho)$, respectively. The SNR analysis results in seven dimensional integrations. Simplifications are presented that utilize a layered atmospheric model and normalized approximation functions of $\Gamma_p(\vec{\rho}, \vartheta)$ and $\Gamma_a(\rho)$. The approximating functions are robust in the choice of ϑ, and can be scaled through Fried's coherence parameter related to the ith layer, r_{oi}. The layered atmospheric model and normalized approximating functions allow for relatively quick calculations under a wide range of atmospheric conditions and correction geometries. Numerical results are presented that demonstrate the utility of an SNR analysis as applied to an adaptive–optics imaging system.

IV. The angle dependent point spread function (PSF) and Strehl ratio

4.1 Introduction

This chapter presents an analysis of the angle dependent point spread function (PSF) and Strehl ratio. Knowledge of the PSF is useful in a conventional linear, shift invariant imaging system, because the image intensity is determined by convolving the PSF with the object intensity. However, since an adaptive-optics imaging system yields an angle dependent PSF, the system is not shift invariant. The image intensity of a non-shift invariant system is a superposition integral of the shift dependent PSF with the object intensity. In the somewhat simpler case of astronomical imaging where the image may be many stars in a wide field-of-view star field, each star may be considered a separate point source. Assuming that each star is separated from surrounding stars such that the corresponding PSFs do not overlap one another, the image of each star is simply the point source convolved with the PSF corresponding to the star's angular location. The angle dependent PSF results in each star within a star field having a slightly different spread or blur. The Strehl ratio is also a useful measure in adaptive-optics since it defines how much the peak of the PSF has been reduced compared to the peak of a diffraction limited PSF.

The organization of this chapter is as follows. A discussion of the analysis procedure for the PSF and Strehl ratio is presented in Section 4.2 followed by the results of the analysis for a particular atmospheric turbulence profile in Section 4.3. Finally, Section 4.4 summarizes this chapter and discusses the significance of the results.

4.2 Analysis

In general, the PSF is defined as the inverse Fourier Transform of the OTF. In Chapter II, the angle dependent OTF was derived. Therefore, the angle dependent PSF can be defined here as the inverse Fourier Transform of the angle dependent OTF. No attempt is made in this analysis to define an analytical expression for the angle dependent PSF. Rather, for a particular atmospheric turbulence profile, the OTF expression of Chapter II is used to create discrete

values of the angle dependent OTF which are then inverse Fourier transformed using standard Fast Fourier Transform (FFT) techniques. The resulting PSF is then examined with regard to the angular dependence. Since the OTF is not circularly symmetric, the PSF analyzed here will not be circularly symmetric. To explore the non–symmetric property of the PSF, 1–D slices of the 2–D PSF are plotted along the axis parallel to the object angle separation direction, $\vec{\vartheta}$, as well as along the perpendicular axis. The angular dependence of the spread of the PSF is shown by plotting the Full–Width–Half–Max (FWHM) as a function of the object angle, ϑ. As the name implies FWHM is a measure of how wide a function is when the value of the function has reached half of the maximum value.

The Strehl ratio is defined as the ratio of the peak of the PSF compared to the peak of a diffraction limited PSF. The Strehl ratio yields a single number that indicates the general performance of the adaptive–optics system. Also, when the Strehl ratio is plotted against object angle, ϑ, it is easily seen how performance degrades with increasing ϑ.

4.3   Results

The atmospheric profile used in this analysis is the same Hufnagel–Valley atmospheric profile with a 54 mph upper atmospheric wind (HV–54) used in previous chapters. Individual points of the atmospheric OTF were computed using the method discussed in Chapter II and multiplied by the diffraction limited OTF for a particular aperture to obtain an array of individual points for the overall system OTF. The resulting array of OTF values is inverse Fourier transformed using standard FFT techniques to obtain a 2–D array of PSF values.

Figure 18 is a plot of the PSF for the axes parallel and perpendicular to $\vec{\vartheta}$ for a 1 meter aperture. Figure 18 includes the diffraction limited PSF and the angle dependent PSF for object angles ranging from $\vartheta = 1$ to $6\theta_o$. Recall that θ_o is the isoplanatic angle for the given atmospheric turbulence profile. The isoplanatic angle for the HV–54, C_n^2 profile is 2.4μrad. The difference between the PSFs in Figure 18 for the parallel and perpendicular directions is difficult to see for the smaller ranges of ϑ. However, for the larger values of ϑ, a definite widening of the PSF can be seen along the parallel axis. The widening along the parallel axis

will cause the image of off-axis stars to contain an oval shape with the major axis aligned parallel to $\vec{\vartheta}$. Figure 19 plots the PSF for an aperture of $D = 2$ meters. A comparison of Figures 18 and 19 indicates that the PSF peak for the 2 meter aperture falls off faster, as a function of the object angle, than for the 1 meter aperture case. For example, at $\vartheta = 4\theta_o$, the PSF peak for the 1 meter aperture case is 0.027 and the PSF peak for the 2 meter case is 0.011. Recall that at $\vartheta = 0$, the PSF is only limited by the amplitude OTF attenuation. As a result, the PSF peak for the 2 meter aperture, at $\vartheta = 0$, will be much larger than the PSF peak for the 1 meter aperture. However, as ϑ increases, the coherence length of the atmospheric turbulence begins to dominate the PSF result. The dominance of the atmosphere will tend to drive the PSF peak for the 1 and 2 meter cases to the same values. The end result, after normalizing to the diffraction limited peak, is the faster fall off of the PSF peak for the 2 meter aperture case. Figure 20 is a plot of the Strehl ratio versus $\frac{\vartheta}{\theta_o}$. This plot again demonstrates the faster fall off of the PSF peak for the 2 meter aperture case as a function of increasing ϑ. Note that even at an object angle of $\vartheta = 0$, the Strehl ratio is down to 0.8 which reflects the attenuation in the amplitude OTF. Figure 21 plots the FWHM of the PSF, which has been normalized to the diffraction limited PSF, versus $\frac{\vartheta}{\theta_o}$. The FWHM is the full width of the PSF as evaluated at the point equal to half the PSFs maximum value. The FWHM value has been normalized such that the diffraction limited FWHM equals one. Figure 21 clearly shows the difference in the spread of the PSF for the axis parallel to $\vec{\vartheta}$ compared to the axis perpendicular to $\vec{\vartheta}$ for both the 1 and 2 meter case. This figure indicates that the PSF has a wider spread in the direction parallel to $\vec{\vartheta}$. It is also seen that the spread of the PSF increases at a faster rate for the 2 meter case than for the 1 meter case. Again, the increasing spread is an indication that at larger separation angles, atmospheric turbulence dominates the system performance.

4.4 Summary and Conclusions

An analysis of the angle dependent PSF and Strehl ratio for a particular atmospheric turbulence profile is presented in this chapter. The work presented in this chapter represents the first time an analysis of an angle dependent PSF that accounts for both amplitude and

phase effects in an adaptive–optics system has been presented. The results demonstrate the performance of the adaptive–optics system with respect to object angle out to a separation of $\vartheta = 6\theta_o$. It is seen that the spread of the PSF is wider along the axis parallel to $\vec{\vartheta}$ than along the axis perpendicular to $\vec{\vartheta}$. The non–symmetric spreading of the PSF results in a non–symmetric image of an off axis point source.
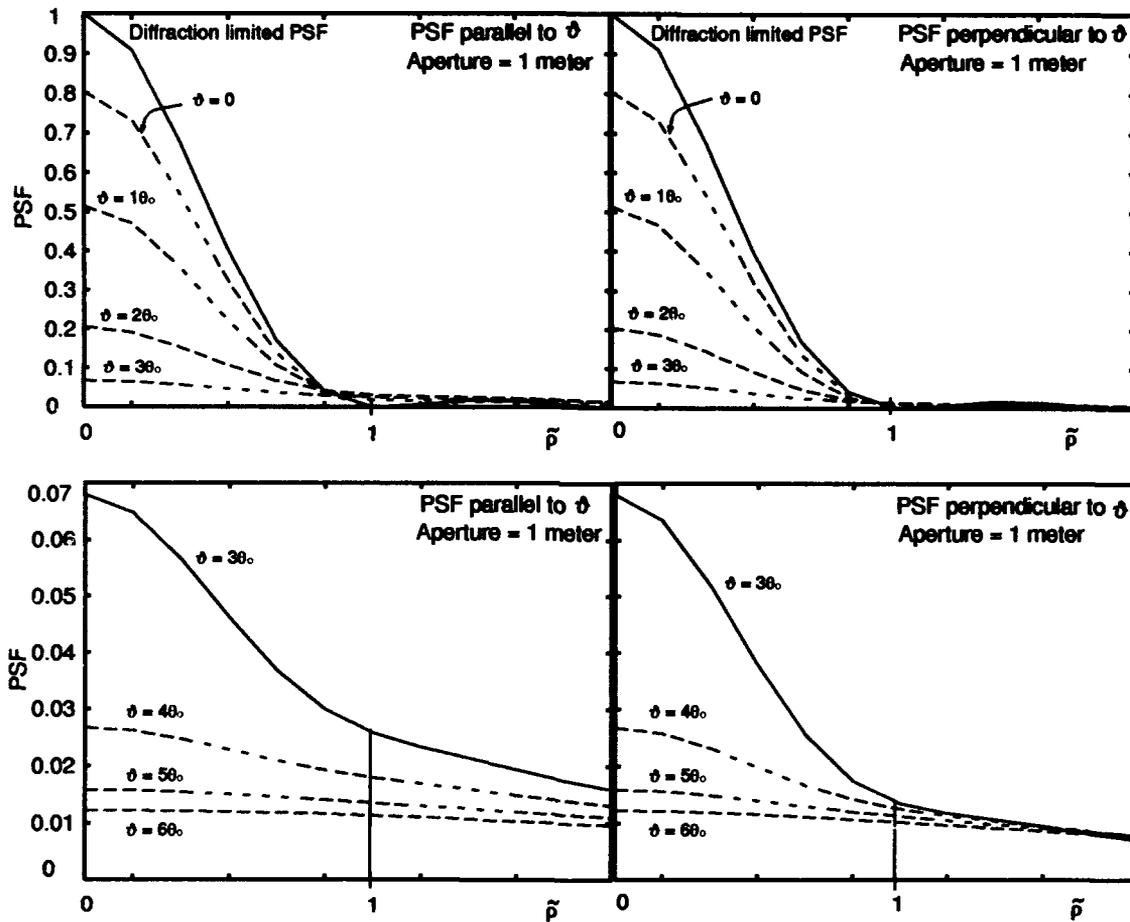
Figure 18. The system PSF plotted against a normalized spatial shift in the image plane for a 1 meter aperture and $\lambda = 0.5$ microns, using a Hufnagel-Valley turbulence profile with a 54 mph upper atmospheric wind and $r_o = 5$ cm. When $\tilde{\rho} = 1$, the spatial shift is equal to $\frac{1.22\lambda f_l}{D}$ where f_l is the focal length of the optics. Individual plots are for the diffraction limited PSF as well as for $\vartheta = 0$ to $3\theta_o$ in the upper plots and for $\vartheta = 3$ to $6\theta_o$ in the lower plots. This figure compares the PSF calculated with $\vec{\rho}$ parallel to $\vec{\vartheta}$ to the PSF calculated with $\vec{\rho}$ perpendicular to $\vec{\vartheta}$.
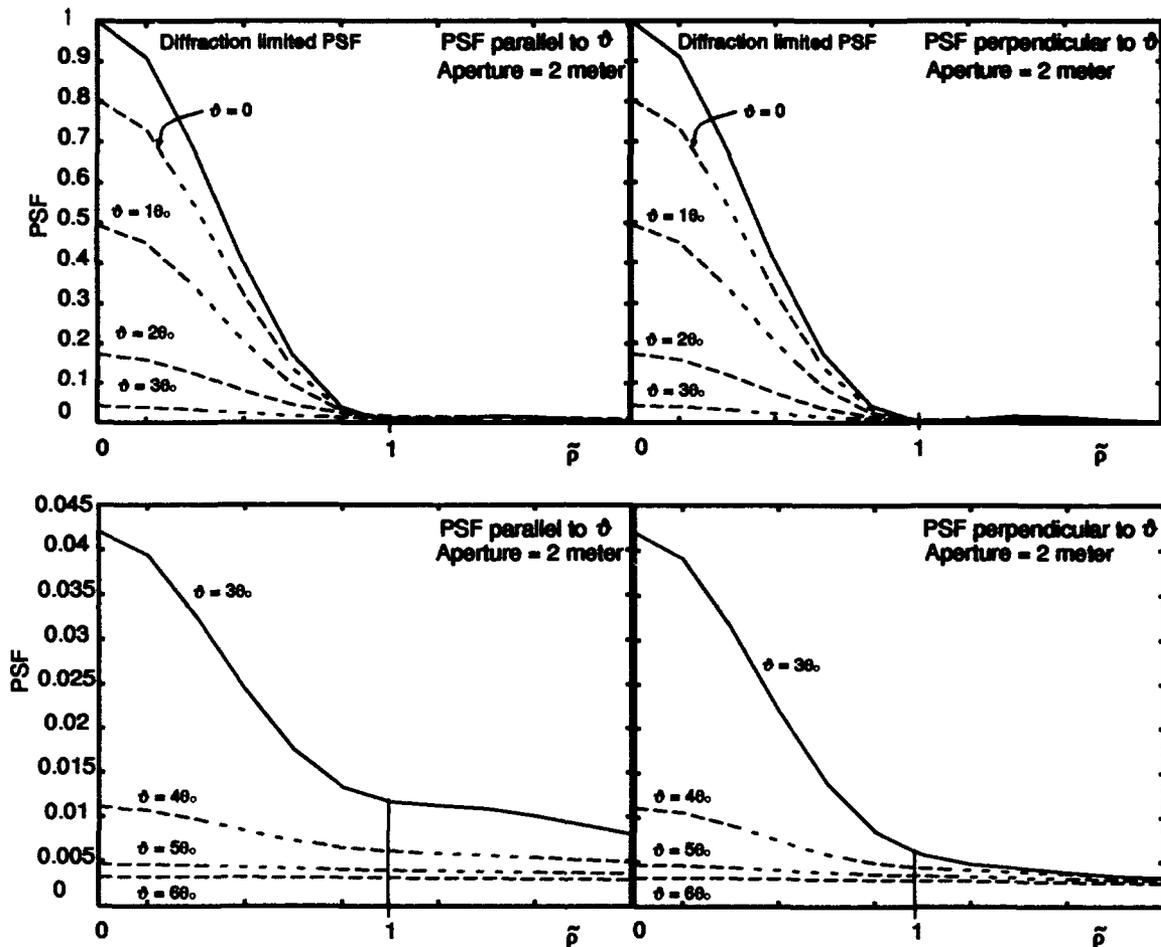
Figure 19. The system PSF plotted against a normalized spatial shift in the image plane for a 2 meter aperture and $\lambda = 0.5$ microns, using a Hufnagel–Valley turbulence profile with a 54 mph upper atmospheric wind and $r_o = 5$ cm. When $\tilde{\rho} = 1$, the spatial shift is equal to $\frac{1.22\lambda f_l}{D}$ where f_l is the focal length of the optics. Individual plots are for the diffraction limited PSF as well as for $\vartheta = 0$ to $3\theta_o$ in the upper plots and for $\vartheta = 3$ to $6\theta_o$ in the lower plots. This figure compares the PSF calculated with $\vec{\rho}$ parallel to $\vec{\vartheta}$ to the PSF calculated with $\vec{\rho}$ perpendicular to $\vec{\vartheta}$.

59
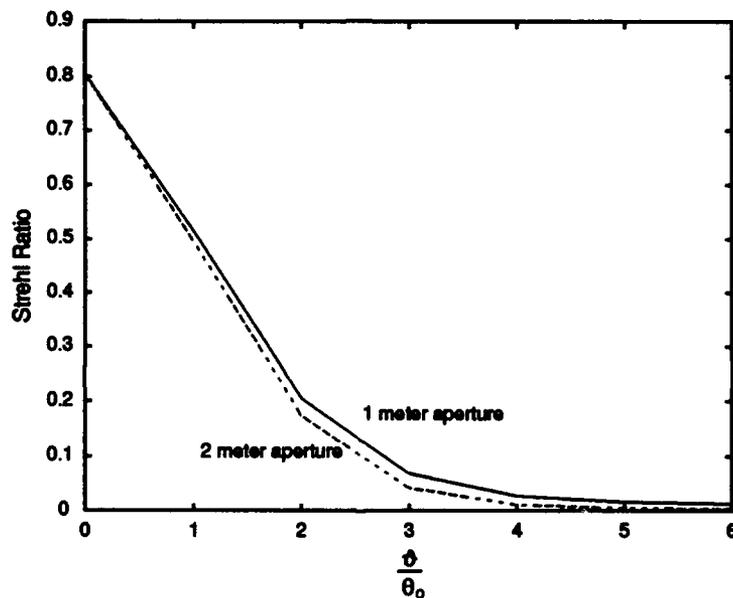
Figure 20. The Strehl Ratio as plotted against $\frac{\vartheta}{\theta_o}$ which represents multiples of the isoplanatic angle for $\lambda = 0.5$ microns using a Hufnagel–Valley turbulence profile with a 54 mph upper atmospheric wind and $r_o = 5$ cm. Individual plots are results for 1 and 2 meter apertures.
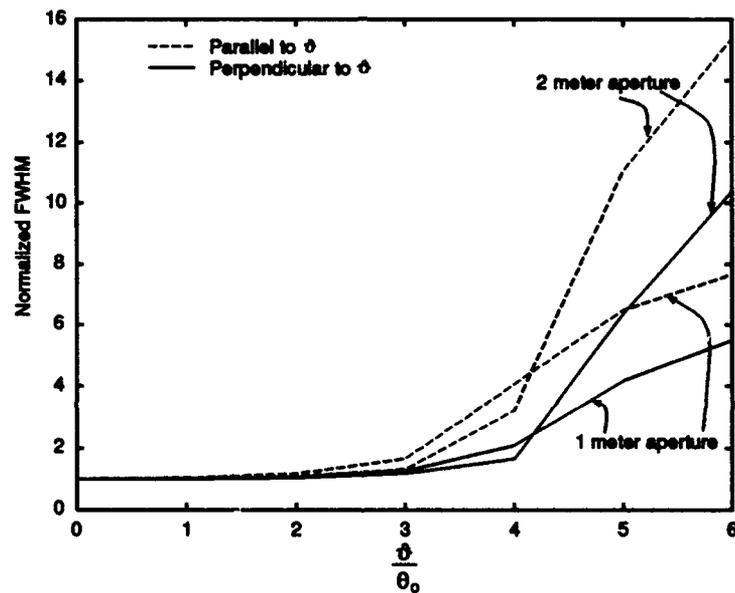
Figure 21. FWHM of the PSF, normalized to the diffraction limited PSF, as plotted against $\frac{\vartheta}{\theta_o}$ which represents multiples of the isoplanatic angle. The PSF is calculated with $\lambda = 0.5$ microns using a Hufnagel–Valley turbulence profile with a 54 mph upper atmospheric wind and $r_o = 5$ cm. This figure compares the FWHM of the PSF calculated with $\vec{\rho}$ parallel and perpendicular to $\vec{\vartheta}$ for both the 1 and 2 meter aperture case.

V. Improved performance through a new wavefront correction algorithm

5.1 Introduction

The purpose of this chapter is to develop a new wavefront correction algorithm for adaptive-optics systems that extends the correctable field-of-view (FOV). The FOV is defined as the maximum angle where good correction is attainable. Therefore, the FOV is defined by the isoplanatic angle as discussed in Chapter II. The extension of the FOV is accomplished using information obtained through the diffraction-based propagation model developed in Chapter II.

Current correction algorithms involve measuring the reference wavefront phase in the pupil and then reconstructing the negative of the measured phase. The reconstructed phase is then applied as a correction to an object wavefront. In such a correction algorithm, the same correction will be applied regardless of the object angle, ϑ. The development in Chapter II indicates that information is known regarding the difference between the phase of the reference wavefront and the phase of the object wavefront. This information can be used to formulate a better method of applying a wavefront correction. The quality of the new correction algorithm will be judged by the resulting phase OTF of the adaptive-optics system. Recall, from Chapter II, that the amplitude OTF will not be affected by the phase correction. The increase in the FOV will be determined by the size of the resulting isoplanatic angle as defined in Chapter II.

The remainder of this chapter is organized as follows. Section 5.2 develops the new wavefront correction algorithm. This development identifies the difference between the reference and object phase, and uses knowledge of the difference to apply a better correction to the object wavefront. Section 5.3 tests the new correction algorithm by calculating the OTFs and corresponding isoplanatic angles for two different atmospheric profiles. Finally, a summary of this chapter is presented in Section 5.4.

5.2 New wavefront correction derivation

Currently, a wavefront is corrected by subtracting the measured phase of a reference wavefront from the phase of an object wavefront. The subtraction is accomplished in the pupil of the adaptive-optics system. The phase of the reference and object wavefronts due to a single spatial frequency component of a single phase screen located at altitude η was developed in Chapter II and is again presented here:

$$P_{ref}(\eta, \vec{\kappa}, \vec{x}) = -A(\eta, \vec{\kappa}) \cos(\eta\alpha) \cos(\vec{\kappa} \cdot \vec{x} + \phi_o(\eta, \vec{\kappa})), \qquad (74)$$

and,

$$P_{obj}(\eta, \vec{\kappa}, \vec{x}, \vec{\vartheta}) = -A(\eta, \vec{\kappa}) \cos(\eta\alpha) \cos(\eta\beta - (\vec{\kappa} \cdot \vec{x} + \phi_o(\eta, \vec{\kappa}))), \qquad (75)$$

where, $\alpha = \frac{|\vec{\kappa}|^2}{2k}$, $\beta = \vec{\kappa} \cdot \vec{\vartheta}$, k is the wavenumber of the propagating wave, and $\vec{\vartheta}$ is the angle between the object and the reference source as shown in Figure 1 on page 4. Note that the only difference between the reference phase and the object phase is the $\eta\beta$ term contained in the argument of the cos in Eq. (75). The $\eta\beta$ term represents additional information regarding the phase of the wavefronts not used by conventional correction algorithms. If the atmospheric turbulence was composed of a single phase screen with a single frequency component, its easy to see that a wavefront correction algorithm would achieve perfect correction if a phase shift $\eta\beta$ is added to $P_{ref}(\eta, \vec{\kappa}, \vec{x})$ be^f applying the correction to $P_{obj}(\eta, \vec{\kappa}, \vec{x}, \vec{\vartheta})$. Since the atmospheric turbulence is not c⌀ ⌀d of a single phase screen, a separate shift would need to be added to each phase contribution from every phase screen to obtain the perfect correction. This would require the ability to determine the contribution of every phase screen to the measured cumulative phase distortion. Johnston's work with multi-conjugate adaptive-optics (MCAO) faced a similar challenge (23, 24, 25). However, determining the altitude related contributions to a measured wavefront is currently a theoretical exercise requiring the use of an array of laser guide stars. Another alternative is to choose a specific η, given by η_o, and use $\eta_o\beta$ as the shifting parameter for all phase screen altitudes. Note that the $\eta_o\beta$

shift parameter is not a function of altitude, but is still a function of spatial frequency since $\beta = \vec{\kappa} \cdot \vec{\vartheta}$.

With an $\eta_o \beta$ shift added to the reference phase, the new reference phase, $\tilde{P}_{ref}$ is written as

$$\tilde{P}_{ref}(\eta, \vec{\kappa}, \vec{x}) = -A(\eta, \vec{\kappa}) \cos(\eta \alpha) \cos(\eta_o \beta - (\vec{\kappa} \cdot \vec{x} + \phi_o(\eta, \vec{\kappa}))). \tag{76}$$

The residual phase of the adaptive optical system is determined by subtracting the phase of the new reference wavefront from the wavefront phase of the object. This residual phase is now given by

$$\begin{aligned} \Delta P_p(\eta, \vec{\kappa}, \vec{x}, \vec{\vartheta}) &= -A \cos(\eta \alpha) \cos(\eta \beta - (\vec{\kappa} \cdot \vec{x} + \phi_o(\vec{\kappa}))) \\ &\quad + A \cos(\eta \alpha) \cos(\eta_o \beta - \vec{\kappa} \cdot \vec{x} + \phi_o(\vec{\kappa})). \end{aligned} \tag{77}$$

Following a similar analysis as given in Chapter II, the resulting phase OTF is found to be

$$\begin{aligned} H_p(\vec{\rho}, \vec{\vartheta}) &= \exp\Big\{ -8\pi k^2 \iint \Phi(\vec{\kappa}, \eta) \cos^2(\frac{\eta |\vec{\kappa}|^2}{2k})[1 - \cos(\vec{\kappa} \cdot \vec{\rho})] \\ &\quad \times [1 - \cos((\eta - \eta_o)\vec{\kappa} \cdot \vec{\vartheta})] d\eta d\vec{\kappa} \Big\}. \end{aligned} \tag{78}$$

To implement this correction algorithm in an actual adaptive-optics system would require the measured phase to first be decomposed into Fourier components. Each frequency component of the resulting decomposed wavefront would then be multiplied by $\exp(j\eta_o \beta)$ to accomplish the shift and then inverse Fourier transformed. The resulting wavefront would then be used for correction of the object wavefront.

5.3 Numerical results

This section presents an analysis of the new correction algorithm through an evaluation of the phase OTF given in Eq. (78). The evaluation of Eq. (78) uses continuous turbulence profiles rather than the layered profiles as discussed in Chapter II. A discussion of the reasons for using a continuous profile is reserved for the end of this section.

64

Note that the new phase OTF expression of Eq. (78) matches the conventional phase of Eq. (27) on page 17, if we let $\eta_o = 0$. Note also, that if the atmosphere was composed of a single phase screen at altitude η_o, the phase OTF of Eq. (78) would equal 1 (i.e., ideal correction). However, when phase screens are located away from η_o, a less than ideal correction will result (i.e. $H_p < 1$). Therefore, for an initial test, η_o is chosen equal to the center of mass of the turbulence profile. For this test, two continuously distributed turbulence profiles are considered. Model SLC-N represents a fit to the AMOS night data as shown in Figure 5 on page 21 and model HV-54 represent the Hufnagel-Valley turbulence profile calculated with a 54 mph upper atmospheric wind, also shown in Figure 5 on page 21. Model SLC-N has a center of mass equal to 1534.25 meters and model HV-54 has a center of mass equal to 3408.5 meters.

Figures 22 and 23 show the phase OTFs obtained using a shift parameter of $\eta_o \beta$ where η_o is set equal to the center of mass of the respective profiles. The object angles for these plots are the isoplanatic angles defined by Fried (10) where θ_o for model SLC-N is 13μrad and θ_o for model HV-54 is 2.4μrad. Figures 22 and 23 show approximately a 11.5 % increase in the high frequency OTF for model SLC-N and about a 3 % increase for model HV-54. Note also that for model HV-54, a significant trade-off consideration must be made between the improvement in the high frequency response and the attenuation in the low frequency response as shown in Figure 23. The difference in correction improvement attained by the two turbulence profiles is determined to be related to the shape of the turbulence profile. By looking at the turbulence profiles in Figure 5 on page 21, a large amount of far-field turbulence in model HV-54 can be seen. Also, it is noted that relative to the center of mass at an altitude of 3408.5 meters, there is a large amount of turbulence located a significant distance away from the center of mass. The greater amount of far-field turbulence results in a greater attenuation in the amplitude portion of the OTF which is not corrected for by the adaptive-optics correction algorithm. The distribution of turbulence away from the center of mass results in a less effective correction when the correction algorithm corrects to the center of mass (i.e. η_o = center of mass). In contrast, model SLC-N contains less far-field

turbulence and a greater proportion of turbulence located near the center of mass at 1534.25 meters. These two properties of the SLC–N turbulence profile result in an increase in the effectiveness of the correction algorithm when using the center of mass of the C_n^2 profile for the $\eta_o \beta$ shift parameter.

The next step is to determine if the center of mass is the best choice for use as a shifting parameter. In Figures 24 and 25 the $\rho = 1$ meter value of the phase OTF is plotted as a function of η_o . These figures show that a slightly better correction is achieved by shifting downward in altitude from the center of mass.

Figures 22 through 25 give a good qualitative look at the FOV improvement obtained through the new correction algorithm. A more quantitative analysis of the FOV is presented in Figures 26 and 27. The FOV of the adaptive–optics system is defined by the isoplanatic angle. The isoplanatic angle angle is defined by Fried (10) as the angle where the high frequency limit of the phase OTF has been attenuated to a factor of e^{-1} of its value at $\vartheta = 0$. Using this definition of the FOV, the SLC–N turbulence profile has an FOV of 19.9μrad using the conventional correction algorithm. The FOV using the new correction algorithm with a shift corresponding to $\eta_o = 1000$ meters is 24.33μrad or an increase of 22.2% in the FOV. For the HV–54 turbulence profile, the increase in FOV is more modest at 3.6μrad for the conventional correction algorithm and 3.9μrad for the new correction algorithm using $\eta_o = 2000$ meters. Use of the new correction algorithm results in an 8.3% increase in the FOV for model HV–54. The reasons for the difference in the improvement between the two turbulence profiles are the same as discussed above for the high frequency OTF improvement.

During the correction algorithm analysis, tests were made using several combinations of finite numbers of phase screens as well as a continuous turbulence profile. Figure 28 shows the phase OTFs using a shift parameter of $\eta_o \beta$ where η_o is set equal to the center of mass for the atmospheric model SLC–N. The two curves plotted in Figure 28 are a comparison of the OTF calculated using a 4–layered atmospheric model and the OTF calculated using a continuous atmospheric profile. Similarly, Figure 29 plots the $\rho = 1$ meter value of the phase OTF as a function of η_o. For $\eta_o = 0$ (i.e. the conventional correction algorithm),

66
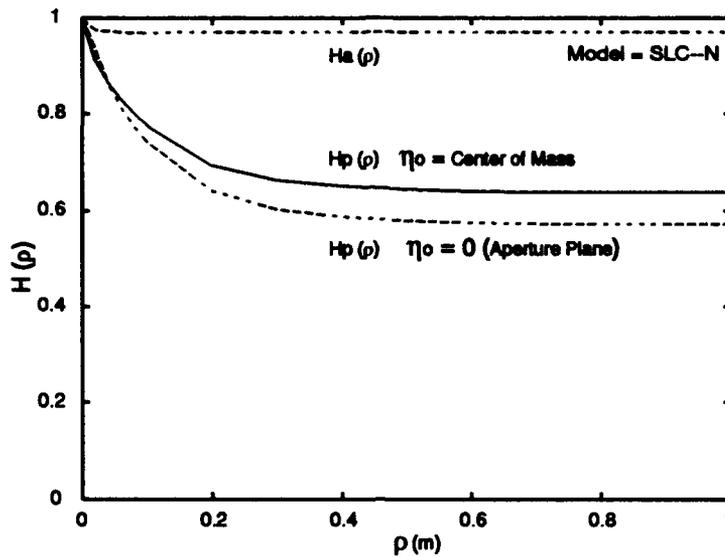
Figure 22. Comparison between the phase OTFs for the new correction algorithm and the conventional correction algorithm. The OTFs are calculated with a $\lambda = 0.5\mu\mathrm{m}$, an AMOS night turbulence profile, $\vartheta = 13.0\mu\mathrm{rad}$, and a Von Karman refractive index power spectrum with $L_m = 1\mathrm{mm}$ and $L_o = 5\mathrm{m}$. The amplitude OTF is not affected with the new correction algorithm but is shown here for reference.

the calculation methods produce a 2% difference in OTF value. However, at the peak of $\eta_o = 1000$meters, the calculation methods produce a 7% difference in OTF value. Results for the conventional algorithm calculations were also verified in Chapter II. The results of this analysis are a reminder that a layered atmospheric model is only an approximation. All real turbulence profiles are continuously distributed with respect to altitude. Many measurements of atmospheric turbulence have been made (3, 29, 37, 41, 50) and are commonly used to justify the use of a layered atmosphere for all applications. The measured turbulence data only indicates that some turbulence profiles may be modeled as discrete layers better than others. In Chapter II and Chapter III, it was determined that a layered atmospheric profile was a good approximation for use in OTF and SNR calculations. However, before these conclusions were reached, the results using a layered profile were compared to a continuous atmospheric profile. It is advised that for any new correction algorithm, theory should be developed to account for the continuous atmospheric profile before simplifications to a layered atmosphere are made.
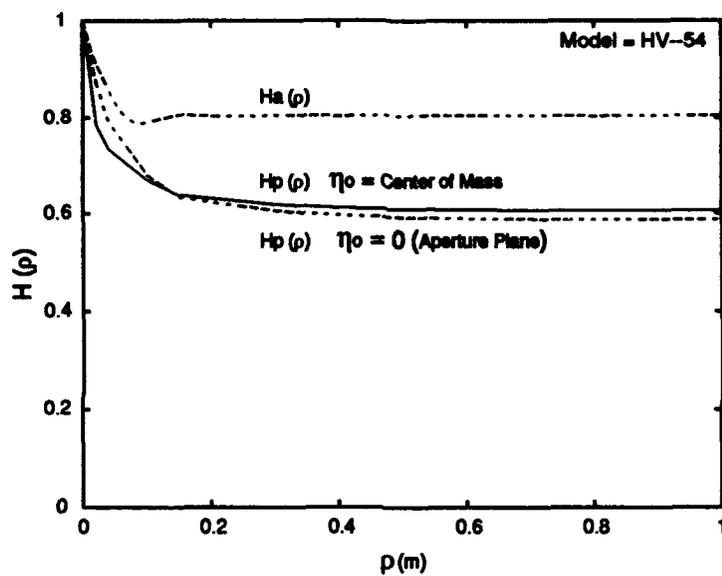
Figure 23. Comparison between the phase OTFs for the new correction algorithm and the conventional correction algorithm. The OTFs are calculated with a $\lambda = 0.5\mu$m, a Hufnagel–Valley turbulence profile with a 54 mph upper altitude wind (21), $\vartheta = 2.4\mu$rad, and a Von Karman refractive index power spectrum with $L_m = 1$mm and $L_o = 5$m. The amplitude OTF is not affected with the new correction algorithm but is shown here for reference.

68
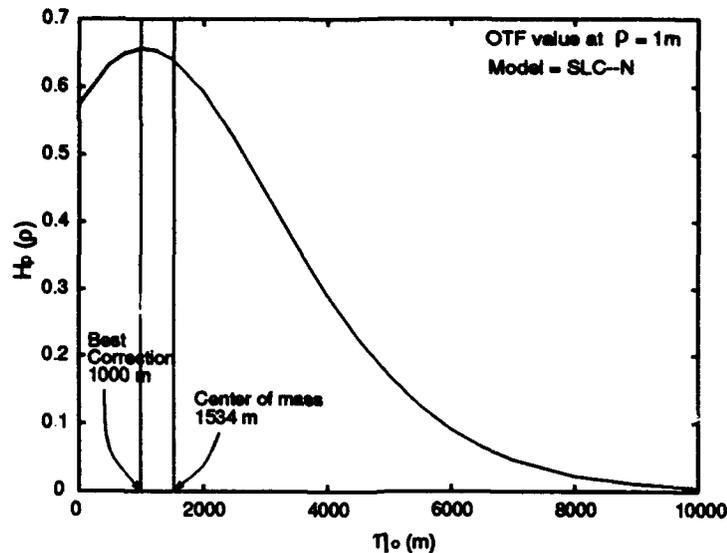
Figure 24.   The phase OTF plotted against shift parameter η_o for model SLC–N. The computed value at each altitude represents the phase OTF at $\rho = 1$m with a $\lambda = 0.5\mu$m, an AMOS night turbulence profile, $\vartheta = 13.0\mu$rad, and a Von Karman refractive index power spectrum with $L_m = 1$mm and $L_o = 5$m.
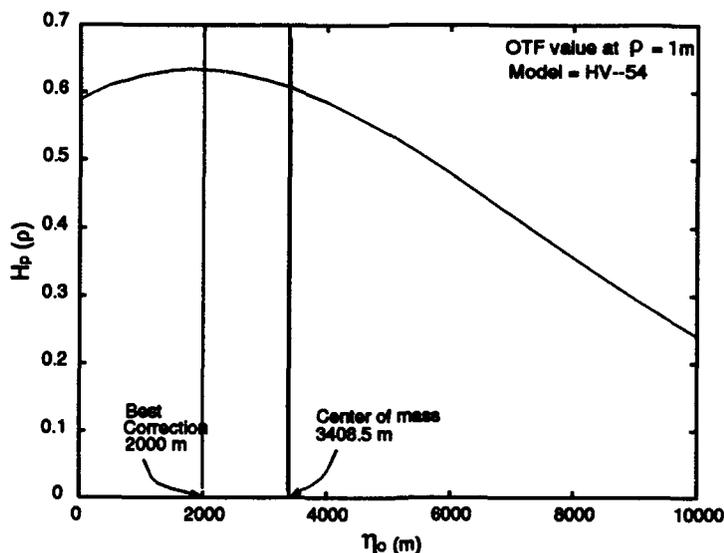
Figure 25.   The phase OTF plotted against shift parameter η_o for model HV-54. The computed value at each altitude represents the phase OTF at $\rho = 1$m with a $\lambda = 0.5\mu$m, a Hufnagel-Valley turbulence profile with a 54 mph upper altitude wind (21), $\vartheta = 2.4\mu$rad, and a Von Karman refractive index power spectrum with $L_m = 1$mm and $L_o = 5$m.

69
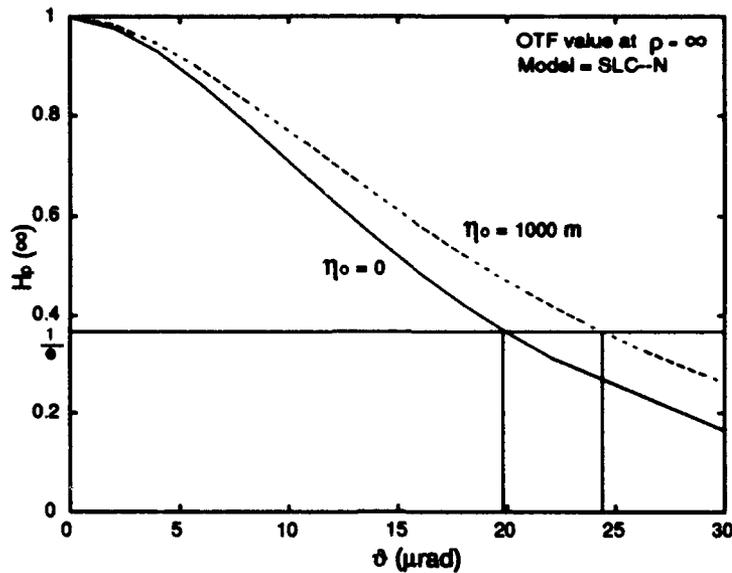
Figure 26. Isoplanatic angle for atmospheric model SLC-N. The computed value at each angular separation represents the OTF at $\rho = \infty$m with a $\lambda = 0.5\mu$m, an AMOS night turbulence profile, $\eta_o = 1000.0$m, and a Von Karman refractive index power spectrum with $L_m = 1$mm and $L_o = 5$m.
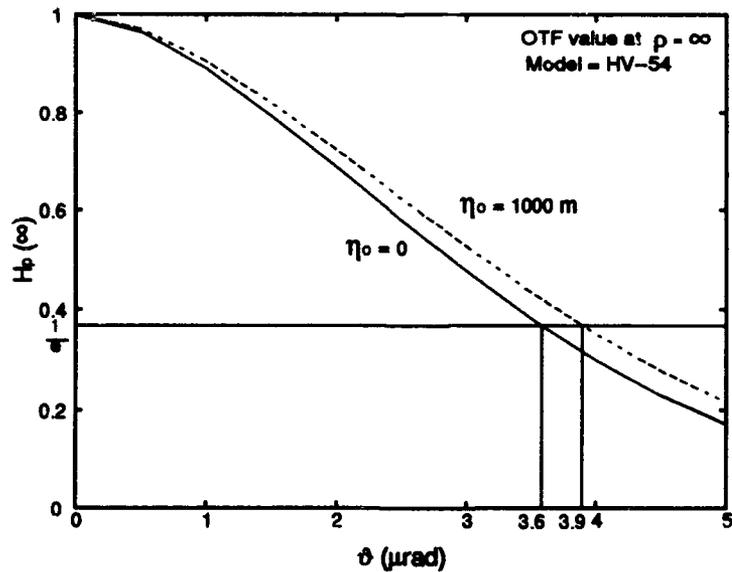
Figure 27. Isoplanatic angle for atmospheric model HV-54. The computed value at each angular separation represents the OTF at $\rho = \infty$m with a $\lambda = 0.5\mu$m, a Hufnagel-Valley turbulence profile with a 54 mph upper altitude wind (21), $\eta_o = 2000.0$m, and a Von Karman refractive index power spectrum with $L_m = 1$mm and $L_o = 5$m.

70
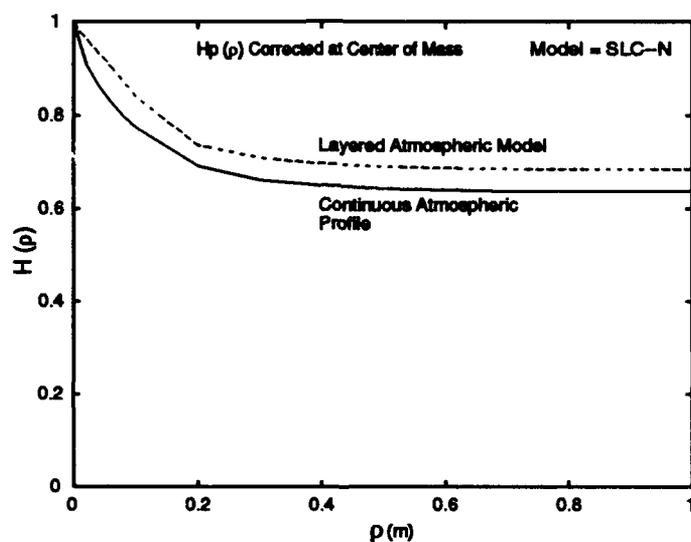
Figure 28.   Comparison with layered atmospheric model for new correction algorithm OTF calculation using atmospheric model SLC-N. The OTFs are calculated with a $\lambda = 0.5\mu$m, an AMOS night turbulence profile, $\vartheta = 13.0\mu$rad, and a Von Karman refractive index power spectrum with $L_m = 1$mm and $L_o = 5$m. The layered atmospheric calculation uses the 4-layered atmospheric model discussed in Chapter II
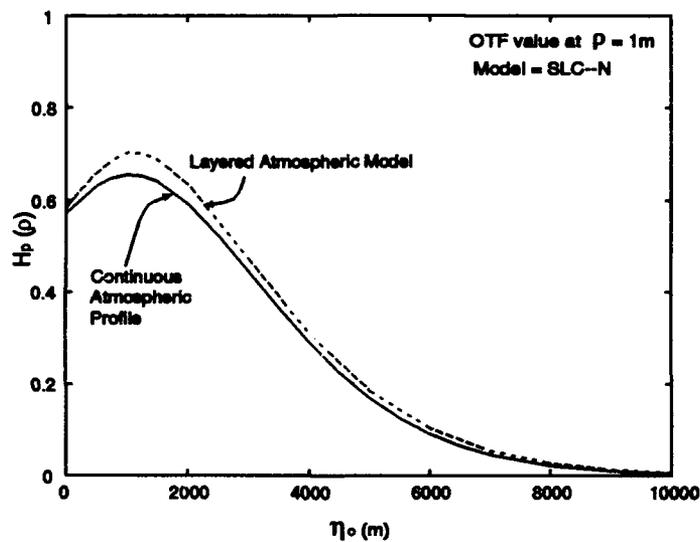
Figure 29. Comparison with layered atmospheric model for new correction algorithm OTF calculation plotted against shift parameter η_o for model SLC-N. The computed value at each altitude represents the phase OTF at $\rho = 1\text{m}$ with a $\lambda = 0.5\mu\text{m}$, an AMOS night turbulence profile, $\vartheta = 13.0\mu\text{rad}$, and a Von Karman refractive index power spectrum with $L_m = 1\text{mm}$ and $L_o = 5\text{m}$. The layered atmospheric calculation uses the 4-layered atmospheric model discussed in Chapter II

5.4 Summary and Conclusions

A new wavefront correction algorithm using the diffraction-based model developed in Chapter II is developed and presented in this chapter. This new correction algorithm makes use of additional information regarding the phase of the propagating wavefronts. The improvement in the correction algorithm is made through a spatial frequency dependent shift parameter, $\eta_o \beta$, where η_o is thought of as an altitude. The best choice of η_o is found to be an altitude slightly lower than the calculated center of mass of the atmospheric C_n^2 turbulence profile. By choosing the optimum value of η_o, the correctable FOV increased by 22.2% for the SCL-N turbulence profile and by 8.3% for the HV-54 profile. The difference in the correctable FOV increase is determined to be due to the distribution of the C_n^2 profiles. A turbulence profile with turbulence distributed closer to a single altitude achieves greater benefit with the new correction algorithm presented in this chapter.

It is also determined through this analysis that care must be taken regarding modeling a continuous atmospheric turbulence profile with discrete layers. A significant difference in the correction results is noted between using a continuous atmospheric turbulence profile and using a layered model 'approximation' of the turbulence profile.

VI. Conclusions and recommendations

6.1 Introduction

This research effort takes a new approach to the analysis of performance measures of an adaptive–optics system. In a typical adaptive–optics system, the object and reference beacon are separated by an object angle. The correction in an adaptive–optics system is accomplished by subtracting the measured phase of the reference beacon from the phase of the object. The non–homogeneous nature of atmospheric turbulence results in performance measures that are a function of the object angle. In this research a diffraction–based propagation model is used to track both the amplitude and phase variations in a propagating wavefront. The diffraction–based model allows for proper accounting of the amplitude and phase contributions to the performance of the adaptive–optics system. Several analysis tools are also developed which allowed a numerical evaluation of the derived performance expressions.

This chapter presents a summary of the contributions of this research along with the significance of the contributions. These contributions are unique and are seen to have a significant impact on the theoretical thinking of the adaptive–optics community. Recommendations for further research are also given.

6.2 Contributions

Propagation Model: A diffraction–based model for plane–wave propagation at an arbitrary angle through atmospheric turbulence is developed in Chapter II. This model is based on the work of Lee and Harp (30) for propagation along the optic axis and extends their results to account for propagation at an arbitrary angle. Results for propagation at an arbitrary angle are required in adaptive–optics analysis since wavefront correction is based on the phase difference between waves propagating at different angles. The diffraction–based propagation model is essential for calculation of the amplitude and phase variations of a propagating wave. The conventional geometric optics propagation model neglects diffraction effects and therefore can not account for the amplitude variations in a propagating wave.

74

Neglecting amplitude variations results in an inaccurate prediction of adaptive-optics system performance.

Amplitude and Phase Optical Transfer Function (OTF) Derivation: An object angle dependent, average amplitude and phase OTF of an adaptive-optics system is developed and presented in Chapter II. The overall OTF is a product of the amplitude and phase OTFs. Computing the amplitude and phase OTFs, requires the previously developed diffraction based propagation model to characterize the amplitude and phase transmittance functions for an adaptive-optics system. The transmittance functions are converted to transfer functions through definitions taken from Goodman (14). The OTF expressions presented in Chapter II represent the first time that angle dependent amplitude *and* phase transfer functions have been developed for an adaptive-optical system. The transfer functions are in the form of a three dimensional integration over the two dimensions of the turbulence spectrum and the single dimension of the propagation path.

Layered Turbulence: A moment matching method of modeling atmospheric turbulence through an arbitrary number of turbulent layers located at pre-determined altitudes is developed and presented in Chapter II. The three dimensional integration for the OTF is computationally intensive and requires recomputation for every new atmospheric turbulence profile. The layered turbulence model presented in this dissertation, uses a set of phase screens located at predetermined altitudes to represent the atmospheric turbulence profile. This atmospheric model using predetermined altitudes is required to develop a method of rapidly calculating the OTF under changing atmospheric conditions. The layered turbulence model using moment matching phase screens at predetermined altitudes as presented in this dissertation is the first time such a model has been developed.

OTF Evaluation: A method of rapidly evaluating the OTF of an adaptive-optics system which allows scaling to different atmospheric conditions is developed and presented in Chapter II. This method requires the development of new theory to represent the OTF by a series of normalized phase transfer functions and amplitude correlation functions for each of the layers of the turbulence model. The normalization is with respect to the strength of turbulence,

75

thus allowing scaling to various turbulence conditions. This method of computation is applied to a typical atmospheric profile to demonstrate the significant contribution of the amplitude OTF to the performance of an adaptive-optics system. It is also shown that the isoplanatic angle is larger than predicted by previous theory using a geometric optics calculation. This indicates that the adaptive-optics system degradation with respect to object angle is less severe than stated by previous geometric optics calculations.

Signal-to-Noise Ratio SNR Derivation: The object angle dependent SNR of an adaptive-optics system OTF is developed and presented in Chapter III. The average OTF developed in Chapter II gives no indication as to how a specific realization of the OTF varies from the average OTF. This information is gained through the OTF SNR. Knowledge of the SNR is also required whenever image reconstruction is used in conjunction with adaptive-optics to determine the spatial frequencies available for the reconstruction process. The SNR derivation in this dissertation represents the first presentation of an angle dependent OTF SNR for an adaptive-optics system. The resulting SNR is in the form of a seven dimensional integration.

SNR Evaluation: A method of rapidly evaluating the SNR of an adaptive-optics system OTF which allows scaling to different atmospheric as well as geometric conditions is developed and presented in Chapter III. The seven dimensional integral result of the SNR derivation, is actually a four dimensional integral over a function of three dimensional phase and amplitude correlations. For the evaluation of the SNR, the layered atmospheric model is used to calculate an array of normalized correlation function values over a wide range of object angles. A least squares fitting routine is then developed to determine approximating functions to approximate the three dimensional integration of the correlation functions. The approximating functions are used to evaluate the SNR for a typical atmospheric turbulence profile. This evaluation demonstrates the utility of the SNR to adaptive-optics image reconstruction by identifying an adaptive-optics cutoff frequency. The SNR evaluation in this dissertation represents the first presentation of an evaluation of the angle dependent OTF SNR for an adaptive-optics system.

Point Spread Function (PSF) and Strehl Ratio Evaluation: The angle dependent average PSF and Strehl ratio of an adaptive-optics system is developed and presented in Chapter IV. The PSF is calculated by first computing an array of OTF values for a particular atmospheric profile. The OTF values are computed using the average OTF expressions and the OTF evaluation method developed in Chapter II. The OTF array is then inverse Fourier transformed using standard FFT techniques. The non-symmetric nature of the PSF is demonstrated with an observed elongation of the PSF in the direction of the object angle. The Strehl ratio is computed as the ratio of the peak of the PSF to the peak of the diffraction limited PSF. This is the first presentation of an angle dependent PSF that accounts for both amplitude and phase effects in an adaptive-optics system.

Correction Algorithm: A new adaptive-optics wavefront correction algorithm which extends the correctable FOV of the adaptive-optics system is developed and presented in Chapter V. Information regarding the wavefront phase differences between the beacon and the object is gained through the propagation model presented in Chapter II. This additional information is used to develop the new correction algorithm. An analysis is performed using two different atmospheric profiles to demonstrate the utility of this new correction algorithm. It is shown that for an atmospheric profile containing only a small amount of high altitude turbulence (the SLC-N model of Figure 5, page 21), an increase of over 20% in the FOV is achieved. When the turbulence profile is more distributed (the HV-57 model of Figure 5, page 21), an increase of approximately 8% in the FOV is achieved.

6.3 Recommendations for future research

The first recommendation is for a more extensive analysis using the average OTF developed in Chapter II. The analysis should determine how atmospheric profiles affect the level of the amplitude and phase OTF. An attempt should be made to quantify when a geometric optics calculation method is adequate and when the diffraction-based calculation method becomes necessary. This same analysis should be performed on the SNR calculations. More research is necessary to determine some simplifications that could be used for the SNR,

and under what atmospheric conditions the simplifications would apply. For example, it should be determined what atmospheric conditions allow the amplitude correlations to be neglected. It is suspected that simplifications to the SNR such as neglecting the amplitude correlations would be valid over a wider range of atmospheric conditions than for the average OTF.

The atmospheric profiles such as the ones shown in Figure 5, page 21, are averaged profiles may not be a good representation of actual profiles. These profiles, are standard throughout the community, but are created using measured data processed through a smoothing function. Measured profiles may vary significantly from the averaged profile. From the analysis of Chapter II, it is known that the transformation from turbulence strength to OTF value is a non–linear operation. Therefor, standard smoothing techniques for the turbulence profile may be a poor method of obtaining a good representation of the turbulence for the purpose of adaptive–optics performance analysis. Two suggested solutions to this problem are proposed. First, determine a better smoothing operation on the turbulence profile data. This would require determining the nonlinear transformation relation between the turbulence profile and the performance measures. This relationship could then be used to develop a properly weighted smoothing function for the turbulence data. A second suggestion is to simply treat the turbulence profile as a random process with a given mean and standard deviation. The adaptive–optics performance measures could then be evaluated at the mean value of the turbulence profile as well as at plus and minus one or two standard deviations. This may yield a clearer picture of the expected adaptive–optics performance.

The new correction algorithm presented in Chapter V appears to have significant promise in extending the correctable FOV. More work could be done with the correction algorithm in its present form to determine what atmospheric conditions yield the best increase in the correctable FOV. It is suspected that results of this analysis would indicate that as a profile becomes more concentrated in a single layer, performance is increased. Also, as turbulence shifts toward lower altitudes, an increase in performance should be seen. Finally, the correction algorithm indicates that perfect correction could be obtained if a received signal could be decomposed into specific altitude contributions. More research needs to be done in this area. Some help in

this solution may be obtained through Johnston's (22) work with multi-conjugate adaptive-optics. It is also possible that different frequencies have a different optimum correction altitude. Currently, the correction algorithm of Chapter V adds a shift to each frequency component that is based on a single altitude. Further research in this area could result in additional improvement in the correctable FOV.

Appendix A. Atmospheric model

In this appendix, a model of atmospheric turbulence is presented. The important concepts include the idea of pockets or 'eddies' of turbulence, the dimensions of these eddies, and how these dimensions are incorporated into a refractive index power spectrum.

The atmospheric model begins by considering the power spectrum of the refractive index variations. The refractive index variations is the cause of atmospheric turbulence. It is common to think of the refractive index variations as pockets of air or 'eddies', each with a characteristic refractive index as shown in Figure 30. The power spectrum of the refractive index turbulence, given by $\Phi(\kappa_x, \kappa_y, \kappa_z)$, may be regarded as a measure of the relative abundance of eddies with dimensions $L_x = 2\pi/\kappa_x$, $L_y = 2\pi/\kappa_y$, and $L_z = 2\pi/\kappa_z$ where L is the length of an eddy and κ is the wavenumber. The atmospheric model presented in this appendix and used throughout this dissertation is one with locally isotropic turbulence. This means that at any point, the distribution of eddy dimensions is the same in all three directions. Isotropic turbulence results in a power spectrum given by $\Phi(\kappa)$ which is a function of a single wavenumber κ with a corresponding eddy size of $L = 2\pi/\kappa$.

The refractive index power spectrum can be thought of as divided into three significant regions. The boundaries of these regions are defined by the inner and outer scale size of the turbulence. The scale size $L_o = 2\pi/\kappa_o$ is called the outer scale of the turbulence and the scale size of $L_m = 2\pi/\kappa_m$ is called the inner scale of the turbulence. The region between the outer scale size and the inner scale size is called the inertial subrange.

The power spectrum of the inertial subrange is determined simply by the physical laws that govern the breakup of large eddies into smaller ones (i.e., the science of turbulent flow). The power spectrum of eddies larger than the outer scale size, L_o, will be affected by things like large scale geographic and meteorological conditions. Turbulent eddies smaller than the inner scale size, L_m, dissipate energy as a result of viscous forces with the result being that the power spectrum beyond this point falls off very rapidly. The sizes of eddies of most concern in adaptive optics are those in the inertial subrange which are modeled, through the work of

80
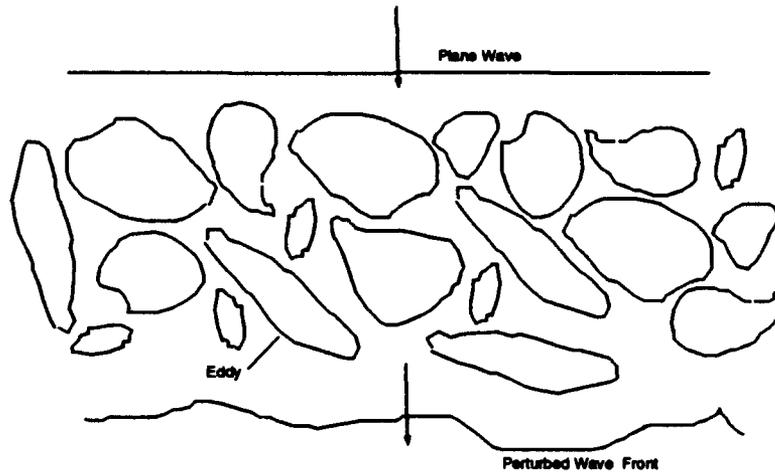
Figure 30. A representation of pockets or eddies of turbulence in the atmosphere. Each pocket can be thought of being composed of a single refractive index. The variations in the refractive index result in perturbations in a propagating wavefront.

Kolmogorov (27), with a power spectrum defined by

$$\Phi(\kappa, \eta) = 0.033 C_n^2(\eta)\kappa^{-11/3},\qquad(79)$$

where η is the altitude and $C_n^2(\eta)$ is called the structure constant of the refractive index fluctuations and is a measure of the strength of the fluctuations. The value of the structure constant depends on local atmospheric conditions and height above the ground. Typical values near the ground vary from $10^{-13}\mathrm{m}^{-2/3}$ for strong turbulence to $10^{-17}\mathrm{m}^{-2/3}$ for weak turbulence with $10^{-15}\mathrm{m}^{-2/3}$ as an average value. This power spectrum has appropriately been called the Kolmogorov power spectrum. The Kolmogorov spectrum is very useful, but care must be taken outside of the inertial subrange. In particular, note the pole in the spectrum at $\kappa = 0$.

In the analysis presented in this dissertation, it is necessary to integrate the power spectrum over all values of κ. To avoid the singularity at zero a modification of the Kolmogorov

81

spectrum called the Von Karman spectrum is used. This spectrum is given by

$$\Phi(\eta, \kappa) = \frac{0.033 C_n^2(\eta)}{\left(\kappa^2 + \kappa_o^2\right)^{11/6}} e^{\left(\frac{-\kappa^2}{\kappa_m^2}\right)}, \tag{80}$$

where κ_o and κ_m are the outer and inner scale wavenumbers, respectively. Not only is the Von Karman spectrum of a nicer form for numerical integration, it is also more representative of actual turbulence. Any refractive index power spectrum should level off as $\kappa \Rightarrow 0$ since there can only be a finite amount of air in the earths atmosphere. A normalized spectrum of $\frac{\Phi(\eta,\kappa)}{C_n^2(\eta)}$ with $\kappa_o = \frac{2\pi}{5\,\mathrm{m}}$ and $\kappa_m = \frac{2\pi}{1\,\mathrm{mm}}$ is plotted in Figure 31. These scale parameters are used throughout the body of this work with more details of how the scale parameters effect system performance given in Section 2.5. Note that the Von Karman spectrum with an outer scale wavenumber of 0, and an inner scale wavenumber set at infinity, is equivalent to the Kolmogorov power spectrum.
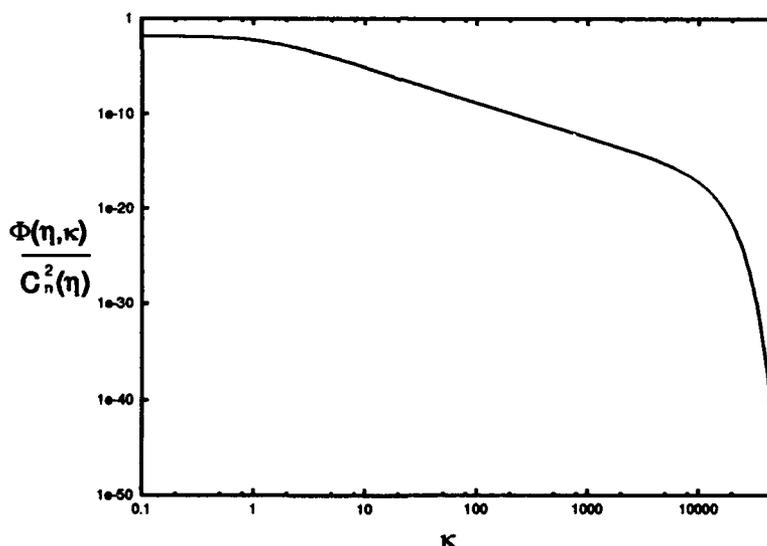
Figure 31. The normalized Von Karman refractive index power spectrum, $\frac{\Phi(\eta,\kappa)}{C_n^2(\eta)}$, as plotted against wavenumber κ. This spectrum is plotted for an outer scale size of 5 meters and an inner scale size equal to 1 millimeter.

82

Appendix B. Phase screen model

This appendix presents the concept of an atmospheric phase screen necessary to understand the model of atmospheric propagation. The goal is to model a section of the atmosphere as a thin phase screen such that a wavefront propagating through the phase screen is identical to a wavefront passing through an actual section of atmosphere. Lee and Harp (30) used the method of phase screens to calculate the phase and amplitude perturbations of a plane wave and their results were validated with the wave equation method by Clifford and Strohbehn (4).

As a wave propagates through a section of the atmosphere, it experiences phase delays related to the index of refraction of that particular section. Since the atmosphere is non-homogeneous with respect to the index of refraction, different portions of the wave will experience different phase delays. A section of atmosphere can therefore be modeled as a phase-only transmittance function or phase screen. Let the transmittance of the phase screen be represented by

$$t(\eta, \vec{x}) = e^{-j\Delta\phi(\eta,\vec{x})}, \tag{81}$$

where, η is the altitude of the phase screen and $\Delta\phi(\eta, \vec{x})$ is the phase of the screen at a location given by $\vec{x}$. As a wave passes through this screen, a phase equal to $\Delta\phi(\eta, \vec{x})$ will be added to the wavefront. In order to properly model the phase screen, $\Delta\phi(\eta, \vec{x})$ must represent the actual phase changes experienced in propagation through a section of turbulence. Let an individual spatial frequency component, $\vec{\kappa}$, of $\Delta\phi(\eta, \vec{x})$ be given by

$$\Delta\phi(\eta, \vec{x}, \vec{\kappa}) = k \, dh \, a(\eta, \vec{\kappa}) \cos(\vec{\kappa} \cdot \vec{x} + \phi_o(\eta, \vec{\kappa})), \tag{82}$$

where k defines the wavenumber of the propagating wave, dh is a differential thickness of the phase screen, $a(\eta, \vec{\kappa})$ and $\phi_o(\eta, \vec{\kappa})$ are the amplitude and initial phase offset of the spatial Fourier component of the index of refraction variations having a spatial frequency $\vec{\kappa}$. Within a plane, the index-of-refraction fluctuations are isotropic but with a power spectrum that is, in general, dependent on the altitude of the screen.

83

Let $\Psi(\eta, \vec{\kappa})$ be the complex amplitude of the Fourier transform component of the refractive index variations, $a(\eta, \vec{\kappa}) \cos(\vec{\kappa} \cdot \vec{x} + \phi_o(\eta, \vec{\kappa}))$, where $\Psi(\eta, \vec{\kappa}) = a(\eta, \vec{\kappa}) \frac{1}{2} e^{j(\phi_o(\eta, \vec{\kappa}))}$. A relationship between the complex Fourier components, $\Psi(\eta, \vec{\kappa})$, and the refractive index power spectrum is given by Tatarski (46) as

$$\langle \Psi(\eta_1, \vec{\kappa}_1)\Psi^*(\eta_2, \vec{\kappa}_2) \rangle = \delta(\vec{\kappa}_1 - \vec{\kappa}_2)F(\eta_1 - \eta_2, \vec{\kappa}_1)d\kappa_1 d\kappa_2, \tag{83}$$

where $F(\eta_1 - \eta_2, \vec{\kappa}_1)$ represents the two dimensional refractive index power spectrum and δ is the Dirac delta function. Notice that Eq. (83) indicates that different frequencies within a phase screen are independent of each other. This fact is essential in the calculations presented in the body of this dissertation. It is now convenient to represent the phase screen of Eq. (82) as

$$\Delta\phi(\eta, \vec{x}, \vec{\kappa}) = A(\eta, \vec{\kappa}) \cos(\vec{\kappa} \cdot \vec{x} + \phi_o(\eta, \vec{\kappa})), \tag{84}$$

where, $A(\eta, \vec{\kappa}) = k \, d^h \, a(\eta, \vec{\kappa})$. The complex phasor representation of the phase screen is then given by

$$
\begin{aligned}
\underline{\Delta\phi}(\eta, \vec{x}, \vec{\kappa}) &= A(\eta, \vec{\kappa}) e^{\phi_o(\eta, \vec{\kappa})} e^{\vec{\kappa} \cdot \vec{x}} \\
&= \tilde{A}(\eta, \vec{\kappa}) e^{\vec{\kappa} \cdot \vec{x}}.
\end{aligned}
\tag{85}
$$

The relation between the phase screen variations and the refractive index power spectrum is then given by

$$
\begin{aligned}
\langle \tilde{A}(\eta_1, \vec{\kappa}_1)\tilde{A}^*(\eta_2, \vec{\kappa}_2) \rangle &= \langle 2k \, dh_1 \, \Psi(\eta_1, \vec{\kappa}_1) 2k \, dh_2 \, \Psi^*(\eta_2 \vec{\kappa}_2) \rangle \\
&\quad 4k^2 \delta(\vec{\kappa}_1 - \vec{\kappa}_2)F(\eta_1 - \eta_2, \vec{\kappa}_1)d\kappa_1 d\kappa_2.
\end{aligned}
\tag{86}
$$

This relation will be used for the derivation of the residual amplitude and phase correlation functions derived in Appendix D.

Appendix C. Derivation of amplitude and phase perturbation equations

In this appendix, the amplitude and phase perturbation equations are derived for a wavefront that has propagated through the atmosphere at some arbitrary angle as shown in Figure 32. In the body of this dissertation, the object angle, ϑ, is defined as the angle between the beacon and the object. To maintain consistency, the optic axis is defined here as the axis from the optics to the beacon and the turbulent layer and observation plane are perpendicular to the propagation direction from the beacon. Any propagating wave can be considered to be propagating in a direction determined by the propagating wavenumber $\vec{k}$, defined by the individual k_x and k_y components of $\vec{k}$. In our system, the turbulent layers are in the x,y plane, and the optic axis defines the z axis. For initial ease of calculations, the 'off axis' wave from the object is designated as a wave having an arbitrary k_x wavenumber component. This arbitrary k_x wavenumber component will result in a propagation angle with respect to the optic axis. The analysis is not restricted by only allowing a k_x wavenumber component since the direction of propagation in the x, y plane will *define* the x axis of the system. The first step in the analysis is to determine the measured wavefront obtained from a point source as propagated through a single frequency component of a phase screen placed at an arbitrary distance away from the aperture plane of the system. A discussion of a phase screen is given in Appendix B. The phase screen will be a single frequency sinusoidal grating with an arbitrary orientation in the x, y plane, with frequency and orientation defined by $\vec{\kappa}$, located at an altitude η, and written as

$$\Delta\phi(\eta, \vec{x}, \vec{\kappa}) = A(\eta, \vec{\kappa})\cos(\vec{\kappa}\cdot\vec{x} + \phi_o(\eta, \vec{\kappa})), \qquad (87)$$

where $A(\eta, \vec{\kappa})$ and $\phi_o(\eta, \vec{\kappa})$ are defined as in Appendix B. In the following analysis we assume that $A(\eta, \vec{\kappa}) \ll 1$ which is consistent with the weak turbulence assumption. It is convenient to represent this phase screen in exponential form as

$$\Delta\phi(\eta, \vec{x}, \vec{\kappa}) = \frac{A(\eta, \vec{\kappa})}{2}\left(e^{j(\vec{\kappa}\cdot\vec{x} + \phi_o(\eta, \vec{\kappa}))} + e^{-j(\vec{\kappa}\cdot\vec{x} + \phi_o(\eta, \vec{\kappa}))}\right). \qquad (88)$$
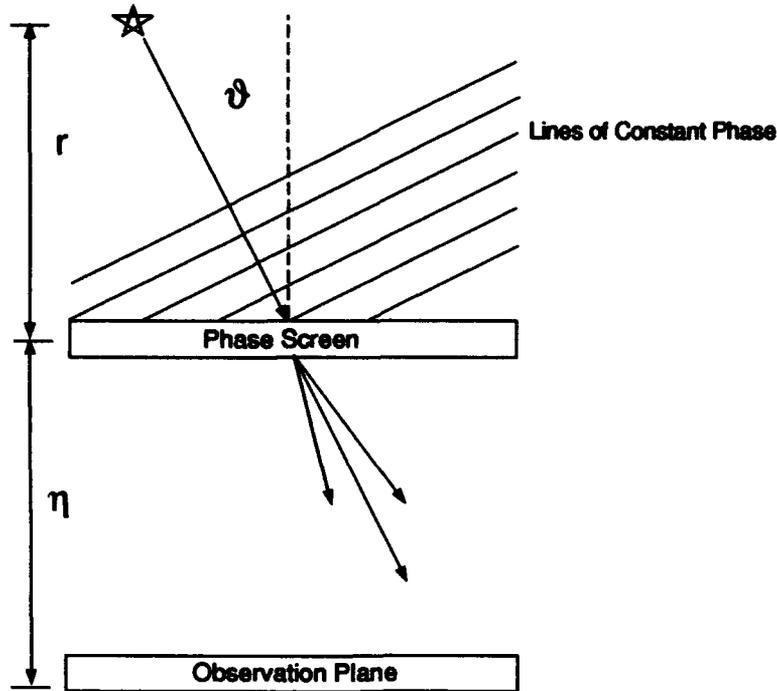
Figure 32. Scattering of a wave through a phase screen

The incoming wave is written with an x frequency component as

$$U_{ref}(r, \vec{x}) = e^{-j(k_z r + k_x x)}, \tag{89}$$

where k_z and k_x are related to the propagation wavenumber k by $k = \sqrt{k_z^2 + k_x^2}$, and r is the distance from the object to the phase screen as shown in Figure 32. The dependence on r will eventually be discarded. However, plane–wave propagation is assumed. Therefore, r must be sufficiently far away to yield a good plane–wave approximation.

After the wave passes through the phase screen, the transmitted field is given by

$$U_t(r, \vec{x}, \vec{\kappa}) = e^{-j(k_z r + k_x x)} e^{-j\Delta\phi(\eta, \vec{x}, \vec{\kappa})}. \tag{90}$$

Expanding the $e^{-j\Delta\phi(\eta,\vec{x},\vec{\kappa})}$ term using a Taylor series, yields

$$e^{-j\Delta\phi(\eta,\vec{x},\vec{\kappa})} = 1 - j\Delta\phi(\eta,\vec{x},\vec{\kappa}) + \frac{(j\Delta\phi(\eta,\vec{x},\vec{\kappa}))^2}{2!} - \frac{(j\Delta\phi(\eta,\vec{x},\vec{\kappa}))^3}{3!} + \cdots \quad (91)$$

Assuming that $\Delta\phi(\eta,\vec{x},\vec{\kappa}) \ll 2\pi$, as implied by $A(\eta,\vec{\kappa}) \ll 1$ the higher order terms in Eq. (91) can be dropped. Rewriting Eq. (90) gives

$$\begin{aligned} U_t(\vec{x},r,\vec{\kappa}) &= e^{-j(k_z r + k_x x)}(1 - j\Delta\phi(\eta,\vec{x},\vec{\kappa})) \\ &= e^{-j(k_z r + k_x x)}[1 - jA(\eta,\vec{\kappa})\cos(\vec{\kappa}\cdot\vec{x} + \phi_o(\eta,\vec{\kappa}))] \\ &= e^{-j(k_z r + k_x x)}[1 - j\frac{A(\eta,\vec{\kappa})}{2}(e^{j(\vec{\kappa}\cdot\vec{x} + \phi_o(\eta,\vec{\kappa}))} + e^{-j(\vec{\kappa}\cdot\vec{x} + \phi_o(\eta,\vec{\kappa}))})]. \end{aligned} \quad (92)$$

This equation states that the effect of passing the field U_{ref} through the phase screen is that there are now three plane waves – one traveling in the original direction, and two scattered waves traveling at directions determined by the $\vec{\kappa}$ frequency component of the phase screen. In order to propagate U_t to the observation plane, at a distance $r + \eta$ from the object, it is necessary to determine the z components of the wave numbers of the scattered waves. These two components are given by

$$k_z' = \sqrt{k^2 - (k_x + \kappa\cos\theta)^2 - (\kappa\sin\theta)^2}, \quad (93)$$

and,

$$k_z'' = \sqrt{k^2 - (k_x - \kappa\cos\theta)^2 - (\kappa\sin\theta)^2}, \quad (94)$$

where θ is the angle that $\vec{\kappa}$ makes with the x axis. U_t is now propagated to the observation plane, resulting in

$$
\begin{aligned}
U_t(r+\eta,\vec{x},\vec{\kappa}) &= e^{-j(k_z(r+\eta)+k_x x)} - j\frac{A(\eta,\vec{\kappa})}{2}(e^{-j((k_z r+k_x x)+k_z'\eta-(\vec{\kappa}\cdot\vec{x}+\phi_o(\eta,\vec{\kappa})))}) \\
&\quad -j\frac{A(\eta,\vec{\kappa})}{2}(e^{-j((k_z r+k_x x)+k_z''\eta+(\vec{\kappa}\cdot\vec{x}+\phi_o(\eta,\vec{\kappa})))}) \\
&= e^{-jk_z r}[e^{-j(k_z\eta+k_x x)} - j\frac{A(\eta,\vec{\kappa})}{2}(e^{-j(k_x x+k_z'\eta-(\vec{\kappa}\cdot\vec{x}+\phi_o(\eta,\vec{\kappa})))}) \\
&\quad -j\frac{A(\eta,\vec{\kappa})}{2}(e^{-j(k_x x+k_z''\eta+(\vec{\kappa}\cdot\vec{x}+\phi_o(\eta,\vec{\kappa})))})].
\end{aligned}
\tag{95}
$$

Since the *variations* in the phase and amplitude are of interest, the constant phase term $e^{-jk_z r}$ is dropped resulting in

$$
\begin{aligned}
U_t(\eta,\vec{x},\vec{\kappa}) &= e^{-j(k_z\eta+k_x x)} - j\frac{A(\eta,\vec{\kappa})}{2}\left(e^{-j(k_x x+k_z'\eta-(\vec{\kappa}\cdot\vec{x}+\phi_o(\eta,\vec{\kappa})))}\right) \\
&\quad -j\frac{A(\eta,\vec{\kappa})}{2}\left(e^{-j(k_x x+k_z''\eta+(\vec{\kappa}\cdot\vec{x}+\phi_o(\eta,\vec{\kappa})))}\right) \\
&= e^{-jk_x}\left[e^{-jk_z\eta} - j\frac{A(\eta,\vec{\kappa})}{2}\left(e^{-j(k_z'\eta-(\vec{\kappa}\cdot\vec{x}+\phi_o(\vec{\kappa})))}\right)\right. \\
&\quad \left. -j\frac{A(\eta,\vec{\kappa})}{2}\left(e^{-j(k_z''\eta+(\vec{\kappa}\cdot\vec{x}+\phi_o(\eta,\vec{\kappa})))}\right)\right].
\end{aligned}
\tag{96}
$$

Making substitutions to ease the algebraic manipulation, let

$$
\begin{aligned}
a &= k_z'\eta, \\
b &= \vec{\kappa}\cdot\vec{x} + \phi_o(\eta,\vec{\kappa}), \\
c &= k_z''\eta.
\end{aligned}
\tag{97}
$$

Equation 97 is substituted into Eq. (96) to yield

$$
\begin{aligned}
U_t(\eta, \vec{x}, \vec{\kappa}) &= e^{-jk_x x}\left(e^{-jk_z \eta} - j\frac{A(\eta, \vec{\kappa})}{2}\left(e^{-j(a-b)} - e^{-j(c+b)}\right)\right) \\[2mm]
&= e^{-jk_x x}\left(e^{-jk_z \eta} - j\frac{A(\eta, \vec{\kappa})}{2}e^{j(\frac{a+c}{2})}e^{-j(\frac{a+c}{2})}\left(e^{-j(a-b)} + e^{-j(c+b)}\right)\right) \\[2mm]
&= e^{-jk_x x}\left(e^{-jk_z \eta} - j\frac{A(\eta, \vec{\kappa})}{2}e^{-j(\frac{a+c}{2})}\left(e^{-j(a-b-(\frac{a+c}{2}))} + e^{j((\frac{a+c}{2})-c-b)}\right)\right) \\[2mm]
&= e^{-jk_x x}\left(e^{-jk_z \eta} - j\frac{A(\eta, \vec{\kappa})}{2}e^{-j(\frac{a+c}{2})}\left(e^{-j((\frac{a-c}{2})-b)} + e^{j((\frac{a-c}{2})-b)}\right)\right) \\[2mm]
&= e^{-jk_x x}\left(e^{-jk_z \eta} - jA(\eta, \vec{\kappa})e^{-j(\frac{a+c}{2})}\cos\left(\left(\frac{a-c}{2}\right)-b\right)\right). \quad (98)
\end{aligned}
$$

Substituting the expressions for a, b, and c from Eq. (97) back into Eq. (98) gives

$$
\begin{aligned}
U_t(\eta, \vec{x}, \vec{\kappa}) &= e^{-jk_x x}\left(e^{-jk_z \eta} - jA(\eta, \vec{\kappa})e^{-j\eta(\frac{k_z'+k_z''}{2})}\right. \\[2mm]
&\qquad \left.\times \cos\left(\eta\left(\frac{k_z'-k_z''}{2}\right) - (\vec{\kappa}\cdot\vec{x} + \phi_o(\eta, \vec{\kappa}))\right)\right) \\[2mm]
&= e^{-j(k_x x + k_z \eta)}\left(1 - jA(\eta, \vec{\kappa})e^{-j\eta(\frac{k_z'+k_z''}{2}-k_z)}\right. \\[2mm]
&\qquad \left.\times \cos\left(\eta\left(\frac{k_z'-k_z''}{2}\right) - (\vec{\kappa}\cdot\vec{x} + \phi_o(\eta, \vec{\kappa}))\right)\right) \quad (99)
\end{aligned}
$$

Again, drop the constant phase term $e^{-jk_z \eta}$. The term $e^{-jk_x x}$ represents a linear phase term or the unaberrated wavefront phase. This linear phase term will result in an overall tilt to the wavefront. The final expression for the wavefront is written as

$$
U_t(\eta, \vec{x}, \vec{\kappa}) = 1 - jA(\eta, \vec{\kappa})e^{-j\eta(\frac{k_z'+k_z''}{2}-k_z)}\cos\left(\eta\left(\frac{k_z'-k_z''}{2}\right) - (\vec{\kappa}\cdot\vec{x} + \phi_o(\eta, \vec{\kappa}))\right).
$$
$$(100)$$

Before the equations become too lengthy, the variables α and β are introduced, where

$$
\alpha = \left(\left(\frac{k_z'+k_z''}{2}\right) - k_z\right) \quad (101)
$$

and,

$$\beta = \left(\frac{k_z' - k_z''}{2} \right).$$ (102)

To find the amplitude and phase perturbations, U_t is written in terms of real and imaginary parts.

$$
\begin{aligned}
U_t(\eta, \vec{x}, \vec{\kappa}) &= 1 - jA(\eta, \vec{\kappa})e^{-j\eta\alpha}\cos(\eta\beta - (\vec{\kappa} \cdot \vec{x} + \phi_o(\eta, \vec{\kappa}))) \\
&= 1 - jA(\eta, \vec{\kappa})[\cos(\eta\alpha) - j\sin(\eta\alpha)]\cos(\eta\beta - (\vec{\kappa} \cdot \vec{x} + \phi_o(\eta, \vec{\kappa}))) \\
&= [1 - A(\eta, \vec{\kappa})\sin(\eta\alpha)\cos(\eta\beta - (\vec{\kappa} \cdot \vec{x} + \phi_o(\eta, \vec{\kappa})))] - \\
&\quad j[A(\eta, \vec{\kappa})\cos(\eta\alpha)\cos(\eta\beta - (\vec{\kappa} \cdot \vec{x} + \phi_o(\eta, \vec{\kappa})))].
\end{aligned}
$$ (103)

The amplitude perturbations, P_a, can now easily be calculated as the magnitude of U_t minus one ($|U_t| - 1$). The magnitude minus one is considered, because propagation began with a uniform amplitude wave and any perturbations of this unity amplitude is the quantity of interest. The amplitude perturbation equation is written as:

$$
\begin{aligned}
P_a &= |U_t| - 1 \\
&= [\Re^2(U_t) + \Im^2(U_t)]^{\frac{1}{2}} - 1 \\
&= \{[1 - A(\eta, \vec{\kappa})\sin(\eta\alpha)\cos(\eta\beta - (\vec{\kappa} \cdot \vec{x} + \phi_o(\eta, \vec{\kappa})))]^2 \\
&\quad + [-A(\eta, \vec{\kappa})\cos(\eta\alpha)\cos(\eta\beta - (\vec{\kappa} \cdot \vec{x} + \phi_o(\eta, \vec{\kappa})))]^2\}^{\frac{1}{2}} - 1.
\end{aligned}
$$ (104)

Since the assumption is made that the maximum amplitude of the phase screen is much less than unity (i.e., $A(\eta, \vec{\kappa}) \ll 1$), the higher order term of $[-A(\eta, \vec{\kappa})\cos(\eta\alpha\cos(\eta\beta - (\vec{\kappa} \cdot \vec{x} + \phi_o(\eta, \vec{\kappa})))]^2$ is neglected. Therefore,

$$P_a = \{[1 - A(\eta, \vec{\kappa})\sin(\eta\alpha)\cos(\eta\beta - (\vec{\kappa} \cdot \vec{x} + \phi_o(\eta, \vec{\kappa})))]^2\}^{\frac{1}{2}} - 1.$$ (105)

By expanding the square term, dropping the higher order term, and using the binomial expansion on the remaining square root, the following final expression for the amplitude perturbation

90

is obtained:

$$P_a = -A(\eta, \vec{\kappa}) \sin(\eta\alpha) \cos(\eta\beta - (\vec{\kappa} \cdot \vec{x} + \phi_o(\eta, \vec{\kappa}))). \tag{106}$$

Now, in calculating the phase perturbations, recall that the initial plane wave is defined by a uniform phase across the wavefront. All constant phase terms have been dropped in the final wavefront expression of Eq. (100). Therefore, *any* remaining phase is considered to be a phase perturbation. The phase perturbations, P_p, can be represented as

$$
\begin{aligned}
P_p &= \tan^{-1}\left[\frac{\Im(U_t)}{\Re(U_t)}\right] \\
&= \tan^{-1}\left[\frac{-A(\eta, \vec{\kappa}) \cos(\eta\alpha) \cos(\eta\beta - (\vec{\kappa} \cdot \vec{x} + \phi_o(\eta, \vec{\kappa})))}{1 - A(\eta, \vec{\kappa}) \sin(\eta\alpha) \cos(\eta\beta - (\vec{\kappa} \cdot \vec{x} + \phi_o(\eta, \vec{\kappa})))}\right].
\end{aligned}
\tag{107}
$$

A Taylor series expansion of $\tan^{-1}(x)$ for the case when $x^2 < 1$ is used, where

$$\tan^{-1}(x) = x - \frac{x^3}{3} + \frac{x^5}{5} - \cdots \tag{108}$$

Again, neglecting the higher order terms, the final form of the phase perturbations is written as

$$
\begin{aligned}
P_p &= \frac{-A(\eta, \vec{\kappa}) \cos(\eta\alpha) \cos(\eta\beta - (\vec{\kappa} \cdot \vec{x} + \phi_o(\eta, \vec{\kappa})))}{1 - A(\eta, \vec{\kappa}) \sin(\eta\alpha) \cos(\eta\beta - (\vec{\kappa} \cdot \vec{x} + \phi_o(\eta, \vec{\kappa})))} \\[2mm]
&\approx -A(\eta, \vec{\kappa}) \cos(\eta\alpha) \cos(\eta\beta - (\vec{\kappa} \cdot \vec{x} + \phi_o(\eta, \vec{\kappa}))).
\end{aligned}
\tag{109}
$$

This final approximation is made using $A(\eta, \vec{\kappa}) \ll 1$.

Equations (106) and (109) form the final results of this appendix. The remainder of this appendix determines simplified expressions for α and β which are used in the numerical analysis. The simplification of α begins by substituting Eqs. (93) and (94) into Eq. (101) and using a binomial expansion on the square root functions.

$$\alpha = \left(\left(\frac{k'_z + k''_z}{2}\right) - k_z\right)$$

$$= \frac{1}{2}\sqrt{k^2 - (k_x + \kappa\cos\theta)^2 - (\kappa\sin\theta)^2}$$

$$\quad + \frac{1}{2}\sqrt{k^2 - (k_x - \kappa\cos\theta)^2 - (\kappa\sin\theta)^2} - \sqrt{k^2 - k_x^2}$$

$$= \frac{1}{2}\sqrt{k^2 - k_x^2 - \kappa^2 - 2k_x\kappa\cos\theta}$$

$$\quad + \frac{1}{2}\sqrt{k^2 - k_x^2 - \kappa^2 + 2k_x\kappa\cos\theta} - \sqrt{k^2 - k_x^2}$$

$$= \frac{1}{2}\sqrt{k^2 - k_x^2}\left(\sqrt{1 - \frac{\kappa^2 + 2k_x\kappa\cos\theta}{k^2 - k_x^2}}\right.$$

$$\quad \left. + \sqrt{1 - \frac{\kappa^2 - 2k_x\kappa\cos\theta}{k^2 - k_x^2}} - 2\right). \tag{110}$$

Now use the binomial expansion where,

$$\sqrt{1 - x} = 1 - \frac{x}{2} - \frac{x^2}{8} - \frac{x^3}{16} - \cdots$$

$$\approx 1 - \frac{x}{2}. \tag{111}$$

This approximation is very good for the case when $x \ll 1$. Applying the binomial expansion to the square roots of Eq. (110), the following approximation is obtained:

$$\alpha \approx \frac{1}{2}\sqrt{k^2 - k_x^2}\left(1 - \frac{1}{2}\left(\frac{\kappa^2 + 2k_x\kappa\cos\theta}{k^2 - k_x^2}\right)\right.$$

$$\quad \left. + 1 - \frac{1}{2}\left(\frac{\kappa^2 - 2k_x\kappa\cos\theta}{k^2 - k_x^2}\right) - 2\right)$$

$$= \frac{1}{2}\sqrt{k^2 - k_x^2}\left(-\frac{\kappa^2}{k^2 - k_x^2}\right)$$

$$= \frac{1}{2}k_z\left(-\frac{\kappa^2}{k_z^2}\right)$$

$$= \left(\frac{-\kappa^2}{2k_z}\right). \tag{112}$$

92

Finally, for small values of ϑ we use the approximation that $k_z \approx k$ which yields the final form for α as

$$\alpha = \left(\frac{-\kappa^2}{2k} \right).$$

$$(113)$$

Notice that in this final approximation, the k_x dependency has been lost. Under these conditions, α for the reference beacon wave is equal to the α for the object wave. This adds a significant simplification to the analysis in the body of this dissertation. Using the same type of analysis as used for the simplification of α, a simplified expression for β is determined as:

$$
\begin{aligned}
\beta &= \frac{k_z' - k_z''}{2} \\
&= \frac{1}{2}\sqrt{k^2 - (k_x + \kappa\cos\theta)^2 - (\kappa\sin\theta)^2} \\
&\quad - \frac{1}{2}\sqrt{k^2 - (k_x - \kappa\cos\theta)^2 - (\kappa\sin\theta)^2} \\
&\approx \frac{1}{2}\sqrt{k^2 - k_x^2}\left(1 - \frac{1}{2}\left(\frac{\kappa^2 + 2k_x\kappa\cos\theta}{k^2 - k_x^2}\right)\right. \\
&\quad \left. - 1 + \frac{1}{2}\left(\frac{\kappa^2 - 2k_x\kappa\cos\theta}{k^2 - k_x^2}\right)\right) \\
&= \frac{1}{2}\sqrt{k^2 - k_x^2}\left(\frac{-2k_x\kappa\cos\theta}{k^2 - k_x^2}\right) \\
&= -\frac{k_x\kappa}{k_z}\cos\theta.
\end{aligned}
$$

$$(114)$$

To this point, the location of the off axis source has been specified through the k_x component of the propagating wave. A more convenient notation is one that directly specifies the angle relative to the beacon direction. The relation between this angle designated ϑ and the k_x component of the propagating wave is given by

$$\frac{k_x}{k_z} = \tan\vartheta,$$

$$(115)$$

or,

$$\tan^{-1}\left(\frac{k_x}{k_z}\right) = \vartheta.$$

$$(116)$$

93

For small arguments, we use the approximation, $\tan^{-1}(x) \approx x$ to yield

$$\frac{k_x}{k_z} \approx \vartheta. \tag{117}$$

This allows β to be written as

$$\beta = \kappa \vartheta \cos \theta. \tag{118}$$

The vector $\vec{\vartheta}$ is defined to be a vector in the x, y plane with a magnitude equal to the object angle, ϑ, and an orientation along the x axis. With the vector definition of $\vec{\vartheta}$, β is written as

$$\beta = \vec{\kappa} \cdot \vec{\vartheta}. \tag{119}$$

Appendix D. Derivation of amplitude and phase correlation functions

The purpose of this appendix is to derive the correlation function for the residual phase and amplitude of a wavefront in the pupil of an adaptive-optics system. Much of this derivation uses theoretical development given by Tatarski for the case of a wave propagating through turbulence (46). In this derivation, Tatarski's theory is applied to the angle dependent amplitude variations and the 'corrected' angle dependent phase variations as discussed in Appendix C.

The amplitude perturbation equation was derived in Appendix C and defined in complex phasor notation in Chapter II as

$$\underline{P_a}(\vec{x}, \vartheta) = \iint d\eta d\vec{\kappa} \tilde{A}(\eta, \vec{\kappa}) e^{-j(\vec{\kappa} \cdot \vec{x})} \sin(\eta \alpha) e^{jn\beta}. \tag{120}$$

The correlation function is therefore defined by

$$
\begin{aligned}
\underline{\Gamma_a}(\vec{\rho}, \vartheta) &= \langle \underline{P_a}(\vec{x}, \vartheta) \underline{P_a}^*(\vec{x} - \vec{\rho}, \vartheta) \rangle \\
&= \Big\langle \iiiint d\eta_1 d\eta_2 d\vec{\kappa}_1 d\vec{\kappa}_2 \tilde{A}(\eta_1, \vec{\kappa}_1) e^{-j(\vec{\kappa}_1 \cdot \vec{x})} \sin(\eta_1 \alpha_1) e^{jn_1 \beta_1} \\
&\qquad \times \ \tilde{A}^*(\eta_2, \vec{\kappa}_2) e^{-j(\vec{\kappa}_2 \cdot (\vec{x} - \vec{\rho}))} \sin(\eta_2 \alpha_2) e^{jn_2 \beta_2} \Big\rangle. \tag{121}
\end{aligned}
$$

Note that the only random quantities are $\tilde{A}$ and $\tilde{A}^*$. The expectation is passed through the integration and Eq. (86) in Appendix B is used to relate the complex representation of the phase screen variations, $\tilde{A}(\eta, \vec{\kappa})$, to the 2-D refractive index power spectrum, $F(\eta_1 - \eta_2, \kappa)$. The result is the correlation function being written as

$$\underline{\Gamma_a}(\vec{\rho}, \vartheta) = 4k^2 \iiint d\eta_1 d\eta_2 d\vec{\kappa} F(\eta_1 - \eta_2, \kappa) e^{-j\vec{\kappa} \cdot \vec{\rho}} \sin(\eta_1 \alpha) \sin(\eta_2 \alpha) e^{j\beta(\eta_1 - \eta_2)}, \tag{122}$$

where the integration over $d\eta_1$ and $d\eta_2$ are from 0 to the upper level of turbulence given by L and $\kappa = |\vec{\kappa}| = \sqrt{\kappa_x^2 + \kappa_y^2}$. Next, a change of variables is performed in order to represent the

2-D power spectrum as a function of only one variable. Let

$$\Delta\eta = \eta_1 - \eta_2, \tag{123}$$

and,

$$2\Sigma\eta = \eta_1 + \eta_2. \tag{124}$$

Note that the Jacobian for this transformation is 1, and that the following equalities hold:

$$\eta_1 = \frac{\Delta\eta + 2\Sigma\eta}{2}, \tag{125}$$

and,

$$\eta_2 = \frac{2\Sigma\eta - \Delta\eta}{2}. \tag{126}$$

The $d\Delta\eta\, d\Sigma\eta$ integration is now performed over a region D in the $(\Delta\eta, \Sigma\eta)$ plane where D is a rhombus with vertices of $(0,0)$, $(L, \frac{L}{2})$, $(0, L)$, and $(-L, \frac{L}{2})$. The amplitude correlation is now written as

$$
\begin{aligned}
\underline{\Gamma_a}(\vec{\rho}, \vartheta) &= 4k^2 \int d\vec{\kappa}\, e^{-j\vec{\kappa}\cdot\vec{\rho}} \iint_D d\Delta\eta\, d\Sigma\eta\, F(\Delta\eta, \kappa) \\
&\quad \times \sin\left(\alpha\frac{\Delta\eta + 2\Sigma\eta}{2}\right) \sin\left(\alpha\frac{2\Sigma\eta - \Delta\eta}{2}\right) e^{j\beta(\Delta\eta)}. \tag{127}
\end{aligned}
$$

Use the identity,

$$-2\sin\left(\frac{a+b}{2}\right) \sin\left(\frac{a-b}{2}\right) = \cos(a) - \cos(b), \tag{128}$$

to show that

$$\sin\left(\alpha\frac{\Delta\eta + 2\Sigma\eta}{2}\right) \sin\left(\alpha\frac{2\Sigma\eta - \Delta\eta}{2}\right) = \frac{1}{2}(\cos(\alpha\Delta\eta) - \cos(2\alpha\Sigma\eta)). \tag{129}$$

Substituting Eq. (129) into Eq. (127) to yield

$$\underline{\Gamma_a}(\vec{\rho}, \vartheta) = 2k^2 \int d\vec{\kappa} e^{-j\vec{\kappa}\cdot\vec{\rho}} \iint_D d\Delta\eta \, d\Sigma\eta F(\Delta\eta, \kappa) e^{j\beta(\Delta\eta)}(\cos(\alpha\Delta\eta) - \cos(2\alpha\Sigma\eta)) \quad (130)$$

The integrand is even with respect to $\Delta\eta$, so the integration over the region D is twice the value of the integration over the right half plane of D. Therefore,

$$
\begin{aligned}
\underline{\Gamma_a}(\vec{\rho}, \vartheta) = 4k^2 \int d\vec{\kappa} e^{-j\vec{\kappa}\cdot\vec{\rho}} \Big[& \int_0^{\frac{L}{2}} \int_0^{\Sigma\eta} d\Delta\eta \, d\Sigma\eta F(\Delta\eta, \kappa) e^{j\beta(\Delta\eta)}(\cos(\alpha\Delta\eta) - \cos(2\alpha\Sigma\eta)) \\
& + \int_{\frac{L}{2}}^{L} \int_0^{L-\Sigma\eta} d\Delta\eta \, d\Sigma\eta F(\Delta\eta, \kappa) e^{j\beta(\Delta\eta)}(\cos(\alpha\Delta\eta) - \cos(2\alpha\Sigma\eta)) \Big].
\end{aligned}
\quad (131)
$$

It is known that the power spectrum will only have significant values for $\kappa\Delta\eta \ll 1$ (i.e., $F(\Delta\eta, \kappa) \to 0$ for $\kappa\Delta\eta \gg 1$) (46). Therefore, in the region where $0 \leq \kappa\Delta\eta \approx 1$, where $F(\Delta\eta, \kappa)$ has a significant value, $\frac{\kappa^2\Delta\eta}{k} < \frac{\kappa}{k} \ll 1$ and using $\alpha = \frac{\kappa^2}{2k}$ and $\beta = \vec{\kappa} \cdot \vec{\vartheta}$, the following approximations can be used:

$$\cos(\alpha\Delta\eta) = \cos(\frac{\kappa^2\Delta\eta}{2k}) \approx 1, \quad (132)$$

and,

$$e^{j\beta\Delta\eta} = e^{j\Delta\eta\kappa\vartheta\cos\theta} \approx 1. \quad (133)$$

The correlation function is now written as

$$
\begin{aligned}
\underline{\Gamma_a}(\vec{\rho}) = 4k^2 \int d\vec{\kappa} e^{-j\vec{\kappa}\cdot\vec{\rho}} \Big[& \int_0^{\frac{L}{2}} (1 - \cos(2\alpha\Sigma\eta)) \int_0^{\Sigma\eta} d\Delta\eta \, d\Sigma\eta F(\Delta\eta, \kappa) \\
& + \int_{\frac{L}{2}}^{L} (1 - \cos(2\alpha\Sigma\eta)) \int_0^{L-\Sigma\eta} d\Delta\eta \, d\Sigma\eta F(\Delta\eta, \kappa) \Big].
\end{aligned}
\quad (134)
$$

Note that the dependence on ϑ has been lost through the loss of β in the approximation of Eq. (133). The upper limits on $d\Delta\eta$ can be taken to ∞ without significantly changing the result. Now use the relation given by Tatarski that relates the 2-D power spectrum to the 3-D

97

power spectrum, $\Phi(\kappa)$ (46):

$$\int_0^\infty d\Delta\eta \, F(\Delta\eta, \kappa) = \pi\Phi(\kappa).\tag{135}$$

The amplitude correlation function is now written as

$$
\begin{aligned}
\underline{\Gamma_a}(\vec{\rho}) &= 4k^2\pi \int d\vec{\kappa} e^{-j\vec{\kappa}\cdot\vec{\rho}}\Phi(\kappa)\left(\int_0^{\frac{L}{2}} d\Sigma\eta(1-\cos(2\alpha\Sigma\eta))\right. \\
&\qquad + \left.\int_{\frac{L}{2}}^L d\Sigma\eta(1-\cos(2\alpha\Sigma\eta))\right) \\
&= 4k^2\pi \int d\vec{\kappa} e^{-j\vec{\kappa}\cdot\vec{\rho}}\Phi(\kappa)\int_0^L d\Sigma\eta(1-\cos(2\alpha\Sigma\eta)).\tag{136}
\end{aligned}
$$

Use the identity,

$$1-\cos(2a) = 2\sin^2(a),\tag{137}$$

or,

$$1-\cos(2\alpha\Sigma\eta) = 2\sin^2(\alpha\Sigma\eta),\tag{138}$$

to write Eq. (136) as

$$\underline{\Gamma_a}(\vec{\rho}) = 8k^2\pi \int d\vec{\kappa} e^{-j\vec{\kappa}\cdot\vec{\rho}}\Phi(\kappa)\int_0^L d\Sigma\eta \sin^2(\alpha\Sigma\eta).\tag{139}$$

Now use the property that the real valued correlation function is equal to one half the real portion of the complex valued correlation function, (i.e., $\Gamma_a(\vec{\rho}) = \frac{1}{2}\mathcal{R}\{\underline{\Gamma_a}(\vec{\rho})\}$). This yields a final correlation function of

$$
\begin{aligned}
\Gamma_a(\vec{\rho}) &= 4k^2\pi \int d\vec{\kappa} \cos(\vec{\kappa}\cdot\vec{\rho})\Phi(\kappa)\int_0^L d\Sigma\eta \sin^2(\alpha\Sigma\eta) \\
&= 4k^2\pi \int\int d\eta d\vec{\kappa} \cos(\vec{\kappa}\cdot\vec{\rho})\Phi(\kappa)\sin^2(\alpha\eta).\tag{140}
\end{aligned}
$$

Equation (140) represents the final form of the amplitude correlation function used in the body of this dissertation. Note that at this point Eq. (140) could be changed to polar coordinates where $d\vec{\kappa} = \kappa \, d\kappa d\theta$ and the integration over $d\theta$ goes from 0 to π. The integration over $d\theta$

98

can then be performed analytically using the relation

$$\int_0^\pi \cos(a\cos(\theta))\mathrm{d}\theta = \pi J_0(a),\tag{141}$$

where J_0 is the zeroth order Bessel function of the first kind. The correlation function is now written as

$$\begin{aligned}\Gamma_a(\vec{\rho}) &= 4k^2\pi\iiint \mathrm{d}\theta\mathrm{d}\kappa\mathrm{d}\eta \ \kappa\cos(\kappa\rho\cos(\theta))\Phi(\kappa)\sin^2(\alpha\eta)\\ &= 4k^2\pi^2\iint \mathrm{d}\eta\mathrm{d}\kappa \ \kappa J_0(\kappa\rho)\Phi(\kappa)\sin^2(\alpha\eta).\end{aligned}\tag{142}$$

This is the exact form of the amplitude correlation function given by Tatarski and also used by Lee and Harp (30, 46). Note that the amplitude correlation function is not a function of object angle. Recall that an assumption was made regarding the size of the object angle in this derivation. However, the condition for the assumption will always be meet in practical applications.

Next, consider the correlation of the residual phase in the pupil of an adaptive–optics system. The residual phase perturbation equation was derived in Appendix C and defined in complex phasor notation in Chapter II as:

$$\underline{\Delta P_p}(\vec{x},\vartheta) = \iint \mathrm{d}\eta\mathrm{d}\vec{\kappa}\tilde{A}(\eta,\vec{\kappa})e^{-j(\vec{\kappa}\cdot\vec{x})}\cos(\eta\alpha)(1-e^{jn\beta}).\tag{143}$$

The correlation of the residual phase in then given by

$$\begin{aligned}\underline{\Gamma_p}(\vec{\rho},\vartheta) &= \langle\underline{P_p}(\vec{x},\vartheta)\underline{P_p}^*(\vec{x}-\vec{\rho},\vartheta)\rangle\\ &= \Big\langle\iiiint \mathrm{d}\eta_1\mathrm{d}\eta_2\mathrm{d}\vec{\kappa}_1\mathrm{d}\vec{\kappa}_2\tilde{A}(\eta_1,\vec{\kappa}_1)e^{-j(\vec{\kappa}_1\cdot\vec{x})}\cos(\eta_1\alpha_1)(1-e^{j\eta_1\beta_1})\\ &\quad\times\ \tilde{A}^*(\eta_2,\vec{\kappa}_2)e^{-j(\vec{\kappa}_2\cdot(\vec{x}-\vec{\rho}))}\cos(\eta_2\alpha_2)(1-e^{-j\eta_2\beta_2})\Big\rangle.\end{aligned}\tag{144}$$

Again, note that the only random quantities are $\tilde{A}$ and $\tilde{A}^*$. The expectation is passed through the integration and use Eq. (86) in Appendix B is used to yield

$$
\begin{aligned}
\underline{\Gamma}_p(\vec{\rho}, \vartheta) \;=\; & 4k^2 \int \mathrm{d}\vec{\kappa}\, e^{-j\vec{\kappa}\cdot\vec{\rho}} \int\!\!\int \mathrm{d}\eta_1 \mathrm{d}\eta_2 F(\eta_1 - \eta_2, \kappa) \\
& \times\; \cos(\eta_1\alpha)\cos(\eta_2\alpha)(1 - e^{j\beta\eta_1})(1 - e^{-j\beta\eta_2}),
\end{aligned}
\tag{145}
$$

where the integration over $\mathrm{d}\eta_1$ and $\mathrm{d}\eta_2$ are from 0 to the upper level of turbulence given by L and $\kappa = |\vec{\kappa}| = \sqrt{\kappa_x^2 + \kappa_y^2}$. The same change of variables given by Eqs. (123) and (124) is now used to yield

$$
\begin{aligned}
\underline{\Gamma}_p(\vec{\rho}, \vartheta) \;=\; & 4k^2 \int \mathrm{d}\vec{\kappa}\, e^{-j\vec{\kappa}\cdot\vec{\rho}} \int\!\!\int_D \mathrm{d}\Delta\eta\, \mathrm{d}\Sigma\eta\, F(\Delta\eta, \kappa) \\
& \times\; \cos\left(\alpha\frac{\Delta\eta + 2\Sigma\eta}{2}\right) \cos\left(\alpha\frac{2\Sigma\eta - \Delta\eta}{2}\right) \left(1 - e^{j\beta\frac{\Delta\eta + 2\Sigma\eta}{2}}\right) \left(1 - e^{-j\beta\frac{2\Sigma\eta - \Delta\eta}{2}}\right).
\end{aligned}
\tag{146}
$$

Use the identity,

$$
-2\cos(\frac{a+b}{2})\cos(\frac{a-b}{2}) = \cos(a) + \cos(b),
\tag{147}
$$

to show that

$$
\cos\left(\alpha\frac{\Delta\eta + 2\Sigma\eta}{2}\right) \cos\left(\alpha\frac{2\Sigma\eta - \Delta\eta}{2}\right) = \frac{1}{2}(\cos(2\alpha\Sigma\eta) + \cos(\alpha\Delta\eta)).
\tag{148}
$$

The residual phase correlation correlation is now written as

$$
\begin{aligned}
\underline{\Gamma}_p(\vec{\rho}, \vartheta) \;=\; & 2k^2 \int \mathrm{d}\vec{\kappa}\, e^{-j\vec{\kappa}\cdot\vec{\rho}} \int\!\!\int_D \mathrm{d}\Delta\eta\, \mathrm{d}\Sigma\eta\, F(\Delta\eta, \kappa) \\
& \times\; (1 - e^{j\beta\frac{\Delta\eta + 2\Sigma\eta}{2}})(1 - e^{-j\beta\frac{2\Sigma\eta - \Delta\eta}{2}})(\cos(2\alpha\Sigma\eta) + \cos(\alpha\Delta\eta)),
\end{aligned}
\tag{149}
$$

where again the $\mathrm{d}\Delta\eta\, \mathrm{d}\Sigma\eta$ integration is over the region D in the $(\Delta\eta, \Sigma\eta)$ plane. Next, consider the term

$$
(1 - e^{j\beta\frac{\Delta\eta + 2\Sigma\eta}{2}})(1 - e^{-j\beta\frac{2\Sigma\eta - \Delta\eta}{2}}).
\tag{150}
$$

100

First, let $a = \beta \Sigma \eta$ and $b = \beta \frac{\Delta \eta}{2}$. The terms of Eq. (150) can then be simplified as

$$
\begin{aligned}
(1 - e^{j(a+b)})(1 - e^{-j(a-b)}) &= 1 - e^{-j(a-b)} - e^{j(a+b)} + e^{j2b} \\
&= 1 + e^{j2b} - e^{jb}(e^{ja} + e^{-ja}) \\
&= 1 + e^{j2b} - e^{jb}(2\cos(a)).
\end{aligned}
\tag{151}
$$

Therefore,

$$
(1 - e^{j\beta \frac{\Delta \eta + 2\Sigma \eta}{2}})(1 - e^{-j\beta \frac{2\Sigma \eta - \Delta \eta}{2}}) = 1 + e^{j\beta \Delta \eta} - e^{j\beta \frac{\Delta \eta}{2}}(2\cos(\beta \Sigma \eta)).
\tag{15?}
$$

Substituting Eq. (152) into Eq. (149) yields

$$
\begin{aligned}
\underline{\Gamma_p}(\vec{\rho}, \vartheta) &= 2k^2 \int d\vec{\kappa} e^{-j\vec{\kappa} \cdot \vec{\rho}} \iint_D d\Delta \eta \, d\Sigma \eta \, F(\Delta \eta, \kappa) \\
&\quad \times (1 + e^{j\beta \Delta \eta} - e^{j\beta \frac{\Delta \eta}{2}}(2\cos(\beta \Sigma \eta)))(\cos(2\alpha \Sigma \eta) + \cos(\alpha \Delta \eta)).
\end{aligned}
\tag{153}
$$

The integration over the region D is again taken to be twice the value of the integration over the right half plane of D. Therefore,

$$
\begin{aligned}
\underline{\Gamma_p}(\vec{\rho}, \vartheta) &= 4k^2 \int d\vec{\kappa} e^{-j\vec{\kappa} \cdot \vec{\rho}} \Bigg[\int_0^{\frac{L}{2}} \int_0^{\Sigma \eta} d\Delta \eta \, d\Sigma \eta \, F(\Delta \eta, \kappa) \\
&\quad \times (1 + e^{j\beta \Delta \eta} - e^{j\beta \frac{\Delta \eta}{2}}(2\cos(\beta \Sigma \eta)))(\cos(2\alpha \Sigma \eta) + \cos(\alpha \Delta \eta)) \\
&\quad + \int_{\frac{L}{2}}^{L} \int_0^{L - \Sigma \eta} d\Delta \eta \, d\Sigma \eta \, F(\Delta \eta, \kappa) \\
&\quad \times (1 + e^{j\beta \Delta \eta} - e^{j\beta \frac{\Delta \eta}{2}}(2\cos(\beta \Sigma \eta)))(\cos(2\alpha \Sigma \eta) + \cos(\alpha \Delta \eta)) \Bigg].
\end{aligned}
\tag{154}
$$

Again, $F(\Delta \eta, \kappa) \rightarrow 0$ for $\kappa \Delta \eta \gg 1$. Therefore, in the region where $0 \leq \kappa \Delta \eta \approx 1$, the following approximations are made:

$$
\begin{aligned}
\cos(\alpha \Delta \eta) &= \cos(\frac{\kappa^2 \Delta \eta}{2k}) \approx 1, \\
e^{j\beta \Delta \eta} &= e^{j\Delta \eta \kappa \vartheta \cos \theta} \approx 1, \\
e^{j\frac{\beta \Delta \eta}{2}} &= e^{j\frac{\Delta \eta \kappa \vartheta}{2} \cos \theta} \approx 1.
\end{aligned}
\tag{155}
$$

101

With the above approximations, the correlation function is now written as

$$\underline{\Gamma_p}(\vec{\rho}, \vartheta) = 4k^2 \int d\vec{\kappa} e^{-j\vec{\kappa}\cdot\vec{\rho}} \left[\int_0^{\frac{L}{2}} d\Sigma\eta (2 - 2\cos(\beta\Sigma\eta))(\cos(2\alpha\Sigma\eta) + 1) \int_0^{\Sigma\eta} d\Delta\eta F(\Delta\eta, \kappa) \right.$$
$$\left. + \int_{\frac{L}{2}}^L d\Sigma\eta (2 - 2\cos(\beta\Sigma\eta))(\cos(2\alpha\Sigma\eta) + 1) \int_0^{L-\Sigma\eta} d\Delta\eta F(\Delta\eta, \kappa) \right]. \quad (156)$$

The upper limits on $d\Delta\eta$ can be taken to ∞ without significantly changing the result. Now use the relation given by Tatarski that relates the 2–D power spectrum to the 3–D power spectrum, $\Phi(\kappa)$ (46), as given in Eq. (135), to yield

$$\underline{\Gamma_p}(\vec{\rho}, \vartheta) = 8\pi k^2 \int d\vec{\kappa} e^{-j\vec{\kappa}\cdot\vec{\rho}} \Phi(\kappa) \int_0^L d\Sigma\eta (1 - \cos(\beta\Sigma\eta))(\cos(2\alpha\Sigma\eta) + 1)$$
$$= 8\pi k^2 \iint d\eta d\vec{\kappa} e^{-j\vec{\kappa}\cdot\vec{\rho}} \Phi(\kappa)(1 - \cos(\beta\eta))(\cos(2\alpha\eta) + 1). \quad (157)$$

Use the relation

$$\cos(2\alpha\eta) + 1 = 2\cos^2(\alpha\eta), \quad (158)$$

to write the final form of the complex representation of the residual phase correlation function as

$$\underline{\Gamma_p}(\vec{\rho}, \vartheta) = 16\pi k^2 \iint d\eta d\vec{\kappa} e^{-j\vec{\kappa}\cdot\vec{\rho}} \Phi(\kappa)(1 - \cos(\beta\eta)) \cos^2(\alpha\eta). \quad (159)$$

Again, use the property that the real valued correlation function is equal to one half the real portion of the complex valued correlation function to yield a final correlation function of

$$\Gamma_p(\vec{\rho}, \vartheta) = 8\pi k^2 \iint d\eta d\vec{\kappa} \cos(\vec{\kappa}\cdot\vec{\rho}) \Phi(\kappa)(1 - \cos(\beta\eta)) \cos^2(\alpha\eta). \quad (160)$$

This is the form of the residual phase correlation function used in the body of this dissertation. Note that the residual phase correlation can not be analytically integrated over $d\theta$ due to the $\cos(\beta\eta) = \cos(\vec{\kappa}\cdot\vec{\vartheta}\eta) = \cos(\eta\kappa\vartheta\cos(\theta))$ term.

Appendix E. The geometric optics approximation

The purpose of this appendix is to show a direct comparison between the average phase OTF expression, $\langle H_p(\vec{\rho}, \vartheta) \rangle$, derived using the diffraction method given in Chapter II and the OTF expression given by Fried using the geometric optics approximation (10). The usefulness of this comparison is in giving confidence that the analysis of the OTF as presented in the body of this dissertation has been properly performed, and in identifying the portion of the OTF equation that defines the diffraction effects. This comparison is made by beginning with the diffraction based OTF and determining what assumptions need be be made to yield the equation given by Fried.

In developing properties of atmospheric turbulence, Goodman (14) addresses the concept of geometric optics by defining the 'near field' region as the region where $\eta \ll \frac{\pi k}{\kappa^2}$. Note that this is a relation between the altitude of turbulence and the wavenumber of the turbulence for a given propagating wavenumber. If the turbulence is close to the optics, 'near field' conditions exist. When $\eta \ll \frac{\pi k}{\kappa^2}$, we can also say that $\frac{\eta \kappa^2}{2k} \ll 1$ and the assumption $\cos^2(\frac{\eta \kappa^2}{2k}) \approx 1$ is used. The following derivation shows that the 'near field' assumption along with a specific refractive index power spectrum is the only difference between the diffraction calculation for $\langle H_p(\vec{\rho}, \vartheta) \rangle$ and Fried's geometric optics OTF calculations.

With the assumption of $\cos^2(\frac{\eta \kappa^2}{2k}) \approx 1$, the phase correlation of Eq. (26) is written as

$$
\begin{aligned}
\Gamma_p(\vec{\rho}, \vartheta) &= 8\pi k^2 \iint \Phi(\vec{\kappa}, \eta) \cos(\vec{\kappa} \cdot \vec{\rho})[1 - \cos(\eta \vec{\kappa} \cdot \vec{\vartheta})] d\vec{\kappa} d\eta \\
&= 8\pi k^2 \Big[\iint \Phi(\vec{\kappa}, \eta) \cos(\vec{\kappa} \cdot \vec{\rho}) d\vec{\kappa} d\eta \\
&\qquad - \iint \Phi(\vec{\kappa}, \eta) \cos(\vec{\kappa} \cdot \vec{\rho}) \cos(\eta \vec{\kappa} \cdot \vec{\vartheta}) d\vec{\kappa} d\eta \Big].
\end{aligned}
\tag{161}
$$

The integration over $\vec{\kappa}$ is broken into polar coordinates where $d\vec{\kappa} = \kappa \, d\kappa \, d\theta$. The integration limits are: κ – from 0 to ∞, θ – from 0 to π, and η – from 0 to L, the altitude of the source.

Next, expand the dot products of Eq. (161) noting that θ defines the orientation of $\vec{\kappa}$, θ_ρ defines the orientation of $\vec{\rho}$ and the orientation of $\vec{\vartheta}$ defines the x axis (i.e., $\theta_\vartheta = 0$).

103

Equation (161) is now written as

$$\Gamma_p(\rho, \theta_\rho, \vartheta) = 8\pi k^2 \Bigg[\int_0^L \int_0^\infty \int_0^\pi \kappa \Phi(\vec{\kappa}, \eta) \cos(\kappa\rho\cos(\theta - \theta_\rho)) \mathrm{d}\theta \mathrm{d}\kappa \mathrm{d}\eta$$

$$- \int_0^L \int_0^\infty \int_0^\pi \kappa \Phi(\vec{\kappa}, \eta) \cos(\kappa\rho\cos(\theta - \theta_\rho)) \cos(\eta\kappa\vartheta\cos(\theta)) \mathrm{d}\theta \mathrm{d}\kappa \mathrm{d}\eta \Bigg] (162)$$

The integration over θ in the first integration term of Eq. (162) is solved using the following property:

$$\int_0^\pi \cos(a\cos(\theta + b)) \mathrm{d}\theta = \pi J_0(a) \tag{163}$$

where, $J_0(a)$ represents the zero order Bessel function of the first kind. Therefore,

$$\int_0^L \int_0^\infty \int_0^\pi \kappa \Phi(\kappa, \eta) \cos(\kappa\rho\cos(\theta - \theta_\rho)) \mathrm{d}\theta \mathrm{d}\kappa \mathrm{d}\eta = \pi \int_0^L \int_0^\infty \kappa \Phi(\kappa, \eta) J_0(\kappa\rho) \mathrm{d}\kappa \mathrm{d}\eta.$$

$$\tag{164}$$

To evaluate the integration over θ in the second integration term of Eq. (162), first write the cosine terms $\cos(\kappa\rho\cos(\theta - \theta_\rho)) \cos(\eta\kappa\vartheta\cos(\theta))$ as

$$\cos(a\cos c)\cos(b\cos d) = \frac{1}{2}\cos(a\cos c - b\cos d) + \frac{1}{2}\cos(a\cos c + b\cos d), \quad (165)$$

where $a = \kappa\rho$, $b = \eta\kappa\vartheta$, $c = \theta - \theta_p$, and $d = \theta$. Note that d can be written as $d = c + c'$ where $c' = \theta_p$. Now consider the term $a\cos c + b\cos d$.

$$\begin{aligned}
a\cos c + b\cos d &= \frac{a}{2}(e^{jc} + e^{-jc}) + \frac{b}{2}(e^{jd} + e^{-jd}) \\
&= \frac{a}{2}(e^{jc} + e^{-jc}) + \frac{b}{2}(e^{j(c+c')} + e^{-j(c+c')}) \\
&= \frac{e^{jc}}{2}(a + be^{jc'}) + \frac{e^{-jc}}{2}(a + be^{-jc'}) \\
&= \frac{ze^{jc}}{2} + \frac{z^*e^{-jc}}{2} \\
&= \frac{|z|e^{j\arg z}}{2}e^{jc} + \frac{|z|e^{-j\arg z}}{2}e^{-jc} \\
&= |z|\cos(c + \arg z), \tag{166}
\end{aligned}$$

104

with $d = c + c'$ and $z = a + be^{jc'}$. So,

$$\cos(a\cos c)\cos(b\cos d) = \frac{1}{2}[\cos(|z|\cos(c + \arg z)) + \cos(|z'|\cos(c + \arg z'))], \quad (167)$$

where $z' = a - be^{jc'}$. Therefore, the second integration term of Eq. (162) can be written as

$$\int_0^L \int_0^\infty \int_0^\pi \kappa\Phi(\kappa,\eta)\frac{1}{2}[\cos(|z|\cos(c + \arg(z))) + \cos(|z'|\cos(c + \arg(z')))]d\theta d\kappa d\eta \quad (168)$$

where,

$$
\begin{aligned}
z &= \kappa\rho + (\eta\kappa\vartheta)e^{j\theta_\rho}, \\
z' &= \kappa\rho - (\eta\kappa\vartheta)e^{j\theta_\rho}, \\
|z| &= \kappa\sqrt{\rho^2 + 2\rho\eta\vartheta\cos\theta_\rho + (\eta\vartheta)^2}, \\
|z'| &= \kappa\sqrt{\rho^2 - 2\rho\eta\vartheta\cos\theta_\rho + (\eta\vartheta)^2}.
\end{aligned}
\quad (169)
$$

The $d\theta$ integration of Eq. (168) is accomplished using Eq. (163). The result of the integration over θ yields:

$$
\frac{1}{2}\pi\int_0^L \int_0^\infty \kappa\Phi(\kappa,\eta)\left(J_0(\kappa\sqrt{\rho^2 + 2\rho\eta\vartheta\cos\theta_\rho + (\eta\vartheta)^2})\right.
$$
$$
\left. + J_0(\kappa\sqrt{\rho^2 - 2\rho\eta^{:9}\cos\theta_\rho + (\eta\vartheta)^2})\right)d\kappa d\eta. \quad (170)
$$

Therefore, the phase correlation is written as

$$
\begin{aligned}
\Gamma_p(\rho,\theta_\rho,\vartheta) &= 8\pi^2 k^2 \int_0^L \int_0^\infty \kappa\Phi(\kappa,\eta)\left[J_0(\kappa\rho)\right. \\
&\quad - \frac{1}{2}J_0\left(\kappa\sqrt{\rho^2 + 2\rho\eta\vartheta\cos\theta_\rho + (\eta\vartheta)^2}\right) \\
&\quad \left. - \frac{1}{2}J_0\left(\kappa\sqrt{\rho^2 - 2\rho\eta\vartheta\cos\theta_\rho + (\eta\vartheta)^2}\right)\right]d\kappa d\eta
\end{aligned}
\quad (171)
$$

and,

$$
\begin{aligned}
\Gamma_p(0, \theta_\rho, \vartheta) &= 8\pi^2 k^2 \int_0^L \int_0^\infty \kappa \Phi(\kappa, \eta) \left[J_0(0) - \frac{1}{2} J_0(\kappa \eta \vartheta) - \frac{1}{2} J_0(\kappa \eta \vartheta) \right] d\kappa d\eta \\
&= 8\pi^2 k^2 \int_0^L \int_0^\infty \kappa \Phi(\kappa, \eta) [J_0(0) - J_0(\kappa \eta \vartheta)] d\kappa d\eta \\
&= 8\pi^2 k^2 \int_0^L \int_0^\infty \kappa \Phi(\kappa, \eta) [1 - J_0(\kappa \eta \vartheta)] d\kappa d\eta
\end{aligned} \tag{172}
$$

Now let $S(\rho, \theta_\rho, \vartheta) = \Gamma_p(0, \theta_\rho, \vartheta) - \Gamma_p(\rho, \theta_\rho, \vartheta)$, and $\langle H_p(\rho, \theta_\rho, \vartheta) \rangle = \exp[-S(\rho, \theta_\rho, \vartheta)]$. Therefore,

$$
\begin{aligned}
S(\rho, \theta_\rho, \vartheta) &= 8\pi^2 k^2 \int_0^L \int_0^\infty \kappa \Phi(\kappa, \eta) [1 - J_0(\kappa \eta \vartheta) - J_0(\kappa \rho) \\
&\quad + \frac{1}{2} J_0(\kappa \sqrt{\rho^2 + 2\rho \eta \vartheta \cos \theta_\rho + (\eta \vartheta)^2}) \\
&\quad - \frac{1}{2} J_0(\kappa \sqrt{\rho^2 - 2\rho \eta \vartheta \cos \theta_\rho + (\eta \vartheta)^2})] d\kappa d\eta
\end{aligned} \tag{173}
$$

If the atmospheric refractive index power spectrum is represented by the Kolmogorov spectrum, as discussed in Appendix A, the integration over κ can be solved analytically. Let the power spectrum be given by

$$
\Phi(\kappa, \eta) = 0.033 C_n^2(\eta) \kappa^{-\frac{11}{3}}. \tag{174}
$$

Now, Eq. (173) is written as

$$
\begin{aligned}
S(\rho, \theta_\rho, \vartheta) &= 8\pi^2 k^2 0.033 \int_0^L C_n^2(\eta) \left[\int_0^\infty \kappa^{-\frac{8}{3}} (1 - J_0(\kappa \rho)) d\kappa \right. \\
&\quad + \int_0^\infty \kappa^{-\frac{8}{3}} (1 - J_0(\kappa \eta \vartheta)) d\kappa \\
&\quad + \frac{1}{2} \int_0^\infty \kappa^{-\frac{8}{3}} \left(1 - J_0(\kappa \sqrt{\rho^2 + 2\rho \eta \vartheta \cos \theta_\rho + (\eta \vartheta)^2}) \right) d\kappa \\
&\quad \left. + \frac{1}{2} \int_0^\infty \kappa^{-\frac{8}{3}} \left(1 - J_0(\kappa \sqrt{\rho^2 - 2\rho \eta \vartheta \cos \theta_\rho + (\eta \vartheta)^2}) \right) d\kappa \right] d\eta,
\end{aligned} \tag{175}
$$

where an integration of $\int_0^\infty \kappa^{-\frac{8}{3}}\mathrm{d}\kappa$ has been added and subtracted to obtain a desirable form. Using the following integration relation,

$$
\begin{aligned}
\int_0^\infty \kappa^{-\frac{8}{3}}(1 - J_0(a\kappa))\mathrm{d}\kappa &= \frac{(a^2)^{5/6}\pi}{2^{5/3}\Gamma(\frac{11}{6})^2} \\
&= 1.11833\, a^{5/3}, \quad\quad (176)
\end{aligned}
$$

the final expression for $S(\rho, \theta_\rho, \vartheta)$ is given by

$$
\begin{aligned}
S(\rho, \theta_\rho, \vartheta) &= 2.91\kappa^2 \int_0^L C_n^2(\eta)\Big[\rho^{\frac{5}{3}} + (\eta\vartheta)^{\frac{5}{3}} - \frac{1}{2}(\rho^2 + 2\rho\eta\vartheta\cos\theta_\rho + (\eta\vartheta)^2)^{\frac{5}{6}} \\
&\quad - \frac{1}{2}(\rho^2 - 2\rho\eta\vartheta\cos\theta_\rho + (\eta\vartheta)^2)^{\frac{5}{6}}\Big]\mathrm{d}\eta. \quad\quad (177)
\end{aligned}
$$

By referring to Fried's paper and assuming plane wave propagation, it is seen that the same results have been obtained through completely different methods of analysis. Note that the 'near field' condition of $\eta \ll \frac{\pi k}{\kappa^2}$ that allows the approximation of $\cos^2(\frac{\eta\kappa^2}{2k}) \approx 1$ is the same that will allow the approximation of $\sin^2(\frac{\eta\kappa^2}{2k}) \approx 0$. By referring to Eq. (18) in Section 2.3, it is seen that this approximation results in the amplitude OTF being equal to one (i.e., $\langle H_a(\vec{\rho})\rangle = 1$). The conclusion of the analysis in this appendix is that imposing the 'near field' condition on the diffraction based OTF calculation, results in the geometric optics based OTF. Also, by assuming a Kolmogorov power spectrum, the same OTF solution is achieved as the one proposed by Fried.

Bibliography

1. Babcock, H. W. "The possibility of compensating astronomical seeing," *Pub. Astron. Soc. Pac.*, *65*(386):229–236 (October 1953).

2. Babcock, Horace W. "Adaptive Optics Revisited," *Science*, *249*:253–257 (July 1990).

3. Bufton, Jack L., et al. "Measurements of turbulence profiles in the troposphere," *J. Opt. Soc. Am.*, *62*(9):1068–1070 (September 1972).

4. Clifford, Steven F. and John W. Strohbehn. "The Theory of Microwave Line–of–Sight Propagation Through a Turbulent Atmosphere," *IEEE Trans. on Antennas and Propagation*, *AP-18*(2):264–274 (March 1970).

5. Cochran, Gregory. *The impact of scintillation on wavefront reconstruction in the SOR-3 experiments*. Technical Report TR-766, Placentia, CA: the Optical Sciences Company, November 1986.

6. Coulman, C. E. and J. Vernin. "Significance of anisotropy and the outer scale of turbulence for optical and radio seeing," *Appl. Opt.*, *30*(1):118–126 (1 January 1991).

7. Fante, Ronald L. "Electromagnetic Beam Propagation in Turbulent Media," *Proc. IEEE*, *63*(12):1669–1689 (December 1975).

8. Finkbeiner, Ann. "Untwinkling the Stars," *Science*, *252*:1786–1787 (28June 1991).

9. Fried, D. L. "Optical resolution through a randomly inhomogeneous medium for very long and very short exposures," *J. Opt. Soc. Am.*, *56*:1372–1379 (1966).

10. Fried, D. L. "Anisoplanatism in Adaptive optics," *J. Opt. Soc. Am.*, *72*:52–61 (January 1982).

11. Fugate, Robert Q. and others, "Experimental demonstration of real time atmospheric compensation with adaptive optics employing laser guide stars." Presented at the Seattle meeting of the American Astronomical Society, 1991.

12. Fugate, R.Q., et al. "Two generations of laser–guide–star adaptive–optics experiments at the Starfire Optical Range," *J. Opt. Soc. Am. A*, *11*(1):310–324 (January 1994).

13. Gardner, Chester S. and others. "Design and performance analysis of adaptive optical telescopes using laser guide stars," *Proc. IEEE*, *78*(11):1721–1743 (November 1990).

14. Goodman, Joseph W. *Statistical Optics*. New York: John Wiley & Sons, 1985.

15. Greenwood, D. P. "Bandwidth specification for adaptive optics systems," *J. Opt. Soc. Am.*, *67*(3):390 (March 1977).

16. Greenwood, Darryl P. and David L. Fried. "Power spectra requirements for wave-front-compensative systems," *J. Opt. Soc. Am.*, *66*(3):193–206 (March 1976).

17. Greenwood, Darryl P. and Charles A. Primmerman. "Adaptive optics research at Lincoln Laboratory," *Lincoln Laboratory Journal*, *5*(1):3–24 (1992).

18. Hardy, John W. "Active optics: A new technology for the control of light," *Proc. IEEE*, 66(6):651-697 (June 1978).

19. Hardy, John W. "Active optics—don't build a telescope without it!." *Proceedings of the SPIE332*. 252-259. 1982.

20. Hecht, Eugene and Alfred Zajac. *Optics*. Reading, MA: Addison-Wesley Publishing Company, February 1979.

21. Hufnagel, R. E. "Variations of atmospheric turbulence." *Digest of Technical Papers, Topical Meeting on Optical Propagation through Turbulence*. 1974.

22. Johnston, D. *Increasing the Corrected Field of View of an Adaptive Optical Telescope*. MS thesis, AFIT/DS/ENG/92-06, School of Engineering, Air Force Institute of Technology, Wright-Patterson AFB, Oh 45433, December 1992.

23. Johnston, D.C. and B.M. Welsh. "Analysis of multiconjugate adaptive optics," *J. Opt. Soc. Am. A*, 11(1):394-408 (January 1994).

24. Johnston, Dustin C. and Byron M. Welsh. "Estimating contributions of turbulent layers to total wavefront phase aberration." *Atmospheric Propagation and Remote Sensing, Proc. SPIE1688*, edited by A. Kohnle and W. B. Miller. preprint. 1992.

25. Johnston, Dustin C. and Byron M. Welsh. "Estimating the contribution of different parts of the atmosphere to optical wavefront aberration," *Computers and Electrical Engineering* (1992). Accepted for publication, December, 1991.

26. Koeffler, S. *Remote Sensing of Turbulence and Transverse Atmospheric Wind Profiles Using Optical Reference Sources*. MS thesis, AFIT/GE/ENG/92D-22, School of Engineering, Air Force Institute of Technology, Wright-Patterson AFB, Oh 45433, December 1992.

27. Kolmogoroff, A. N. "Dissipation of energy in the locally isotropic turbulence." *Turbulence, Classic Papers on Statistical Theory* edited by S. K. Friedlander and L. Topper, 159-161, Wiley-Interscience, New York, 1961.

28. Korff, D. "Analysis of a method for obtaining near-diffraction-limited information in the presence of atmospheric turbulence," *J. Opt. Soc. Am.*, 63(8):971-980 (1973).

29. Lawrence, R. S., et al. "Measurements of atmospheric turbulence relevant to optical propagation," *J. Opt. Soc. Am.*, 60(6):826-830 (June 1970).

30. Lee, Robert W. and Jeffery C. Harp. "Weak Scattering in Random Media, with Applications to Remote Probing," *Proc. IEEE*, 57(4):375-406 (April 1969).

31. Lemonick, Michael D. "Who Needs the Hubble?," *Time*, 90 (22 October 1990).

32. McKechnie, T. Stewart. "Light propagation through the atmosphere and the properties of images formed by large ground-based telescopes," *J. Opt. Soc. Am. A*, 8(2):346-365 (February 1991).

33. McKechnie, T. Stewart. "Atmospheric turbulence and the resolution limits of large ground-based telescopes," *J. Opt. Soc. Am. A*, 9(11):1937-1954 (November 1992).

109

34. Merkle, Fritz and Jacques M. Beckers. "Application of adaptive optics to astronomy." *Active Telescope Systems, Proc. SPIE1114*, edited by Francois Roddier. 36-42. 1989.

35. Miller, M., et al. "Characterization of Atmospheric Turbulence." *Proceedings of the SPIE/SPSE Technical Symposium East on Imaging Through The Atmosphere75*, edited by James C. Wyant. March 1977.

36. Murphy, Daniel V. "Atmospheric-turbulence compensation experiments using cooperative beacons," *Lincoln Laboratory Journal*, 5(1):25-44 (1992).

37. Ochs, G. R., et al. "Stellar-scintillation measurement of the vertical profile of refractive-index turbulence in the atmosphere." *Imaging through the Atmosphere, Proc. SPIE75*. 48-54. 1976.

38. Pennington, T. *Performance Comparison of Shearing Interferometer and Hartmann Wave Front Sensor*. MS thesis, AFIT/GE/ENG/93D-31, School of Engineering, Air Force Institute of Technology, Wright-Patterson AFB, Oh 45433, December 1993.

39. Press, William H. and others. *Numerical Recipes*. New York: Cambridge, 1987.

40. Reed, I. S. "On a moment theorem for complex Gaussian processes," *IRE Transactions on Information Theory*, 194-195 (April 1962).

41. Rocca, A., et al. "Detection of atmospheric turbulent layers by spatiotemporal and spatioangular correlation measurements of stellar light scintillation," *J. Opt. Soc. Am.*, 64(7):1000-1004 (July 1974).

42. Roggemann, M.C. and C.L. Matson. "Power spectrum and Fourier phase spectrum estimation by using fully and partially compensating adaptive optics and bispectrum postprocessing," *J. Opt. Soc. Am. A*, 9(9):1525-1535 (September 1992).

43. Roggemann, Michael C. "Limited Degree-of-Freedom Adaptive Optics and Image Reconstruction," *Appl. Opt.*, 30(29):4227-4233 (10 October 1991).

44. Stoudt, C. *Improved Quality of Reconstructed Images Through Sifting of data in Statistical Image Reconstruction*. MS thesis, AFIT/GE0/ENG/93D-03, School of Engineering, Air Force Institute of Technology, Wright-Patterson AFB, Oh 45433, December 1993

45. Stover, Dawn. "Laser guide star," *Popular Science*, 23 (September 1991).

46. Tatarski, V. I. *Wave Propagation in a Turbulent Medium*. New York: McGraw-Hill Book Company, Inc., 1961.

47. Troxel, S.E., et al. "Anisoplanatism effects on signal-to-noise ratio performance of adaptive optical systems," *J. Opt. Soc. Am. A* (94). Submitted for Publication Feb 94.

48. Troxel, S.E., et al. "Off-axis optical transfer function calculations in an adaptive-optics system by means of a diffraction calculation for weak index fluctuations," *J. Opt. Soc. Am. A* (94). To be Published Jul 94.

49. Tyler, G.A. "Turbulence-induced adaptive-optics performance degradation: evaluation in the time domain," *J. Opt. Soc. Am. A*, 3(1):251-262 (March 1984).

50. Vernin, J. and F. Roddier. "Experimental determination of two-dimensional spatiotemporal power spectra of stellar light scintillation. Evidence for a multilayer structure of the air turbulence in the upper troposphere," *J. Opt. Soc. Am., 63*(3):270–273 (March 1973).

51. VonNiederhausern, R. N. *Performance Analysis of the Speckle Holography Image Reconstruction Technique.* MS thesis, AFIT/GE/ENG/91D-05, School of Engineering, Air Force Institute of Technology, Wright–Patterson AFB, Oh 45433, December 1991.

52. Wallner, Edward P. "Optimal wave-front correction using slope measurements," *J. Opt. Soc. Am., 73*:1771–1776 (December 1983).

53. Welsh, B. M. and R. N. Von Niederhausern. "Performance analysis of the self-referenced speckle holography image reconstruction technique," *Appl. Opt., 32*:5071–5078 (1993).

54. Welsh, Byron M. "Imaging performance analysis of adaptive optical telescopes using laser guide stars," *Appl. Opt., 30*(34):5021–5030 (1 December 1991).

55. Welsh, Byron M. and Chester S. Gardner. "Performance analysis of adaptive-optics systems using laser guide stars and slope sensors," *J. Opt. Soc. Am. A, 6*(12):1913–1923 (December 1989).

56. Welsh, Byron M. and Chester S. Gardner. "Effects of turbulence-induced anisoplanatism on the imaging performance of adaptive-astronomical telescopes using laser guide stars," *J. Opt. Soc. Am. A, 8*(1):69–80 (1991).

57. Zollars, Byron G. "Atmospheric-turbulence compensation experiments using synthetic beacons," *Lincoln Laboratory Journal, 5*(1):67–92 (1992).

Vita

Capt Steve Troxel entered the United States Air Force in 1980 and served as an enlisted Titan missile crew member at Davis Monthon AFB Arizona. He was selected for the Airman Education and Commissioning Program and received a Bachelor of Science degree in Electrical Engineering from the University of Arizona, Tucson, Arizona, Dec 1983. Upon graduation, he was commissioned as a lieutenant and served as a technical engineer with the Minuteman and Peacekeeper missiles at F.E. Warren AFB Wyoming. He subsequently received a Master of Science degree in Electrical Engineering from the Air Force Institute of Technology, Wright-Patterson Air Force Base, Ohio, December 1987. In March 1988 he was promoted to the rank of Captain while serving as the Chief of Laser Data Processing, Foreign Technology Division, Wright-Patterson AFB, Ohio. In June of 1991 Capt Troxel started working a doctorate degree in Electrical Engineering at the Air Force Institute of Technology, Wright-Patterson Air Force Base, Ohio. His next assignment is with the Optical Radiation Division of Armstrong Labs at Brooks AFB, Texas.

Permanent address: 1435 Edenwood Dr.
Beavercreek, OH

REPORT DOCUMENTATION PAGE

1. AGENCY USE ONLY (Leave blank)	2. REPORT DATE **June 1994**	3. REPORT TYPE AND DATES COVERED *Doctoral Dissertation*

4. TITLE AND SUBTITLE	5. FUNDING NUMBERS
A diffraction-based model of **anisoplanatism effects in adaptive optic systems**	

6. AUTHOR(S)

Steven E. Troxel, Capt, USAF

7. PERFORMING ORGANIZATION NAME(S) AND ADDRESS(ES)	8. PERFORMING ORGANIZATION REPORT NUMBER
Air Force Institute of Technology, WPAFB OH 45433-6583	**AFIT/DS/ENG/94J-05**

9. SPONSORING / MONITORING AGENCY NAME(S) AND ADDRESS(ES)	10. SPONSORING / MONITORING AGENCY REPORT NUMBER
PL/LIG (Brent Ellerbroek) **3550 Aberdeen Av. S.E.** **Kirtland AFB, NM 87117-5776**	

11. SUPPLEMENTARY NOTES

12a. DISTRIBUTION / AVAILABILITY STATEMENT	12b. DISTRIBUTION CODE
Approved for Public Release; Distribution Unlimited.	

13. ABSTRACT (Maximum 200 words)

This dissertation presents a new model for computing the angle dependent performance measures of an adaptive-optics system. By incorporating diffraction caused by the index-of-refraction variations of the atmosphere, the phase and amplitude fluctuations of the propagating wave are computed. New theory is presented, that uses the diffraction-based propagation model to yield optical transfer function (OTF) expressions that are more accurate as compared to current theory that neglects diffraction. An evaluation method for calculating the OTF is presented that utilizes a layered atmospheric model and normalized OTF expressions. The diffraction model is also used to present the first OTF signal-to-noise ratio (SNR) expressions that are a function of separation angle between the beacon and the object in an adaptive-optics system. An evaluation method for the SNR is presented that utilizes normalized correlation functions which are valid over a wide range of atmospheric conditions and correction geometries. An analysis of the angle dependency of the point spread function (PSF) is presented using the derived OTF expression. The diffraction model is then used to develop a new adaptive-optics wavefront correction algorithm that results in an extended correctable field-of-view (FOV) as compared to current correction algorithms.

14. SUBJECT TERMS	15. NUMBER OF PAGES
Adaptive Optics, Atmospheric Optics, Anisoplanatism, Atmospheric Turbulence	**124**
	16. PRICE CODE

17. SECURITY CLASSIFICATION OF REPORT	18. SECURITY CLASSIFICATION OF THIS PAGE	19. SECURITY CLASSIFICATION OF ABSTRACT	20. LIMITATION OF ABSTRACT
Unclassified	**Unclassified**	**Unclassified**	**UL**

GENERAL INSTRUCTIONS FOR COMPLETING SF 298

The Report Documentation Page (RDP) is used in announcing and cataloging reports. It is important that this information be consistent with the rest of the report, particularly the cover and title page. Instructions for filling in each block of the form follow. It is important to **stay within the lines to meet optical scanning requirements.**

Block 1. Agency Use Only (Leave Blank)

Block 2. Report Date. Full publication date including day, month, and year, if available (e.g. 1 Jan 88). Must cite at least the year.

Block 3. Type of Report and Dates Covered. State whether report is interim, final, etc. If applicable, enter inclusive report dates (e.g. 10 Jun 87 - 30 Jun 88).

Block 4. Title and Subtitle. A title is taken from the part of the report that provides the most meaningful and complete information. When a report is prepared in more than one volume, repeat the primary title, add volume number, and include subtitle for the specific volume. On classified documents enter the title classification in parentheses.

Block 5. Funding Numbers. To include contract and grant numbers; may include program element number(s), project number(s), task number(s), and work unit number(s). Use the following labels:

C	- Contract	PR	- Project
G	- Grant	TA	- Task
PE	- Program Element	WU	- Work Unit Accession No.

Block 6. Author(s). Name(s) of person(s) responsible for writing the report, performing the research, or credited with the content of the report. If editor or compiler, this should follow the name(s).

Block 7. Performing Organization Name(s) and Address(es). Self-explanatory.

Block 8. Performing Organization Report Number. Enter the unique alphanumeric report number(s) assigned by the organization performing the report.

Block 9. Sponsoring/Monitoring Agency Names(s) and Address(es). Self-explanatory.

Block 10. Sponsoring/Monitoring Agency. Report Number. (If known)

Block 11. Supplementary Notes. Enter information not included elsewhere such as: Prepared in cooperation with...; Trans. of ..., To be published in .... When a report is revised, include a statement whether the new report supersedes or supplements the older report.

Block 12a. Distribution/Availablity Statement. Denote public availability or limitation. Cite any availability to the public. Enter additional limitations or special markings in all capitals (e.g. NOFORN, REL, ITAR)

DOD	-	See DoDD 5230.24, "Distribution Statements on Technical Documents."
DOE	-	See authorities
NASA	-	See Handbook NHB 2200.2.
NTIS	-	Leave blank.

Block 12b. Distribution Code.

DOD	-	DOD - Leave blank
DOE	-	DOE - Enter DOE distribution categories from the Standard Distribution for Unclassified Scientific and Technical Reports
NASA	-	NASA - Leave blank
NTIS	-	NTIS - Leave blank.

Block 13. Abstract. Include a brief (Maximum 200 words) factual summary of the most significant information contained in the report.

Block 14. Subject Terms. Keywords or phrases identifying major subjects in the report.

Block 15. Number of Pages. Enter the total number of pages.

Block 16. Price Code. Enter appropriate price code (NTIS only).

Blocks 17. - 19. Security Classifications. Self-explanatory. Enter U.S. Security Classification in accordance with U.S. Security Regulations (i.e., UNCLASSIFIED). If form contains classified information, stamp classification on the top and bottom of the page.

Block 20. Limitation of Abstract. This block must be completed to assign a limitation to the abstract. Enter either UL (unlimited) or SAR (same as report). An entry in this block is necessary if the abstract is to be limited. If blank, the abstract is assumed to be unlimited.